NOTE TO USERS

Page(s) not included in the original manuscript and are unavailable from the author or university. The manuscript was scanned as received.

61,81, & 82

UNIVERSITY OF OKLAHOMA

GRADUATE COLLEGE

INTRASEASONAL VARIABILITY

OF THE

NORTH AMERICAN MONSOON OVER ARIZONA

A Dissertation

SUBMITTED TO THE GRADUATE FACULTY

in partial fulfillment of the requirements for the

degree of

Doctor of Philosophy

By

Pamela Lynn Heinselman
Norman, Oklahoma
2004

UMI Number: 3117196

INFORMATION TO USERS

The quality of this reproduction is dependent upon the quality of the copy submitted. Broken or indistinct print, colored or poor quality illustrations and photographs, print bleed-through, substandard margins, and improper alignment can adversely affect reproduction.

In the unlikely event that the author did not send a complete manuscript and there are missing pages, these will be noted. Also, if unauthorized copyright material had to be removed, a note will indicate the deletion.
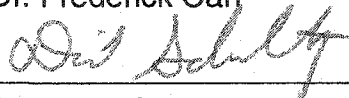
INTRASEASONAL VARIABILITY
IN THE
NORTH AMERICAN MONSOON OVER ARIZONA

A Dissertation APPROVED FOR THE
SCHOOL OF METEOROLOGY
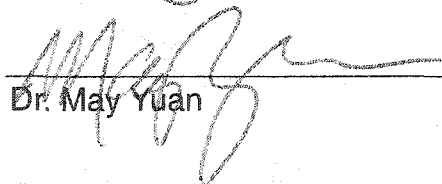
BY

_____

Dr. Frederick Carr

_____

Dr. David Schultz

_____

Dr. Michael Richman

_____

Dr. Alan Shapiro

_____

Dr. David Stensrud

_____

Dr. May Yuan

Acknowledgments

This dissertation arose from personal perseverance and support and encouragement from my Ph.D. committee, colleagues, friends, and family. Concerning Ph.D. committee members, I thank them all for their affable attitude through this process, especially when changes in schedule arose. Early on, Dr. Alan Shapiro helped build confidence in my ability to independently learn and apply dynamics theory, via my paper on EP Flux. Throughout this process, Dr. Stensrud provided insightful discussion, questions, and comments about my research, as well as his personal support. Dr. Richman was helpful concerning statistical evaluation of sounding parameters and Dr. Yuan helped me fine tune fundamental results. Dr. Carr challenged me to know the details of tools used in the research. Most importantly, Dr. Schultz helped me grow as a researcher, writer, and presenter. His ability to ask probing questions and remain dedicated to excellence is greatly appreciated.

I also thank several colleagues at the National Severe Storms Laboratory and the Storm Prediction Center for sharing their expertise. Dr. Jian Zhang provided her radar mosaic code and helped me adapt it as needed; these actions made this research possible. John Hart supplied his NSHARP code, which aided my examination of sounding variables. Dr. Harold Brooks was willing to discuss statistical results at the drop of a hat, and Dr. Kim Elmore furnished unparalleled personal and technical support. Dr. Kimpel worked with NOAA to provide mone-

tary support, which made this degree more easily attainable. In addition, Dr. Zrnic gave me the freedom to finish this paper during work hours, a gift I will work hard to repay in the coming years. Last, but not least, Ken Howard invited me to work on this topic for my Ph.D. and provided significant funding through the Salt River Project (SRP). Thus, I also extend thanks to SRP for making this research possible.

My family and friends are responsible for keeping me sane while attaining my Ph.D. I especially thank Jeanne and Gary Tesch for their listening ears, advice, and fun times together. Listening ears and fun times were also provided by Daphne Zaras and Carrie Langston–thank you! I also thank all the ladies at Memorial Presbyterian Church who supported this venture, including Doris Hinson, Dr. Alice Lanning, Lucy Lanning, Holly Van Auken, and Ruby Marsh. Thanks extend across the miles to Gail Tardio, in Tucson, AZ, for her love and support, through great cards and e-mail. Of course, I also appreciate all the love, support, and caring given by my mom and dad, Dianne and Don Heinselman, and my brother Kevin. My greatest proponent of my success was, and still is, my fiance and best friend, Carl Wood. His loving words and vivid analogies guided me through the completion of this research and the writing of this paper.

v

Table of Contents

List of Tables

LIST OF ILLUSTRATIONS

; mm), calculated from 12 UTC soundings at Phoenix. Filled
boxes show the data distribution within the 25th and 75th
percentiles, where the median is denoted by a thick white line.
Outermost braces indicate values within 1.5 x interquartile
range (IQR, defined as the difference between the 75th and
5th percentiles), whereas isolated horizontal lines indicate
outliers.

Abstract

In Arizona, the North American Monsoon (NAM) supplies up to 50% of the region's annual rainfall. Although Arizona's diurnal precipitation climatology indicates that precipitation follows a regular cycle, daily storm development patterns deviate from this periodicity. The purpose of this study is to investigate the intraseasonal variability of diurnal storm development and environment over Arizona. Intraseasonal variability of diurnal storm development is investigated during the 1997 and 1999 NAMs using radar reflectivity moasics constructed from Phoenix and Flagstaff Weather Surveillance Radar-1988 Doppler (WSR-88D) data. This investigation reveals five repeated storm development patterns or regimes, including the 1) dry regime (DR), 2) eastern mountain regime (EMR), 3) central–eastern-mountain regime (CEMR), 4) central–eastern-mountain and Sonoran regime (CEMSR), and 5) nondiurnal regime (NDR), listed in the order of increasing areal storm coverage across the domain. Although regions within these regimes overlap, they highlight different regions where storm development is most active, which, in turn, may prove useful for zone forecasts within the NWS. The environment associated with each regime is found by analyzing 12 UTC soundings at Phoenix and 500-mb maps over the southwest United States. This analysis shows that the spatial distribution of tropospheric moisture controls the areal extent of storm development over elevated terrain. In turn, the spatial distribution of tropospheric moisture is controlled by the synoptic-scale flow.

A discriminant analysis of several 12 UTC sounding variables at Phoenix reveals that precipitable water provides strong discrimination of DR and EMR from each other, and, the more convectively active regimes (e.g., CEMR, CEMSR, and NDR). On the other hand, 0–6-km shear offers the best discrimation of NDR from CEMR and CEMSR. Although this discriminant analysis becomes less skillful when considering the potential for one or more of the wet regimes (especially CEMR vs. CEMSR), as a whole, the combined discriminant analysis (Fig. 23) has more skill than a random forecast (HSS=0.43), and is more accurate than persistence or a one in five guess.

Another aspect of intraseasonal variability is the daily persistence of regimes. DR is the most persistent regime, followed by CEMR, NDR, EMR, and CEMSR. Occasionally, sharp changes in storm coverage precede or follow a given regime. At mid–upper-levels significant local changes in moisture arise mostly from quasi-horizontal advection, in response to changes in the synoptic-scale flow. In most cases, moistening corresponds with the westward or northward expansion of the subtropical high, whereas drying corresponds with the passage of a shortwave trough. Occasionally, mid–upper-level moistening is enhanced by the vertical advection of moisture ahead of shortwave troughs. At low-levels in Phoenix, significant changes in moisture at 12 UTC are associated with three situations: precipitation in the vicinity of Phoenix the previous night (30%), surges from the Gulf of California (35%), and moisture advection east or southeast of Phoenix (35%).

1. Introduction

Over 63% of Arizona's 5.13 million residents live in Phoenix–Mesa, a metropolitan area with an explosive population growth of 45.3% between 1990 and 2000 (http://www.census.gov). With this rapidly growing population, the potential impacts from summertime convective storms are increasing. Socio-economic impacts from storms can include damage to property and threat to life from high winds, flash flooding, and/or copious lightning (Hales 1975; Schmidli 1986), downed power lines resulting in loss of profits to power companies and disruption to life and businesses, and transportation delays.

Arizona receives 40–60% of its annual rainfall from summer storms. Farmers and cattle ranchers depend on summer runoff to keep their vegetation thriving (Jurwitz 1953; Sellers and Hill 1974; C. Ester 2001, personal communication). This summer wet season occurs in response to the North American Monsoon (NAM), a reversal in circulation at low and midlevels over Mexico and the Desert Southwest every July and August (Fig. 2; Douglas et al. 1993). A map of the region is shown in Fig. 1a. During this wet season, precipitation exhibits a diurnal cycle. Arizona's summertime diurnal precipitation climatology is forced primarily by mountainous terrain surrounding the Sonoran Desert (Fig. 1b). In the morning, storms tend to initiate over the Mogollon Rim, White Mountains, and Southeast Highlands. Storms move and redevelop southward down the Mogollon Rim, and
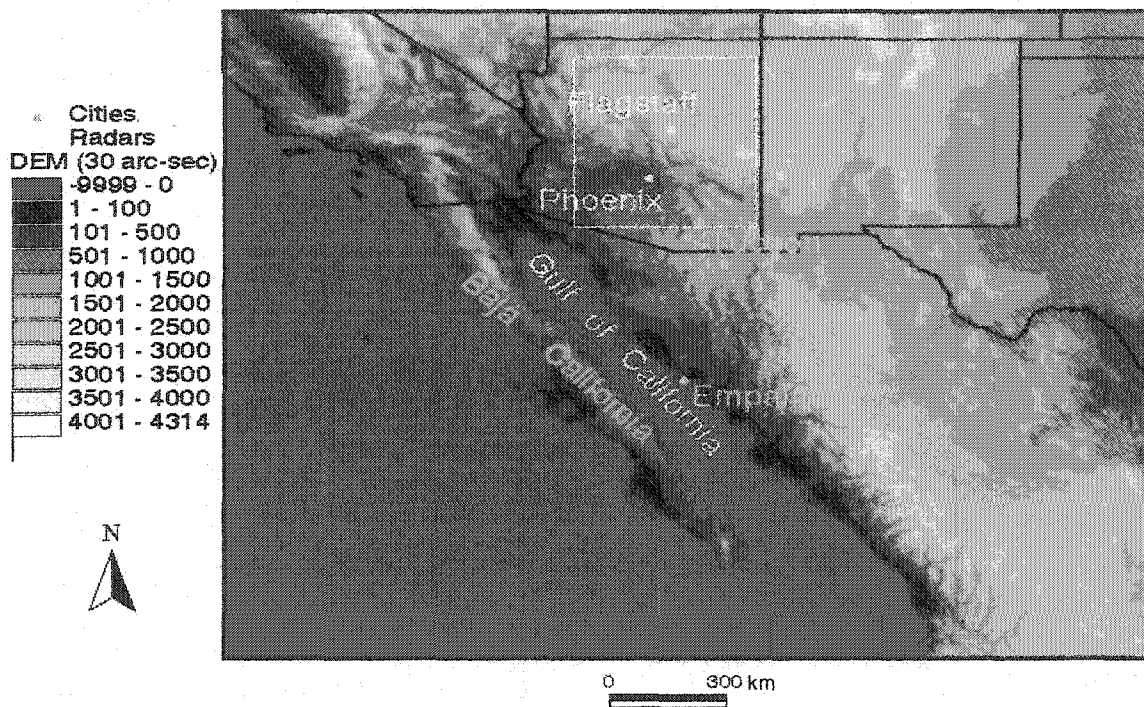
Figure 1a. Terrain map of the southwest United States and Mexico, including radar sites and cities mentioned in text. The white box indicates the domain investigated in this study. Elevation data are gridded at 1-km resolution from 30 arc-sec USGS data.
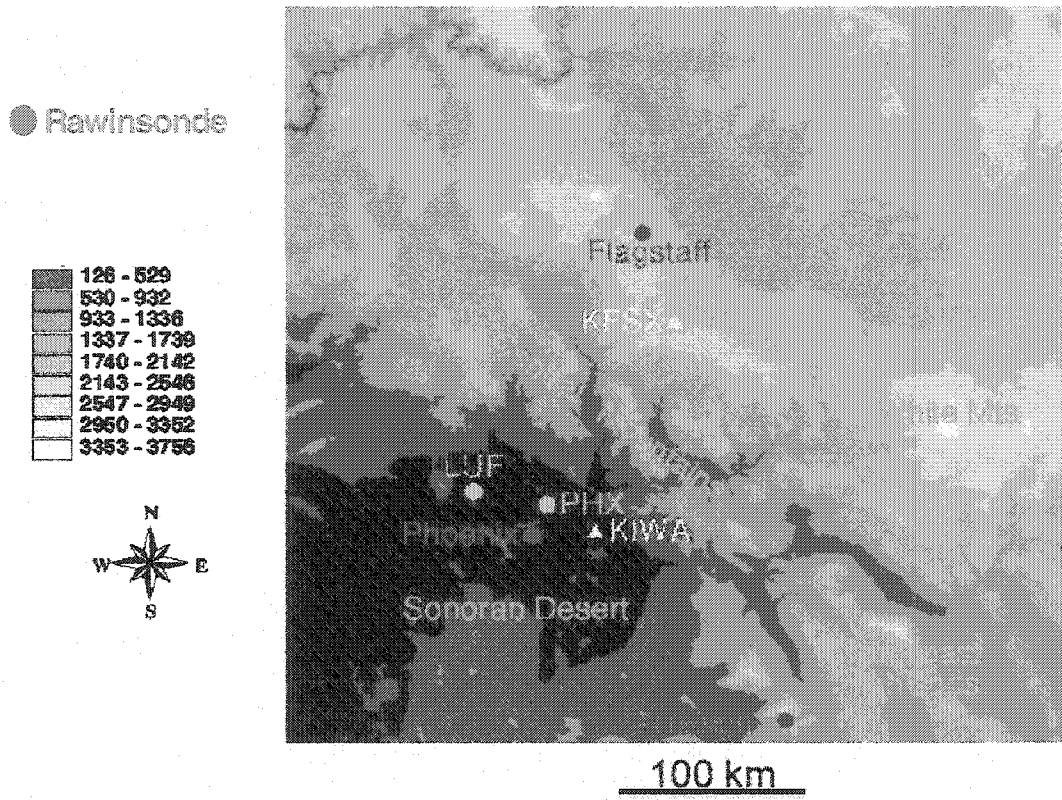
Figure 1b. Elevation (m) of terrain features in domain, gridded at 1-km resolution from 30 arc-sec USGS data. Also shown are locations of WSR-88D sites (yellow triangles), rawin-sonde sites (orange circles), and cities (pink circles).

move southwestward from the White Mountains and Southeast Highlands during the afternoon, culminating in the Sonoran Desert near sundown. This evolution is ubiquitous: it appears in diurnal climatologies using precipitation-gauge (Balling and Brazel 1987), lightning (Watson et al. 1994b; King and Balling 1994) and radar reflectivity data (Hales 1972b; MacKeen and Zhang 2000). Despite this robust diurnal precipitation cycle, tremendous intraseasonal variations in the occurrence, timing, and location of convective storms are possible.

Intraseasonal variations in Arizona's precipitation during the NAM are categorized as wet and dry periods, or "bursts" and "breaks," respectively. Previous studies have identified differences between composited synoptic-scale patterns during these periods to help forecasters discern environments supporting or inhibiting precipitation (Carleton 1986; Watson et al. 1994a; Mullen et al. 1998). Such simple stratifications of synoptic-scale flows, however, find upper-air patterns with limited relevance to forecasts on individual days.

The purpose of this research is to investigate the variability in daily storm development patterns and atmospheric environment during the NAM over mountainous and desert terrain in Arizona (Fig. 1b). This investigation is pursued by addressing the following questions: 1) What is the role of synoptic-scale flow on controlling the occurrence and location of storm development? 2) Do a variety of diurnal storm development patterns occur over Arizona, and if so, how persistent are they? and 3) Given such a variety, are some patterns easier to forecast than

4

others? It is anticipated that answers to such questions will lead to improved regional forecasts of storm likelihood that may, in turn, help residents and businesses prepare better for possible threats to life, damage to property, and loss of profit.

In Chapter 2, mechanisms associated with the development of Arizona's summer wet season are reviewed. Chapter 3 describes the radar data and methodology used to identify the five repeated storm development patterns found in this study, Chapter 4 examines characteristics of Phoenix soundings that may be used to help discern the potential for a given storm development pattern, Chapter 5 examines the relative importance of synoptic-scale forcing associated with the patterns, and Chapter 6 presents a conceptual model of storm development variability and the role of synoptic-scale flow in Arizona during the NAM. Chapter 7 presents conclusions and discusses the relevance of this research to operational forecasting.

Chapter 2: Physical Processes in the North American Monsoon

Circulations comprising the NAM are described in Section 2.1. Section 2.2 reviews the mean synoptic environments associated with bursts and breaks, and Section 2.3 discusses possible mechanisms for storm development.

2.1 The NAM

The NAM is defined by reversals in tropospheric wind direction that occur in response to interactions between the underlying topography and incoming solar radiation (Tang and Reiter 1984). Owing to the annual early summer peak in solar insolution over the subtropics, the thermal gradient over the North American Hemisphere shifts northward. Differential heating of the land and sea results in the development of a thermal low over the deserts of Arizona, southeastern California, and northwestern Mexico, which results in a low-level (500 m AGL–850 mb) change in wind direction over Arizona from westerly to southerly (Tang and Reiter 1984; Rowson and Colucci 1992; Douglas et al. 1993; Adams and Comrie 1997; Tucker 1999). The intensity of the thermal low is regulated, at least in part, by the evolution of synoptic-scale systems (Rowson and Collucci 1992) and the diurnal cycle (Douglas and Li 1996). During the summer, strong tropospheric heating results in deep tropospheric layers of constant pressure, and, hence, the development of a mid–upper-level (700–100 mb) high pressure system over the southwest U.S. (Fig. 2; Reed 1933,1939; Bryson and Lowry 1955; Douglas et al. 1993; Adams and Comrie 1997).

Interestingly, the NAM is only one of several monsoon systems. Like the NAM, the Asian, Australian, west African, and South American monsoons (SAM) have an annual cycle that has two distinct phases: wet-warm, and dry-cool (Magana and Webster 1998). Both the NAM and SAM, and Asian and Australian monsoons coexist, owing to the reversal in tropospheric flow between summer and winter seasons (Magana and Webster 1998). Although both the NAM and Asian monsoon are driven by similar mechanisms and occur during the summer months, several of their characteristics differ. First, the scale of the Asian monsoon is larger than that of the NAM (Magana and Webster 1998). This difference in scale appears related to the much larger Asian land mass, higher mountainous regions, and the larger coastal plain, compared to Mexico. In addition, the Asian monsoon is associated with three large, interacting circulations, including the Walker Circulation, the Transverse monsoon circulation, and the lateral monsoon circulation (Magana and Webster 1998), whereas the NAM is associated primarily with two interacting circulations, including the subtropical and North Pacific Highs. Composite troughs within these monsoons also show that confluent flow is north–south-oriented during the Asian monsoon, and east–west-oriented during the NAM. Given such differences in scale between the Asian and NAMs, do differences in precipitation characteristics occur as well?

Both the NAM and Asian monsoon consist of wet and dry periods. During the NAM, wet or dry periods generally last for 2–5 days, whereas during the Asian monsoon, these wet or dry periods generally last longer: 10–40 days (Magana

7

and Webster 1998). In addition, moisture anomalies associated with wet and dry periods of the Asian monsoon span larger spatial scales (east African coast to the date line!) than those associated with the NAM (Mexico and southwest US; Magana and Wester 1998; Schmitz and Mullen 1996). Furthermore, the longer wet periods associated with the Asian monsoon result in higher values of latent heat release, compared to the NAM (Magana and Webster 1998). These higher values of latent heat release, coupled with the more elevated heat source of the Himalaya mountains, apparently results in stronger easterlies than those found just south of Arizona, in the form of an easterly jet stream (Magana and Webster 1998). The intensity of this easterly jet indicates the intensity of the Asian monsoon (1998). As described later, the intensity of the NAM may be closely related to the passage of waves in the easterlies, which induce a strong northward-moving jet over the Gulf of California.

The correspondence of the NAM to summer precipitation occurrence over western Mexico, Arizona, and New Mexico was recognized in the early 1920s, when scientists find that the development of this precipitation is related to both the development of the thermal low (Campbell 1906; Beals 1922; Blake 1923) and the transport of moisture from the Gulf of California into the southwest U.S. (Blake 1923). More concrete evidence for this transport of moisture arises when Rasmussen (1967) finds a positive net annual flux of water vapor from the northern Gulf of California into Arizona. Soon afterward, Hales (1972a, 1974) and Brenner (1974) show that the transport of moisture from the Gulf of California into the
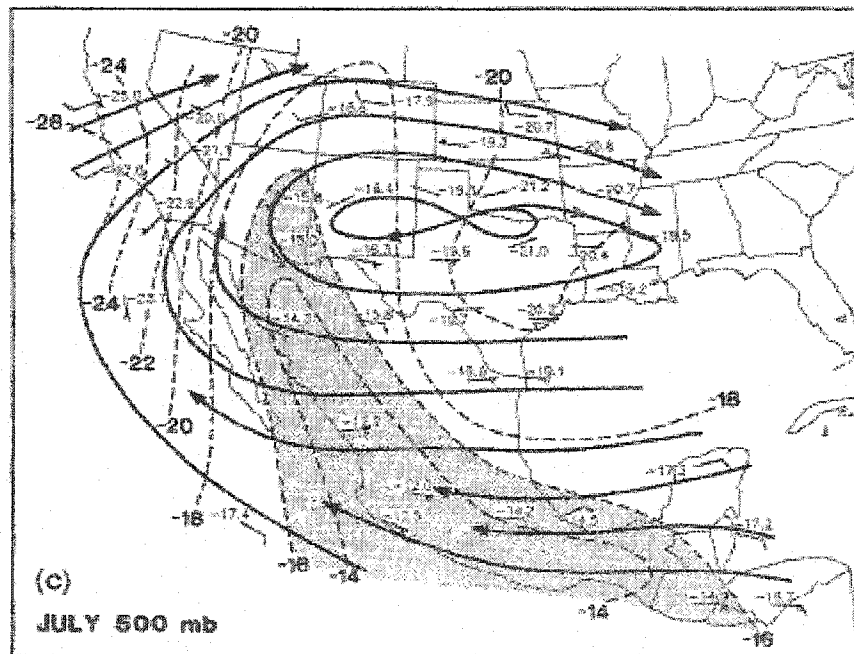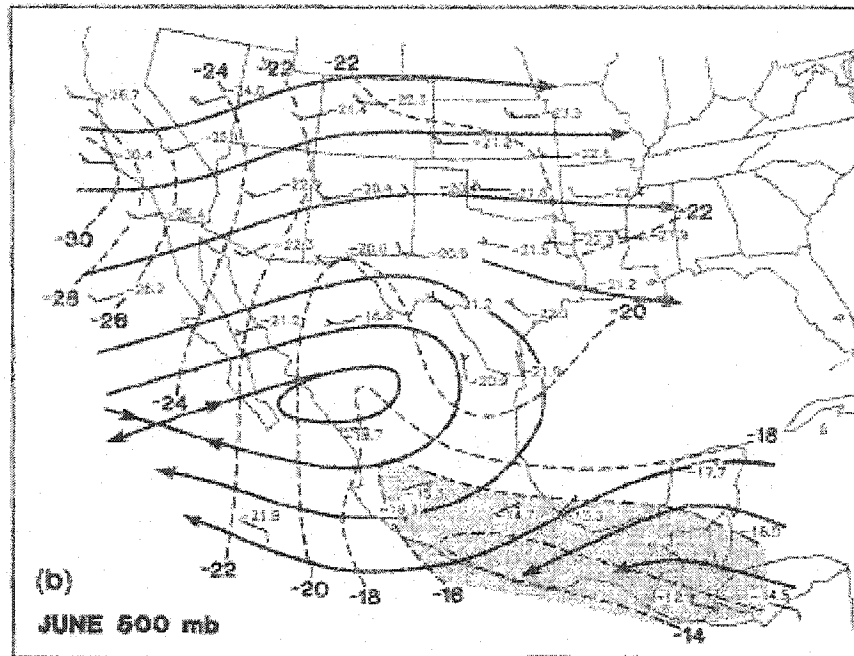
Figure 2. Mean winds (m s^{-1}), streamlines, and dewpoint temperature (°C) analysis for June and July. Means use 12 UTC data for the 11-year interval 1979–1989. Areas with dewpoint temperatures > -16 °C area shaded: a) June, and b) July. Taken from Douglas et al. 1993.

southwest U.S. sometimes occurs as "surges" of low-level moisture. Surges

approaching southern Arizona are characterized by relatively strong low-level

southerly winds (10–15 m s^{-1}), cool temperatures, high pressure, high dewpoints,

and low–mid-level cloudiness (Hales 1972a, 1974; Brenner 1974; Stensrud et al.

1997).

Hales (1972a) speculates that during surges, such low-level moisture is

channelled northward—between the Sierra San Pedro Martir of Baja, California,

and the Sierra Madre Occidental of Mexico—from the Gulf of California into south-

ern Arizona via an enhancement of the meridional pressure gradients that nor-

mally exist between the relatively cool air over the southern Gulf of California, and

the relatively hot desert air over the southwest U.S. thermal low (Figs. 6, 7 of

Hales 1974). After further investigation, Hales (1974) later finds that five-day run-

ning means of 850-mb temperature ($^{\circ}$C) at Empalme and 850-mb relative humid-

ity at Tucson show a linear correlation at zero, 24- and 48- hour time lags, of -

0.71, -0.76, and -0.69, respectively. Hales (1974) credits the relatively cool air at

Empalme, and the associated increase in relative humidity at Tucson, to influxes

of moist, cool tropical air following the passage of tropical disturbances over

the southern part of the Gulf of California (Fig. 3). A more recent 9-yr climatology

of surges at Empalme, Mexico, provides a more detailed spatial and temporal

analysis of surge characteristics (Douglas and Leal 1989). The idea that the pas-

sage of tropical disturbances, or easterly waves over the Gulf of California are

related to the development of surges over the Gulf of California, is corroborated

10

by several authors (Brenner 1974; Stensrud et al. 1997; Douglas and Leal 1989; Anderson et al. 2000; Fuller and Stensrud 2000). For example, Fuller and Stensrud (2000) show that within three days following the passage of a tropical easterly wave westward of 110° W, 70% of easterly wave passages over a 14-y period are associated with a moisture surge at Yuma, Arizona. Interestingly, a numerical modeling study of surges by Stensrud et al. (1997), indicates that strong gulf surges, or those that affect Arizona, tend to occur a few days following the passage of a midlatitude trough over the western United States. Thus, both tropical and midlatitude systems may be important to the occurrence of gulf surges.

Since surges occur only occasionally during the NAM, a more continuous process is likely responsible for the positive water vapor flux that several authors find from the northern Gulf of California into Arizona (Rasmussen 1967; Houghton 1979; Tang and Reiter 1984; Badan-Dagon et al. 1991; Douglas et al. 1993; Schmitz and Mullen 1996; Higgins 1997). Douglas (1995) uses data collected during the 1990 Southwest Area Monsoon Project (SWAMP) to show that a daily nocturnal low-level jet (LLJ) develops below 700 mb over the northern part of the Gulf of California. Special pilot balloon reports and aircraft data indicate that this LLJ is characterized by a 12 UTC speed maxima ($\sim$7 ms^{-1}) at a height of 500 m AGL over Yuma, and at a height of 250–400 m AGL over the Gulf of California. Douglas (1995) surmises that this low-level southerly flow is forced by a pressure gradient force that develops in response to a mean temperature difference (6°C at 900 mb) between the stations. This mean temperature difference is about half that
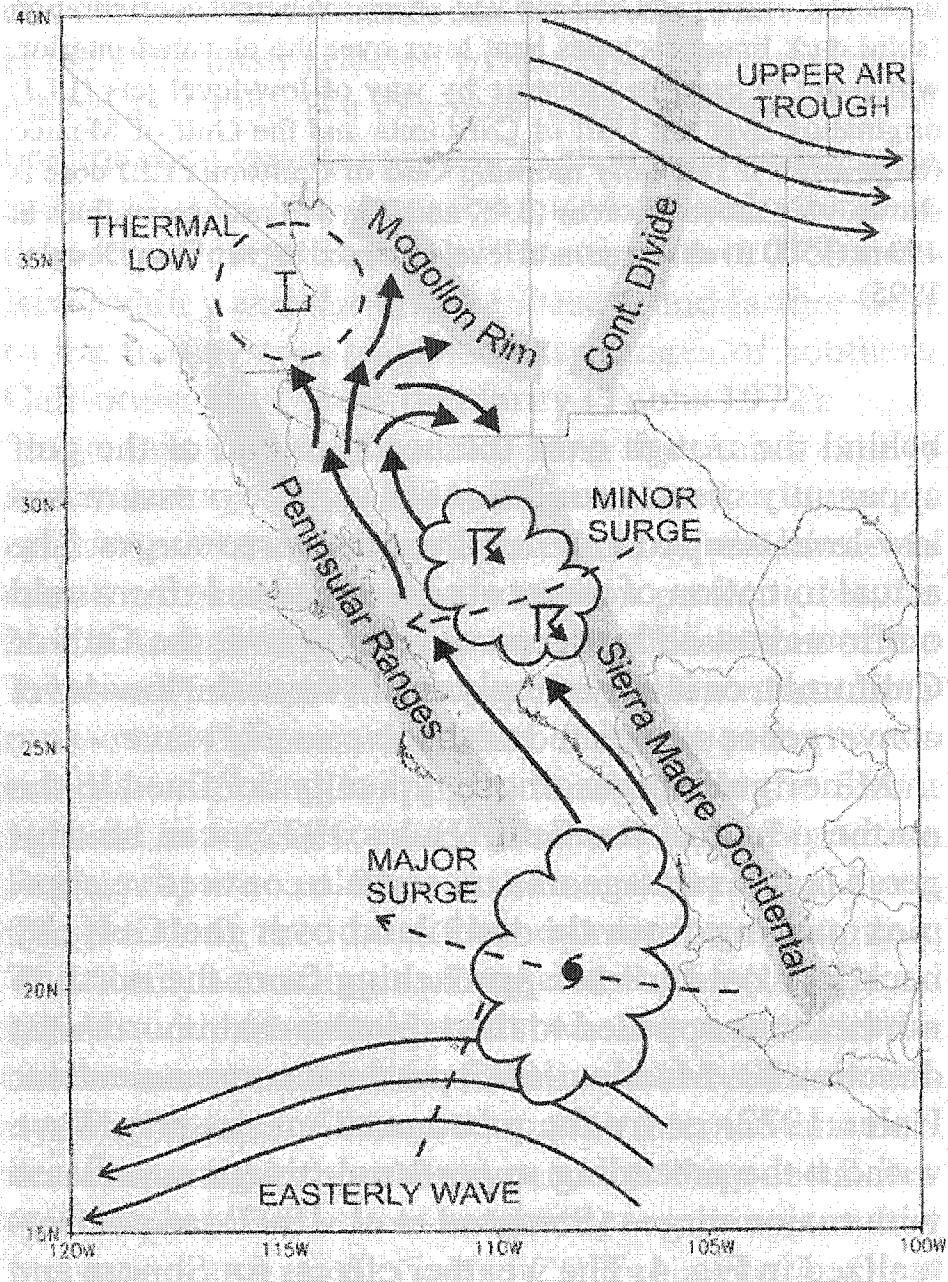
Figure 3. Conceptual model of gulf surges from the Gulf of California, where surges are associated with either the passage of an easterly wave, south of the Gulf of Calfornia, or mesoscale convective systems drifting over the northern half of the gulf. Taken from Adams and Comrie 1997.

calculated by Hales ($10°C$,1974) for a surge event in August 1972. Consequently, the pressure gradient force apparently forces both the LLJ and surges, and surges are an intensification of this channelled flow.

In the late 1920's, the collection of upper-air observations shift the attention of researchers from the thermal low to the newly observed mid–upper-level anti-cyclone as a circulation important to the development of the NAM. Reed (1933, 1939) finds that the position of a 500-mb closed anticyclone, which develops in tandem with the thermal low, may be associated with precipitation occurrence over Arizona. He suggests that precipitation is more likely to develop over Arizona when the center of this high is located eastward rather than westward of the state because air transported into the region is likely more moist, and therefore, more conducive to storm development. Later, climatologies of the southwest U.S. summer 700- and 500-mb flow show that, in the mean, southerly-to-southwesterly winds from the Bermuda high anticyclone transport air into Arizona (e.g., Fig. 2; Bryson and Lowry 1955; Douglas 1993). Based on this flow pattern, Bryson and Lowry (1955) surmise that moist air is transported into Arizona from the Gulf of Mexico, and that the Gulf of Mexico is the primary moisture source during NAM; similar reasoning arose from Jurwitz (1953), although no analyses are shown in his paper.

The idea that the Gulf of Mexico is Arizona's primary source of moisture during the summer is later discounted by several authors who reason that air

transported northwestward from the Gulf of Mexico into Mexico by the Bermuda High is dried substantially after passing over the Sierra Madre Oriental and the Sierra Occidental prior to reaching Arizona (Hales 1972a, 1974; Brenner 1974; Douglas et al. 1993). Schmitz and Mullen (1996) address this issue quantitatively by analyzing European Center for Medium-range Forecasts (ECMWF) water vapor fields over Mexico and the United States. Differences in moisture transport between lower and upper levels are discerned by calculating vertically integrated moisture flux vectors for the surface-to-700-mb layer and the 700-to-200-mb layer (Fig 7. of Schmitz and Mullen 1996). The low-level flux is northward from the Gulf of California into Arizona, whereas the mid-level flux is northwestward from western Mexico into Arizona. A trajectory analysis shows that the moist air over western Mexico originates from the Gulf of Mexico. Based on these results, Schmitz and Mullen (1996) conclude that low-level moisture arises from the Gulf of California, and that mid–upper level moisture arises from the Gulf of Mexico. Owing to the ECMWF's relatively large grid spacing (1.125° lat x 1.125° lon), mesoscale processes are poorly represented. Therefore, it is possible that midlevel moist air over Arizona may originate, at least in part, from vertical mixing of moist air from mesoscale convective systems (MCSs) that form over mountainous terrain in western Mexico (e.g., Brenner 1974; Douglas et al. 1993). This air may then be advected over Arizona by the southeasterly-to-southerly flow of the mid-level anticyclonic flow.

In summary, the circulations comprising the NAM include a heat low over Arizona and the northward-shifted Subtropical High. The establishment of these circulations allows the transport of moisture at low-levels by the daily low-level jet over the Northern Gulf of California and occasional surges, and the transport of moisture at mid–upper levels, in part, by the Subtropical High. While this relative enhancement of moisture over Arizona creates a large-scale environment supportive of storm development, periods of wet and dry weather occur during the NAM, coinciding with variations in the mean synoptic environment (Carleton 1986; Watson et al. 1994a; Mullen et al. 1998). Mean synoptic environments associated with bursts and breaks are summarized below.

2.2 Mean synoptic environments associated with bursts and breaks

During the NAM, Arizona experiences periods of wet and dry weather, called 'bursts' and 'breaks,' respectively. Such bursts and breaks have been analyzed using three different data sets: 1980–1982 GOES-W infrared satellite data over the southwest U.S. (Carleton 1986), 1985–1990 Bureau of Land Management lightning data over Arizona (Watson et al. 1994a), and 1985–1992 precipitation data over southeastern Arizona (Mullen et al. 1998). A purpose of these studies is to identify the mean synoptic-scale environment responsible for periods of wet and dry weather. Although the mean flow at low-levels exhibits a heat low over Arizona during both bursts and breaks (Carleton 1986), differences appear in the mean mid-level flow. In breaks, 500-mb composites show an east-to-west-ori-

15

ented longwave ridge over the southwest U.S., whose ridge axis is located southward of central Arizona (Figs. 4b, 4d; Carleton 1986; Watson et al. 1994a; Mullen et al. 1998). The resulting westerly flow advects dry air into Arizona that suppresses storm development (Carleton 1986; Watson et al. 1994a; Mullen et al. 1998).

In bursts, two composites arise: an east-to-west oriented longwave ridge over the southwest U.S., whose horizontal ridge axis is located farther northward than during breaks (Fig. 4c; Watson et al. 1994a; Mullen et al. 1998), and a shortwave trough in the westerlies approaching the southwest U.S. from the southeast Pacific, with the western edge of the Bermuda High located over Texas (Fig. 4a; Carleton 1986). The latter burst composite suggests that synoptic-scale forcing ahead of shortwave troughs is common during 1980–1982 NAMs. The absence of a shortwave trough in Watson et al.'s (1994a) and Mullen et al.'s (1998) burst composites suggests that other mechanisms, such as terrain forcing and/or mesoscale forcing, also play an important role.

Differences in moist transport at low- and mid- to upper-levels during bursts and breaks is investigated by Mullen et al. (1998). They find that similar amounts of moisture are transported from the northern Gulf of California into southern Arizona during *both* bursts and breaks (Mullen et al. 1998). This result corroborates previous analyses showing a positive water vapor flux at low-levels from the northern Gulf of California into Arizona during the summer (Rasmussen

16
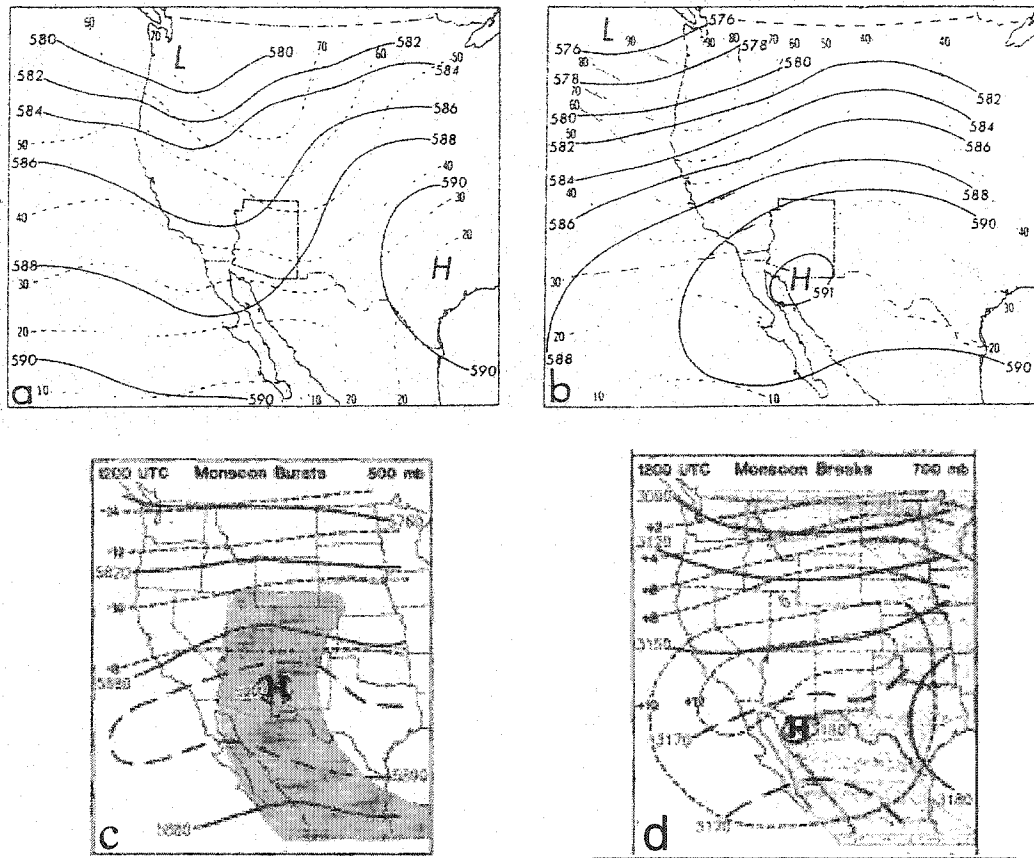
Figure 4. Carleton's (1986) composite 500-mb heights (in gpdm) for three monsoon seasons: 1980–1982, during a) bursts and b) breaks. Standard deviations (m) are dashed. Watson et al. (1994b) 500-mb analyses (m) for c) 12 monsoon bursts and d) 10 monsoon breaks. Temperature-dewpoint spreads of 5 °C or less are shaded and temperature isopleths are contoured.

1967;Houghton 1979; Tang and Reiter 1984; Badan-Dagon et al. 1991; Douglas 1995; Schmitz and Mullen 1996; Higgins 1997). In contrast, at mid–upper levels more moisture is transported into southeastern Arizona from the Gulf of Mexico during bursts than breaks (Mullen et al. 1998).

In summary, the occurrence of bursts and breaks in Arizona appears related to the mean mid–upper-level synoptic-scale flow and, in turn, the amount of moisture transported from the Gulf of Mexico into Arizona at mid–upper levels. Generally, less moisture is transported into Arizona during breaks because the mean mid–upper-level flow is westerly, whereas more moisture is transported into Arizona during bursts because the mean mid–upper-level flow is southerly. Since the amount of mean low-level moisture is similar during bursts and breaks, it appears that, on average, periods of precipitation are sensitive to the amount of available mean mid–upper-level moisture. In addition, during some NAMs, short-wave troughs apparently play an important role toward the development of bursts.

These findings address two of the three ingredients necessary for storm development during bursts: moisture and lift (Johns and Doswell 1992). While short wave troughs are an important source of lift during some NAM seasons, other lifting mechanisms, such as terrain forcing, also play a role. The next section reviews such lifting mechanisms, as well as processes affecting instability in Arizona.

2.3 Additional Mechanisms for storm development

One significant source of lift in Arizona is mountainous terrain (e.g., Banta 1990). Within this study's domain, areas of mountainous terrain are concentrated in the Southeast Highlands, the Central Mountains, and the Mogollon Rim, which surround the Sonoran Desert (Fig. 1b). During the afternoon, low-level flow over the Sonoran Desert is upslope, toward higher terrain (Douglas and Li 1996). In general, interactions between this flow and topographic features likely regulate daily storm development (e.g., Banta 1990; Fujita et al. 1962). For example, Fujita et al. (1962) discover that early-morning solar heating on the eastward facing slopes of the San Francisco Mountains (Fig. 1b) initiates a mesolow, which, in turn, creates localized convergence and lift for convective storm development. Additionally, they find higher rainfall totals occur when 600-mb winds contain a southerly rather than a northerly component, consistent with findings from burst and break studies.

The prominence of terrain forcing is evinced by Arizona's summer diurnal precipitation climatology, described previously in the Introduction (Balling and Brazel 1987; Watson et al. 1994b; King and Balling 1994; Hales 1972b; MacKeen and Zhang 2000). Since summer storms are usually short-lived, the apparent movement of precipitating convective cells from higher toward lower terrain raises an unanswered question: "What mechanisms are responsible for this evolution?". Two plausible mechanisms for such storm redevelopment include diurnal terrain

forcing and/or lift generated by downdrafts interacting with hot, moist upslope air (Watson et al. 1994b).

In practice, storm evolution from higher terrain into the Sonoran Desert does not occur daily, suggesting that at least one of the three ingredients needed for storm development is sometimes absent within the desert environment, including Phoenix–Mesa (Fig. 1b). The likelihood for storm development in the desert depends, in part, on the characteristics of the planetary boundary layer. During the afternoon in Phoenix–Mesa, the lapse rate in the planetary boundary layer is oftentimes dry adiabatic. In the presence of sufficient moisture and lift, this neutrally-stable environment must become conditionally unstable to support storm development. Hales (1977) hypothesizes that tropospheric destabilization in Phoenix may sometimes be instigated by the advection of mid-level cloud-cooled air, produced by afternoon thunderstorms over the mountains, over the hot desert landscape.

Stensrud (1993) finds two cases during the 1990 Southwest Area Monsoon Project (SWAMP) where elevated residual layers (ERLs) are advected by a northerly wind from the Mogollon Rim to the 800–650-mb layer over Phoenix by early evening. An ERL is defined as a boundary layer, which may or may not be well-mixed, that forms initially over elevated terrain and is later advected over boundary layers developing over lower terrain (Stensrud 1993). In both cases, rawinsondes launched three times between the late afternoon and early evening in

Phoenix, show a warming and drying of the air between 800–650 mb, which decreases the convective potential substantially. The suppression of storm development over Phoenix owing to an ERL is emphasized by a case where storms fail to develop even though a convergence boundary, produced by thunderstorms moving off the mountains toward Phoenix, moves across Phoenix without new storm development (Stensrud 1993). Since the associated ERL increased the Convective Inhibition (CIN) from an expected value of 87 J kg^{-1} to 264 J kg^{-1}, it appears that stability within the planetary boundary layer is regulated, in part, by layers of air advected above this boundary layer during the diurnal cycle.

At times, more dramatic processes influence the potential for storm development. For example, McCollum et al. (1995) discuss an event where significant changes in characteristics of Phoenix sounding and surface data occur over just a few hours. During the 1990 SWAMP, both NWS and National Severe Storms Laboratory staff forecast incorrectly a dry evening over Phoenix on 23 July 1990—when instead a mesoscale convective system (MCS) developed. Later, detailed analyses of surface data, Phoenix soundings, and pibal wind reports from northern Mexico, suggested that a southerly LLJ bolstered low-level moisture and instability values. In combination with vertical motion arising from interactions between thunderstorm outflows moving into the desert, and opposing southerly flow south of Phoenix, such short-term changes made the Phoenix environment conducive to the development of a nocturnal MCS.

2.4 Summary

The circulations of the NAM are instrumental to summer storm development in Arizona. At low-levels, the temperature and pressure gradient between the southwest U.S. thermal low and the mesohigh over the mouth of the Gulf of California, constricted zonally by surrounding mountains, channels moist southerly flow in the form of a nocturnal LLJ—a flow intensified occasionally in the form of a surge. At mid–upper levels, the southeasterly-to-southerly flow over western Mexico and Arizona, respectively, transports water vapor into Arizona.

Within this environment, periods of wet and dry weather occur in response to variations in the synoptic-scale flow (Carleton 1986; Watson et al. 1994a; Mullen et al. 1998; Wallace 1997; Wallace et al. 1999). Although such burst and break studies find differences in synoptic-scale flow associated with wet vs. dry periods, the operational utility of such studies remains unverified. Unfortunately, burst and break studies provide little forecast guidance concerning where, when, and how storms may evolve on a given day. Mechanisms for storm development are addressed by a few Arizona case studies. These studies point to the importance of interactions between mountainous terrain and mid-level wind direction (Fujita 1962), mechanism for destabilization of the planetary boundary layer (Hales 1977; Stensrud 1993; McCollum et al. 1995), and interactions between thunderstorm outflows and the ambient desert flow (Watson et al. 1994b; McCollum et al. 1995), for supporting convective storm development.

22

The purpose of this study is to investigate the *variability* in daily storm development patterns and the tropospheric environment in Arizona during two NAM seasons, and, in turn, improve forecast guidance concerning where, when, and how storms may evolve on a given day. In the next section, this investigation begins by using radar mosaics to study daily storm development patterns.

3. Radar Reflectivity Regimes

In this section, variability in summer storm development in Arizona is investigated using radar reflectivity data. First, Section 3.1 describes the radar data and techniques used to construct high-resolution reflectivity mosaics. Second, Section 3.2 outlines the method used to assess variability of storm development. Third, Section 3.3 describes the five storm development patterns found from this analysis.

3.1 Radar Data and Methodology

Weather Surveillance Radar-1988 Doppler (WSR-88D) level II radar reflectivity data, collected from the Phoenix (KIWA) and Flagstaff (KFSX) sites, are used to investigate variability in diurnal storm development over Arizona. Radar reflectivity data from two NAM seasons, July and August 1997 and 1999, are examined. Although this study examines two NAMs only, it provides the first examination of intraseasonal variability using radar reflectivity data. During these periods, WSR-88D data are available for 111 of the 124 days (~90% of events), with 12 days (2 days) missing from the 1997 (1999) data set. The analysis period begins in 1997 because it is the first year where radar data are available from both the Phoenix and Flagstaff WSR-88D sites. As discussed in detail below, these radar sites are used to create radar reflectivity composites. Analyses span from July through August because precipitation associated with the NAM usually begins in early July, and dissipates during September (Sellers and Hill 1974). Since this study is also concerned with the variability in the tropospheric environ-

ment, the 1998 summer season is excluded owing to large gaps in archived sounding data at Phoenix.

Quality control techniques are applied to minimize echo from non-meteorological sources, including ground clutter and anomalous propagation. In this quality control process, a gate of radar reflectivity is considered ground clutter if its height is below the height of the hybrid reflectivity level (Gourley et al. 2001). The hybrid reflectivity level is defined as the height where one of the four lowest radar tilts is at least 500 ft above ground level (see Fig. 5 for heights of the KIWA and KFSX hybrid scan; Fulton et al. 1998). As illustrated in Fig. 5, the height of the hybrid reflectivity level increases most quickly with increasing range in regions where terrain blocks the radar beam.

A radar reflectivity observation is considered anomalous propagation, or surface-ducting of the radar beam, if it is nearly stationary (corresponding velocity magnitude is less than or equal to 2.5 ms^{-1}) and the magnitude of the reflectivity value above the observation is comparatively small (Gourley et al. 2001). Specifically, significant decreases in reflectivity with height are considered non-meteorological if the following condition is satisfied: $\dfrac{(ref_H - ref_{H+1})}{ref_H} \geq 0.9$, where

ref_H is the reflectivity value in a bin at the hybrid tilt height, and ref_{H+1} is the reflectivity value in a bin at the tilt above the hybrid level (Gourley et al. 2001).

Thus, this second criteria is met when ref_{H+1} is at least 90% smaller than

ref_H. Radar reflectivity data identified as ground clutter or anomalous propaga-

tion are removed from the data set.

Once data quality control is completed, the polar-coordinate radar

reflectivity volumes from each radar are interpolated to a three-dimensional (3-D

Cartesian grid (Zhang 2000). The Cartesian grid has a cylindrical equidistant lati-

tude/longitude reference frame, such that only distance along standard parallels

and meridians are true to scale. The Cartesian grid is 440 km x 440 km in the hor-

izontal dimension (Fig. 1b), with 1-km grid spacing in the horizontal and 21

stretched levels in the vertical (surface to 12 km), such that height intervals

increase hyperbolic-tangentially with increasing height.

The raw reflectivity factor, f, is interpolated from polar coordinates,

$f_i(r, \theta, \phi)$, to Cartesian coordinates, $f_g(x, y, z)$, by performing an adaptive Bar-

nes interpolation scheme (e.g., Trapp and Doswell 2000):

$$f_g(x, y, z) = \frac{\sum\limits_{i}^{N} w_i f_i(r, \theta, \phi)}{\sum\limits_{i=1}^{N} w_i}, \tag{1}$$

where the weighting factor w_i is defined as:

$$w_i = \exp\left[-\frac{(r_g - r_i)^2}{\kappa_r} - \frac{(\theta_g - \theta_i)^2}{\kappa_\theta} - \frac{(\phi_g - \phi_i)^2}{\kappa_\phi}\right], \qquad (2)$$

where r, θ, ϕ represent polar coordinates of distance, azimuth, and elevation, x, y, z represent Cartesian coordinates of horizontal distance and height, the subscripts i and g represent a bin of raw reflectivity data in polar and Cartesian coordinates, respectively, N is the number of radar bins influencing the interpolated grid value, and κ_r, κ_θ, and κ_ϕ are the dimensional filtering parameters. These
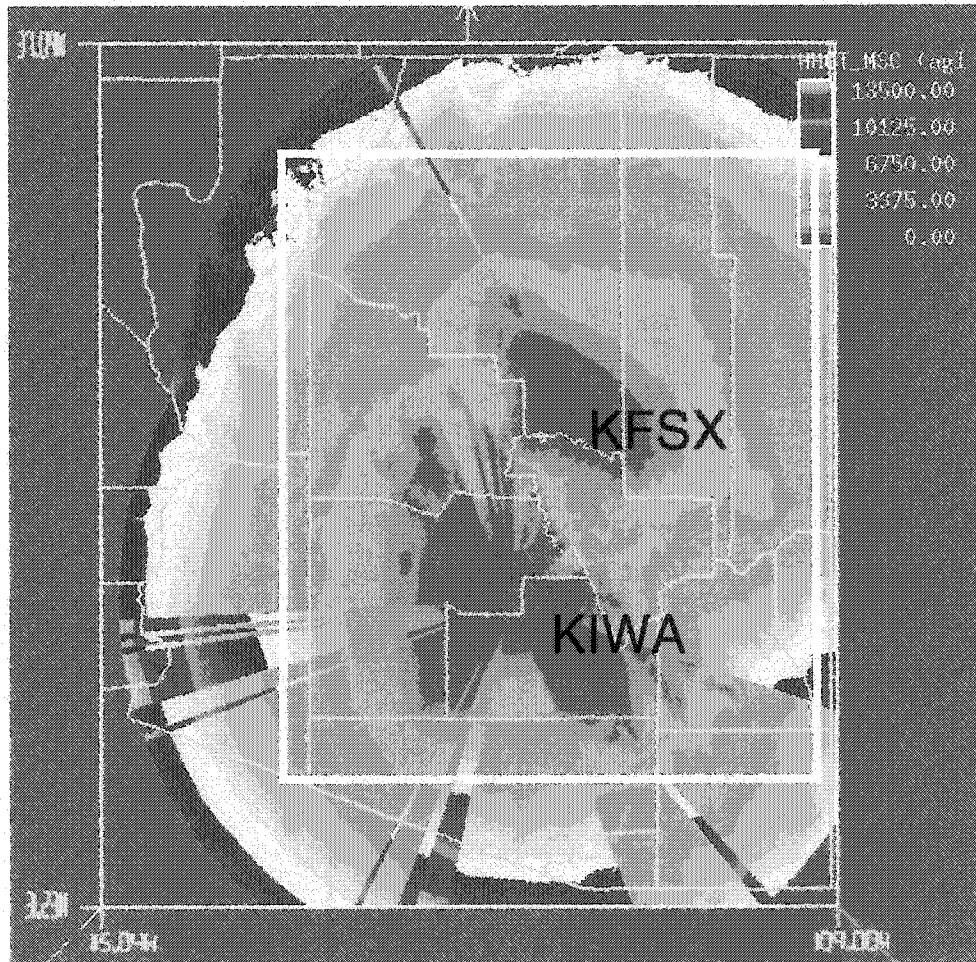
Figure 5. Height of hybrid scan, or lowest elevation above 500 ft (152 m) where data are collected for KIWA and KFSX WSR-88Ds (m AGL). The white box denotes this study's domain.

27

dimensional filtering parameters are a function of r only, and are defined in Appendix A.

The influence region of $f_g(x,y,z)$ is volumetric, and is defined in polar coordinates, such that radar bins located within 5 km radial distance, two degrees azimuth, and within the two closest elevation scans above and below the grid point, contribute toward that point's weighted reflectivity value. Since the resolution of radar reflectivity data decreases in azimuthal and vertical directions with increasing range from the radar, the region of influence applied to grid points located far from the radar is larger than the region of influence applied to grid points located near to the radar, but includes the same number of data points. Since azimuthal- and elevation-length scales increase with increasing range, filtering ($\kappa_\theta(r)$ and $\kappa_\phi(r)$) is range-dependent in these dimensions. The range dependence of filtering, and hence the three-dimensional response function, is exemplified in Appendix A.

In contrast to the adaptive Barne's interpolation scheme applied here, Trapp and Doswell (2000) prefer non-adaptive Barnes interpolation schemes. The main difference between adaptive and non-adaptive Barne's interpolation schemes is that the non-adaptive scheme applies fixed length scales in both azimuthal and vertical directions. Trapp and Doswell (2000) suggest choosing fixed length-scales at the outermost radial range of a particular analysis. By doing so,

the highest-resolution reflectivity data, close to the radar, are lost, but the weight functions are independent in range. As a result, the growth or decay of a storm moving toward or away from the radar may be determined with greater certainty than that available from adaptive techniques. Since this study is concerned primarily with general patterns of radar reflectivity frequencies above a specified reflectivity threshold, effects of storm growth and decay are assumed minimal.

Once each volume scan of reflectivity from the KIWA and KFSX radars is interpolated to the Cartesian grid, a 3-D reflectivity mosaic is created by combining radar data at each Cartesian level, z. Use of two radars minimizes radar data limitations such as beam blockage and decreasing resolution with increasing range, and composes a more complete depiction of storm structure and precipitation than either radar alone could provide. At each level z, interpolated reflectivity values, $f_g(x,y,z)$, are mosaiced to each grid point, $f_m(x,y,z)$, in the domain using an inverse distance-weighted average (Zhang 2000):

$$f_m(x, y, z) = \frac{\displaystyle\sum_{n=1}^{nradars} w_n(x, y, z) f_g^n(x, y, z)}{\displaystyle\sum_{n=1}^{nradars} w_n(x, y, z)}, \tag{3}$$

where *nradars* is the number of radars that cover each grid point (here *nradars=* 2), $f_g^n(x,y,z)$ is the interpolated reflectivity value from the *nth* radar, and $f_m(x,y,z)$ is the mosaiced value at each grid point. The weight, w_n, given to a radar observa-

tion is dependent on the distance between the radar and the observation (i.e.,

Cressman weight function; Zhang 2000):

$$w_n(x, y, z) = \frac{R_{inf}^2 - d_n^2(x, y, z)}{R_{inf}^2 + d_n^2(x, y, z)}, \qquad (4)$$

where R_{inf} is the farthest range at which a valid observation is attainable ($R_{inf} =$

300 km), and $d_n(x,y,z)$ is the distance between a mosaic grid point and the nth

radar. The final 3-D radar reflectivity mosaic is created every 10 min. A composite

reflectivity mosaic is also computed, which compresses the 3-D Cartesian grid to

a 2-D field of maximum reflectivity value within each 1-km x 1-km x 12-km column.

This 2-D composite reflectivity mosaic is used to investigate the variability of

storm development over Arizona.

3.2 Assessing the variability of storm development

Arizona's summer diurnal precipitation climatology indicates a cycle of

storm development from higher to lower terrain during the afternoon and into the

early evening, culminating in the Sonoran Desert at night. This climatology pro-

vokes at least two questions: 1) How often does a this diurnal precipitation cycle

occur over Arizona? and 2) What variety of diurnal storm development patterns

tend to occur over Arizona? Answers to these questions are needed to build an

understanding of daily storm development variability in Arizona.

The variability in diurnal storm development patterns is investigated by examining daily storm evolution. First, for each day (a day is defined as the 24-hr period beginning at 12 UTC), the diurnal relative frequency of composite mosaics of reflectivity greater than or equal to 25 dBZ is calculated, beginning at the top of each hour. The 25 dBZ threshold serves as a proxy for storm development. Second, animated loops of hourly relative frequency maps for each day are observed repeatedly, to assess the variability in diurnal storm development. By observing these relative frequency maps, it becomes apparent that similar diurnal storm evolutions occur repeatedly over different geographic regions. For instance, on some days, storms develop over mountains in eastern Arizona only, whereas on other days storms develop over mountains in eastern Arizona and along the Mogollon Rim. On other days, storms evolve in a manner similar to the diurnal precipitation climatology. The fidelity of such repeated diurnal storm evolutions is elucidated by computing diurnal 3-hourly relative frequencies (e.g., 12–14 UTC, 15–17 UTC, 18–20 UTC, etc.) of composite radar reflectivity, 25 dBZ and higher, from the 10 min mosaics for days comprising diurnal storm cycles over similar geographic areas, and then manually comparing similarities and differences in spatial and temporal patterns. The results of this analysis are reported next.

3.3 Reflectivity Regimes

Five repeated storm development patterns, or regimes (Table 1) are found over the domain. In four of the five reflectivity regimes, composite reflectiv-

ity evolves repeatedly over similar geographic regions, including: 1) eastern mountains (called eastern mountain regime (EMR);12 days or 10% of events), 2) central and eastern mountains (called central and eastern mountain regime (CEMR); 35 days or 28% of events), 3) central mountains, eastern mountains, and Sonoran Desert (called central mountains, eastern mountains, and Sonoran regime (CEMSR); 22 days or 18% of events), and 4) none of the domain (called dry regime (DR); 13 days or 10.5% of events).

The fifth regime is distinguished by storm development that is less closely tied to the climatological diurnal cycle, and therefore is called the non-diurnal regime (NDR). Such events occur on 23 days, or 18.5% of the time, and are depicted by storms that move across Arizona with the prevailing steering-level flow, including westerlies, easterlies, and southerlies. Owing to such differences in storm movement, days within this regime are subcategorized according to direction of storm movement, including northward moving (NDR-N;11 days or 48% of widespread events), eastward moving (NDR-E; 7 days or 30% of widespread events), and westward moving (NDR-W; 5 days or 22% of widespread events). Six days or 5% of events occur over various isolated areas in Arizona (called unclassified), and thirteen days or 10.5% of the radar data set are missing. Both unclassified and missing events are excluded hereafter, such that 111 of 124 possible events are examined.

Table 1: Distribution of reflectivity regimes during the 1997 and 1999 NAMs, where DR is the dry regime, EMR is the eastern mountain regime, CEMR is the central–eastern mountain regime, CEMSR is the central–eastern mountain and Sonoran Desert regime, NDR is the non-diurnal regime, UNC is the unclassified regime, and MISS is days missing from the radar dataset. Shaded columns highlight the two regime types that occur most frequently in 1997 and 1999.

	DR	EMR	CEMR	CEMSR	NDR	UNC	MISS
July–August 1997	9 (14%)	6 (10%)	13 (21%)	7 (11%)	9 (16%)	6 (10%)	12 (18%)
July–August 1999	4 (6%)	6 (10%)	22 (36%)	12 (19%)	16 (26%)	0 (0%)	2 (3%)
Total	13 (11%)	12 (10%)	35 (28%)	19 (15%)	25 (20%)	6 (5%)	14 (11%)

The repeated diurnal storm evolutions elucidated by computing 3-hourly frequencies of composite radar reflectivity during the period of peak storm development (i.e. 18–09 UTC), for each regime, are described below. The resulting patterns affirm the classification of repeated storm development patterns over different geographic regions in Arizona.

3.3.1 Eastern Mountain Regime (EMR)

The eastern mountain regime is characterized by storm development over the mountains of eastern Arizona. Storms develop first in the vicinity of the White Mountains and the Southeast Highlands in the early afternoon (18–20 UTC; Fig. 6a). By mid-afternoon the areal extent of storm development is maximized, as storms begin to move toward lower elevations (22–00 UTC; Fig. 6b). Toward evening, storm development is most frequent over the Southeast Highlands (02–

04 UTC; Fig. 6c), and by early morning storm development has ceased (06–08 UTC; Fig. 6d).

Compared to other precipitating regimes, EMR occurs least frequently (only 10% of the time) and evolves over the least amount of terrain. Also, EMR's frequencies of radar reflectivity are comparatively low. These lower relative frequencies may indicate high spatial and temporal variability in storm development within a relatively small sample size.

3.3.2 Central–Eastern Mountain Regime (CEMR)

The central and eastern mountain regime is characterized by storm development over the Mogollon Rim, White Mountains, and Southeast Highlands (Fig. 7). Storms develop first over the peaks of the Southeast Highlands and the higher elevations of the Mogollon Rim, such that a linear relative frequency pattern extends from the White Mountains to the San Francisco mountains (18–20 UTC; Fig. 7a). Like EMR, by mid-afternoon the areal extent of storm development is maximized, as storms begin to move toward lower elevations (22–00 UTC; Fig. 7b). Toward evening the areal extent of storm development over the Mogollon Rim is greatly diminished, while storms continue to move away from the Southeast Highlands (02–04 UTC; Fig. 7c). By early morning storms infrequently occur over the Southeast Highlands and White Mountains (06–08 UTC; Fig. 7d).

Compared to other regimes, the CEMR occurs most frequently (28% of the time), demonstrating the environment's propensity for storm development over mountainous terrain. The major difference between the CEMR and EMR is the expanded storm development across the Mogollon Rim and larger areas of higher relative frequencies (7–14% vs. 3–5%) of radar reflectivity over elevated terrain (cf. Figs. 6 and 7).

3.3.3 Central–Eastern Mountain and Sonoran Regime (CEMSR)

The CEMSR is characterized by initial storm development over the Mogollon Rim, Southeast Highlands, Central Mountains, and later development over the Sonoran Desert (Fig. 8). Storms develop first over the higher elevations of the San Francisco Mountains, Mogollon Rim, White Mountains, Southeast Highlands, and Central Mountains during the early afternoon (18–20 UTC; Fig 8a). This early afternoon storm development is more widespread over mountainous terrain compared to the CEMR, and there is a tendency for higher relative frequencies of radar reflectivity along the Mogollon Rim (11–14% vs. 7–10%) and in the vicinity of the White Mountains and San Francisco Mountains (15–18% vs. 7–10%; cf. Figs. 7a and 8a). By mid-afternoon the region of relative frequencies has expanded to the north and south and their magnitude has intensified along the ranges of the Central Mountains (20–00 UTC; Fig. 8b). Compared to the CEMR, this band of high relative frequencies is more distinct and intense, and relative frequencies of
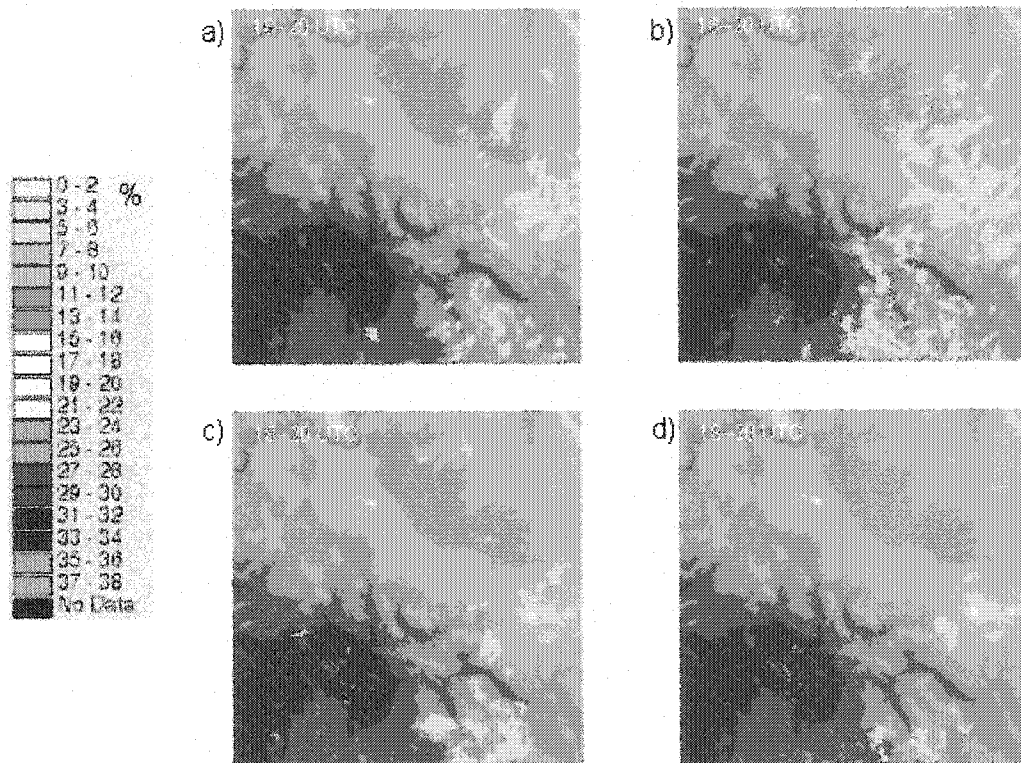
Figure 6. Three-h relative frequencies of radar reflectivity 25 dBZ and higher for EMR at a) 18–20 UTC, b) 22–00 UTC, c) 02–04 UTC, and 06–09 UTC.
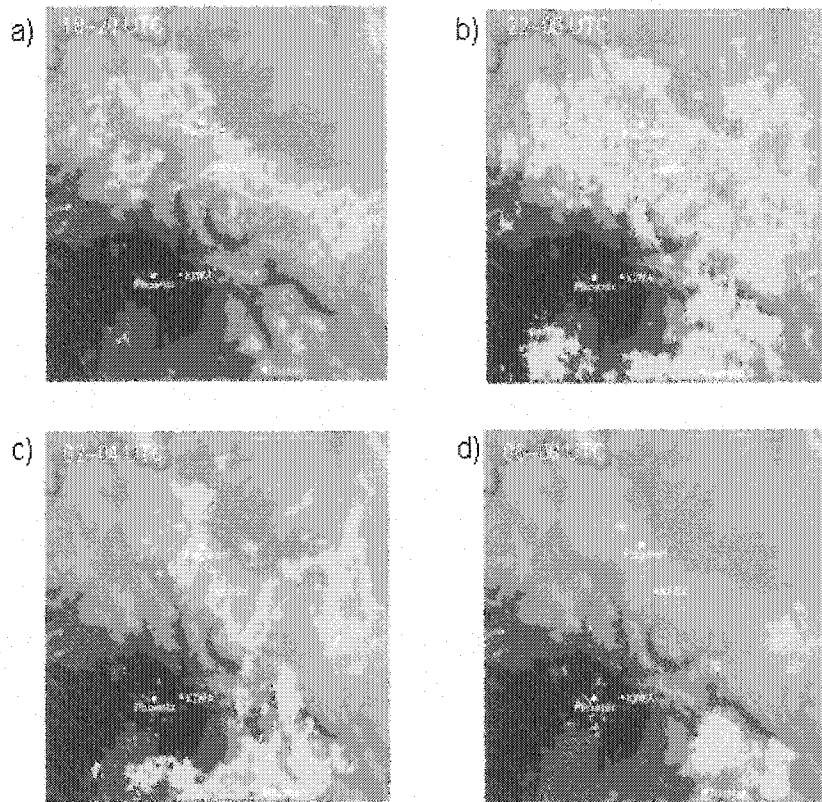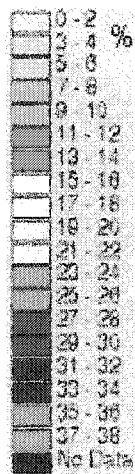
Figure 7. Same as in Fig. 6, except for CEMR.

radar reflectivity are higher and more widespread along the periphery of the Sonoran Desert (cf. Figs. 7b and 8b). This more intense band of high relative frequencies, compared to CEMR, reflects the tendency for more organized storm development during CEMSR. Indeed, studies of 10 min reflectivity mosaic loops show that cell mergers and storm outflows are more prolific during CEMSR than CEMR.

Unlike EMR and CEMR, toward evening storm development is abundant over the Central Mountains, Southeast Highlands, and the Sonoran Desert (02–04 UTC; cf. Figs. 6c, 7c, and 8c), with secondary relative frequency maximum in the vicinity of the Southeast Highlands and southwestern and western parts of the Sonoran Desert. By early morning storm development is diminished over the Central Mountains but remains somewhat active over the Southeast Highlands and the Sonoran Desert (Fig. 8d). The storm evolution of this regime is similar to that depicted by Arizona's diurnal climatology: capturing both the afternoon precipitation maxima over elevated terrain and the late night precipitation maxima over the Sonoran Desert (Balling and Brazel 1987; King and Balling 1994; Watson et al. 1994b). Since three of the four precipitating regimes involve storm development over elevated terrain during the afternoon, the similarity between EMR, CEMR, CEMSR and climatology is hardly surprising.

The CEMSR occurs less frequently (18% vs. 28% of the time) than

CEMR, indicating that ingredients for storm development are present in the Sono-

ran Desert less often than over elevated terrain. The major difference between
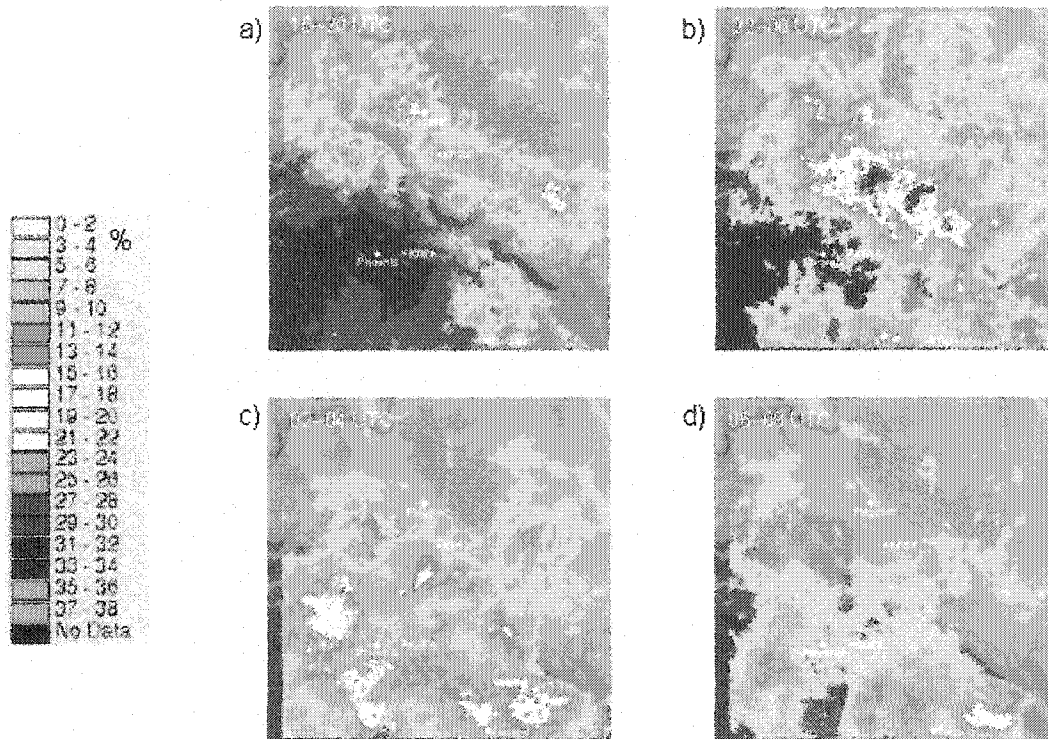
Figure 8. Same as in Fig. 6, except for CEMSR.

CEMSR and CEMR during the afternoon is more frequent storm development across the Mogollon Rim, and especially the Southeast Highlands and Central Mountains which surround the Sonoran Desert.

3.3.4 Nondiurnal Regime (NDR)

The non-diurnal regime (NDR) regime is characterized by storm development that is tied less strongly to the topographically-influenced diurnal precipitation cycle than the previous three regimes (EMR, CEMR, and CEMSR; cf. Figs. 6–9). Although relative frequencies of radar reflectivity show early-afternoon storm development over higher terrain, including western portions of the Central Mountains and Mogollon Rim, and Southeast Highlands, storms may also occur over the Painted and Sonoran Deserts (18–20 UTC; Fig. 9a). By mid-afternoon, storm development is most frequent the Sonoran Desert (maximum of 19–22%), and less frequent over most of the Mogollon Rim, Central Mountains, Southeast Highlands, and Painted Desert (22–00 UTC; Fig. 9b). Such afternoon storm development is unique because, climatologically, storm development over the Sonoran Desert is most frequent late at night. This maximum in afternoon storm development suggests that forcing mechanisms, in addition to terrain-forcing, are significant. By early evening, storm development is most frequent over the Sonoran Desert and Southeast Highlands (11–14%), with lower frequencies over the
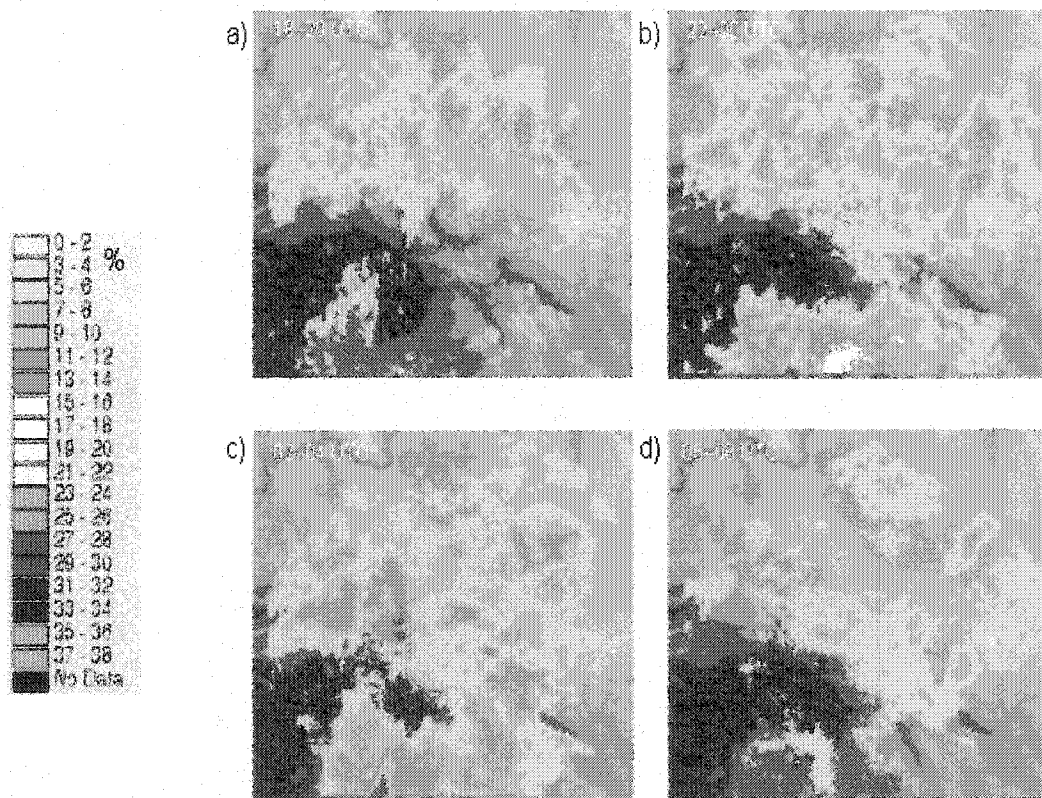
Figure 9. Same as in Fig. 6, except for NDR.

Central Mountains, Mogollon Rim, and Painted Desert (3–10%; 02–04 UTC; Fig. 9c). In the early morning, storm development is most frequent over regions within the Central Mountains and Painted Desert (7–10%), and infrequent over most of the Sonoran Desert and Southeast Highlands (06–08 UTC; Fig. 9d). Although NDR's diurnal cycle of reflectivity frequency highlights the unique development of afternoon storms over the Sonoran Desert, on a given day, storm development can differ markedly from that described above. Variations in diurnal storm development arise owing to variability in storm movement, which may be categorized as northerly, easterly, or westerly on each day. In general, these storm systems are well organized, developing linear bands of convective cells that move with the mean flow.

The NDR occurs 20% of the time, a percentage slightly higher than that found for CEMSR (15%). In both regimes, diurnal frequencies of reflectivity exhibit storm development over the Sonoran Desert, with maxima in the late afternoon and evening hours. To verify further the propensity for precipitation over the Sonoran Desert during NDR and CEMSR, compared to DR, EMR, and CEMR, distributions of 24-h rainfall data associated with each regime are examined from the Automated Local Evaluation in Real Time (ALERT) rain gage network (http://www.fcd.maricopa.gov/alert/alert.hml) within Phoenix-Mesa and the surrounding desert area. This region is defined by a domain extending latitudinally from 32.83°–33.76°, and longitudinally from -111.39°– -113.12°. For each regime, percentiles of rainfall (0.5–0.95) are computed using the 1997 and 1999 ALERT data.

As expected, no measurable precipitation is reported during DR or EMR (not shown). Measurable (nonzero) precipitation during CEMR appears first at the 95th percentile, with a measly value of 0.04 in (Fig. 10). In contrast, nonzero precipitation values appear lower in the NDR and CEMSR distributions, at the 70th and 75th percentiles, respectively (Fig. 10). Thus, 4.8 (2.6) times more stations reported 24 h accumulated precipitation of 0.04 in or higher during NDR (CEMSR) than CEMR. Furthermore, NDR's and CEMSR's 95th percentiles are at least eleven times higher than those reported during CEMR. In conclusion, the relative lack of 24 h accumulated precipitation over the northern Sonoran Desert and Phoenix–Mesa region strengthens the radar-only-based regime classification depicted above.

3.6 Summary

Repeated storm development over the Mogollon Rim, Southeast Highlands, and Central Mountains illustrates the importance of terrain forcing in the initiation of moist convection in Arizona during the summer. Differences in geographic regions where storms develop repeatedly suggest that corresponding variations in environmental conditions may exist which help discern one regime from another. In the next section, this hypothesis is addressed by examining and comparing characteristics of composite upper-air maps and 12 UTC soundings at Phoenix associated with these regimes.
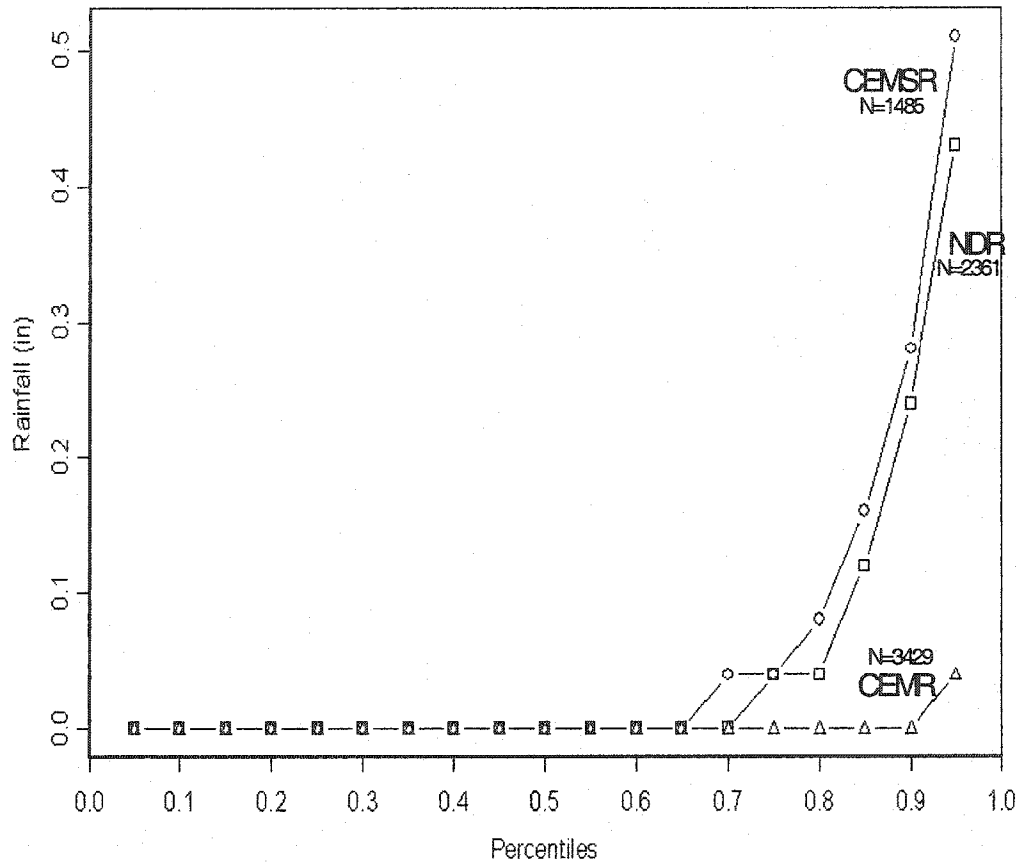
Figure 10. Percentiles of 24-h rain amountsl (in) from the ALERT network, associated with CEMR (N=3429), CEMSR (N=1485), and NDR (N=2361).

4. Environmental conditions associated with regimes

Three ingredients necessary for deep moist convection include moisture, lift, and instability (Johns and Doswell 1992). Regional and temporal differences in storm coverage associated with reflectivity regimes suggest that intrinsic variability in these ingredients may be related to the synoptic-scale flow. This speculation is investigated by analyzing characteristics of synoptic-scale flow over the southwest US and local tropospheric conditions at Phoenix associated with each regime.

4.1 Composite upper-air maps

Composite 12 UTC maps of 500-mb geopotential height and specific humidity are employed to explore mean upper-air conditions associated with each regime. These composites are constructed using National Center for Environmental Prediction / National Central for Atmospheric Research (NCEP/NCAR) Reanalysis data (Kalnay et al. 1996) at the Climate Diagnostic Center's Web site (http://www.cdc.noaa.gov). Characteristics of the composite map for each regime are described below, in order of increasing storm coverage.

During the dry regime (DR), flow at 500 mb is dominated by a low-amplitude ridge and relatively dry air, especially over southern California, Nevada, and Arizona (Fig. 11). These conditions result from the location of the subtropical

45

high's horizontal ridge axis: 30°N. This pattern is similar to break composites found by Carleton (1986), Watson et al. (1994a), and Mullen et al. (1998).

The 500-mb composites for the remaining "wet" regimes differ from DR in at least two significant ways. First, the horizontal ridge axis of the subtropical high is located farther northward, making the flow predominantly meridional rather than zonal (e.g., southerly rather than westerly; cf. Figs. 11 and 12–15). Second, owing to this southerly flow, the meridional moist axis expands farther northward than on dry days (cf. Figs. 11 and 11–15). Although these characteristics correspond well with Carleton's (1986) and Watson et al.'s (1994a) burst composites, it is possible to discriminate more precisely among different regimes based on synoptic-scale flow.

During the eastern mountain regime (EMR), Arizona is located just west of a confluence zone that marks the transition in flow between the drier air of the North Pacific trough and the more moist air of the subtropical high (Fig.12). This transition zone is known as the monsoon boundary (Adang and Gall 1989). Adang and Gall (1989) show that this boundary extends vertically from the surface to 400 mb, and is associated with a relatively weak temperature gradient. Conditionally unstable, warmer air is located east of the boundary (Adang and Gall 1989). By applying the two-dimensional, geostrophic momentum version of the Sawyer–Eliassen equation (Shapiro 1981), Adang and Gall (1989) show that
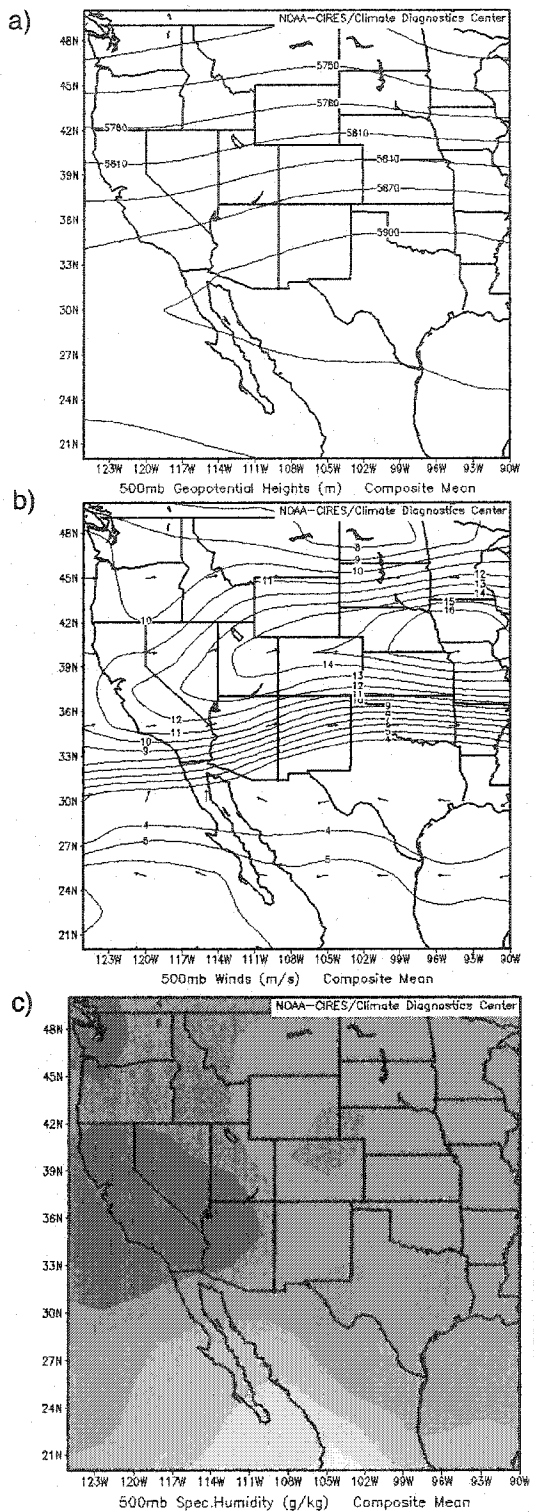
Figure 11. Composite 500-mb map of a) geopotential height (m), b) vector winds (m s^{-1}), and c) specific humidity (g kg^{-1}) for the dry regime (DR). Image provided by the NOAA-CIRES Climate Diagnostics Center, Boulder, Colorado from their Website at http://www.cdc.noaa.gov.

these gradients of temperature and moisture are forced by confluence, $2\dfrac{\partial u_g}{\partial p}\dfrac{\partial v_g}{\partial y}$,

rather than by geostrophic horizontal shear, $-2\dfrac{\partial u_g}{\partial y}\dfrac{\partial v_g}{\partial p}$. Confluence is also the

primary forcing function responsible for the associated direct ageostropic stream-function, with rising (descending) air east (west) of the boundary (Fig. 9 of Adang and Gall 1989). Since the monsoon boundary is located near eastern Arizona during EMR, conditions are favorable for storm development over the eastern mountains, where orographic and/or thermal forcing may be enhanced by rising moist air from the ageostrophic circulation.

The composite synoptic-scale flow associated with the central–eastern mountain regime (CEMR) is dominated by a large-scale anticyclone (i.e., subtropical high), centered over the Texas Panhandle (Fig. 13). This flow is accompanied by a broad meridional axis of moist air, centered along the Arizona/New Mexico border (Fig. 13). The similarity of this synoptic-scale pattern to the EMR composite suggests the same processes as before, only shifted westward and expanded in scale. This change in environment implies conditions favorable for storm development over both the central and eastern mountains (cf. Figs. 12 and 13).

During the central–eastern mountain and Sonoran regime (CEMSR), the composite 500-mb flow remains primarily anticyclonic over the southwest US, with a meridional axis of moist air centered over the border of Arizona and New Mexico

a) 500mb Geopotential Heights (m) Composite Mean

b) 500mb Winds (m/s) Composite Mean

c) 500mb Spec.Humidity (g/kg) Composite Mean
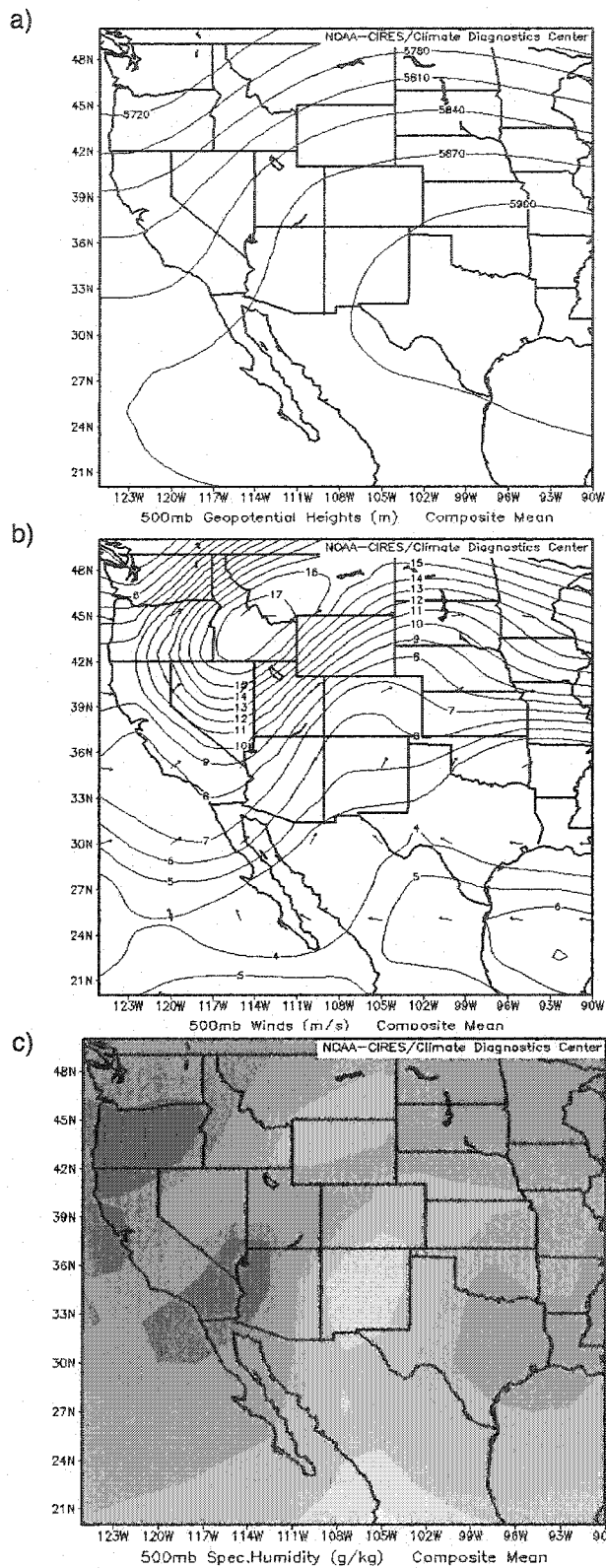
Figure 12. Same as Fig. 11, only for the eastern mountain regime (EMR).

a)

500mb Geopotential Heights (m)   Composite Mean

b)

500mb Winds (m/s)   Composite Mean

c)

500mb Spec.Humidity (g/kg)   Composite Mean
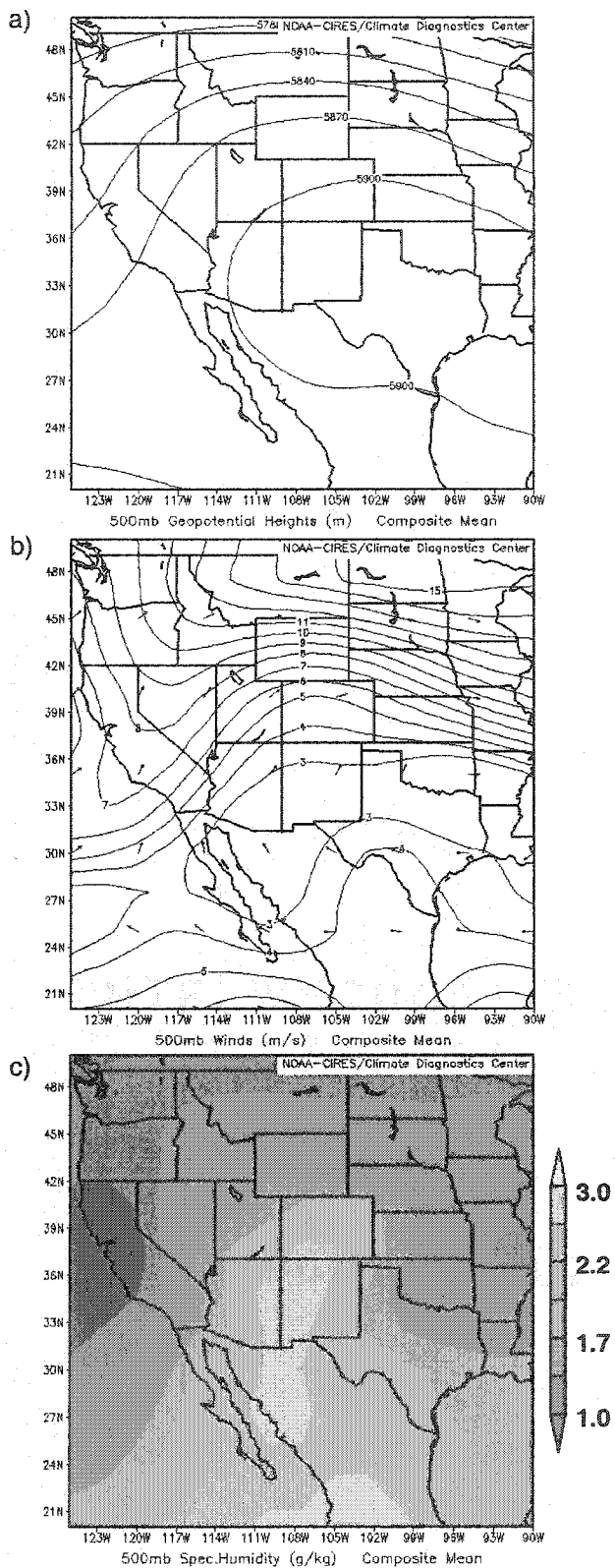
Figure 13. Same as Fig. 11, only for the central–eastern mountain regime (CEMR).

a)

500mb Geopotential Heights (m)   Composite Mean

b)

500mb Winds (m/s)   Composite Mean

c)

500mb Spec.Humidity (g/kg)   Composite Mean
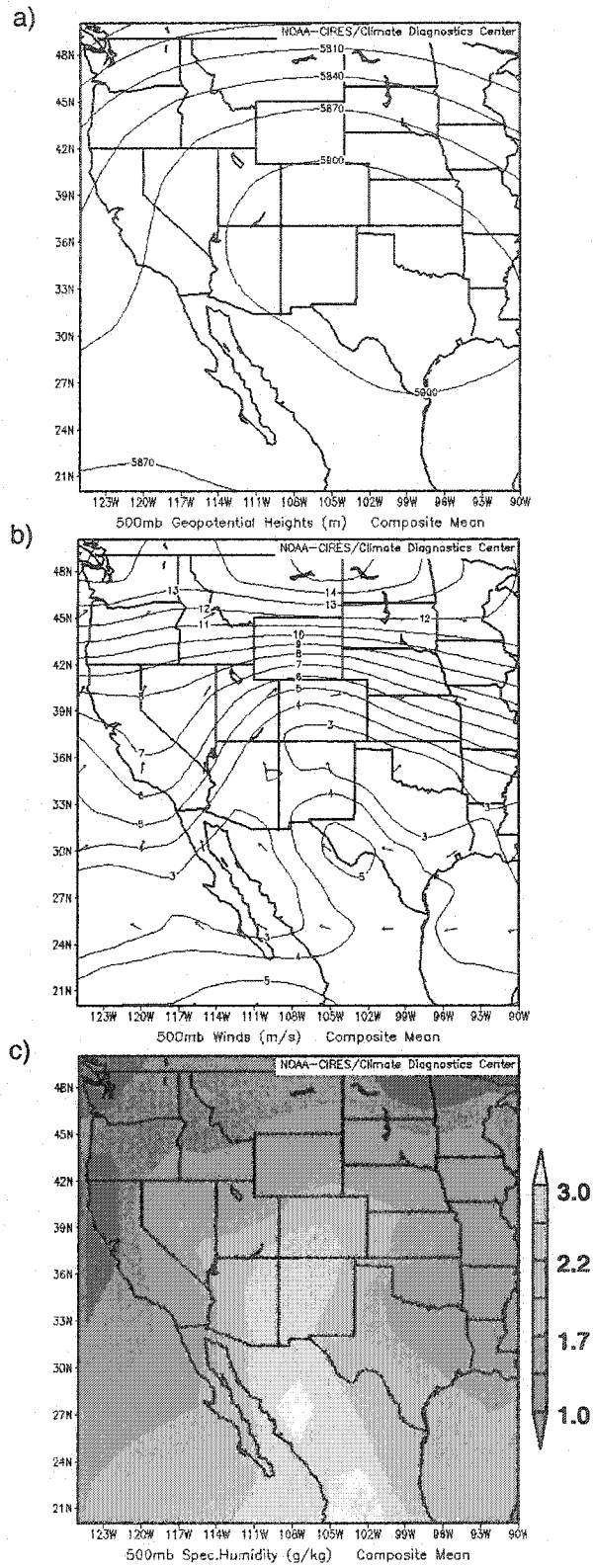
Figure 14. Same as Fig. 11, only for the central–eastern mountain and Sonoran regime (CEMSR).

(Fig. 14). Although this pattern is similar to the 500-mb CEMR composite, the ridge is shifted slightly northward and its axis is tilted toward the northwest, creating a flow with a stronger easterly component (cf. Figs. 13 and 14). In addition, specific humidity values are slightly higher within the meridional moist axis in Mexico, and across Arizona (cf. Figs. 13 and 14). This incremental increase in moisture may create a midlevel environment more favorable for storm development within the Sonoran Desert. Since the motion of convective cells is tied to the vector mean wind within the cloud layer (e.g., Brooks 1946), the stronger easterly component found in the CEMSR composite, relative to the CEMR composite, is more favorable for storm movement from elevated terrain into the Sonoran Desert (cf. Figs. 13 and 14; Brooks (1946)). The relative importance of such differences is examined further in Section 4.2.

During nondiurnal regime (NDR), storm systems may move eastward, northward, or westward. Thus, synoptic-scale conditions are examined by creating a 500-mb composite for each type (Figs. 15a–c). A comparison of these composites reveals that, within each pattern, the meridional moist axis is centered over central Arizona and extends northeastward into Colorado. This small westward shift in the moist axis, relative to CEMR and CEMSR (e.g., cf. Figs. 14 and 15a), results in the availability of deep moisture across the entire domain, including the Sonoran Desert. Although the moisture field is similar among the three types, characteristics of their geopotential height composites differ. These patterns are discussed below.

a)

500mb Geopotential Heights (m)   Composite Mean

b)

500mb Winds (m/s)   Composite Mean

c)

500mb Spec.Humidity (g/kg)   Composite Mean
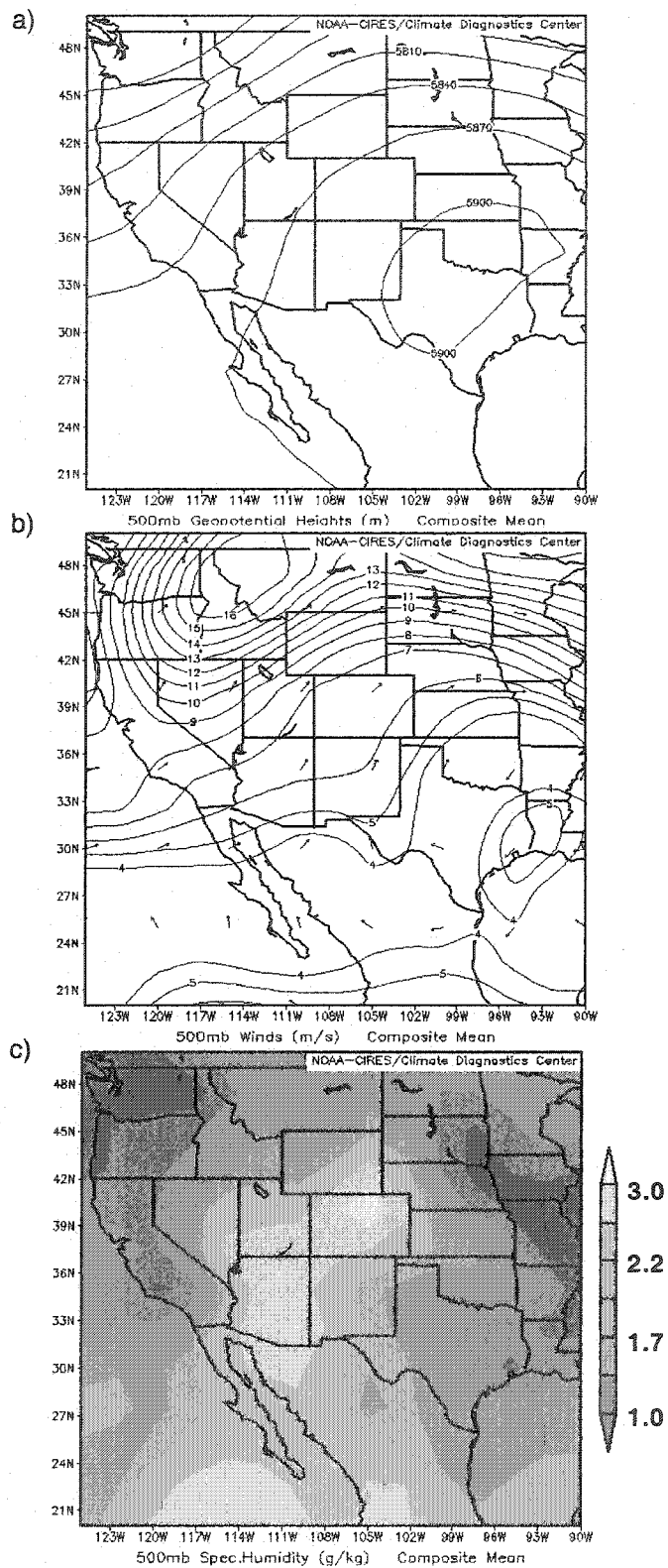
Figure 15a. Same as Fig. 11, only for the nondiurnal regime, where storm movement is eastward (NDR-E).

a)

b)

c)
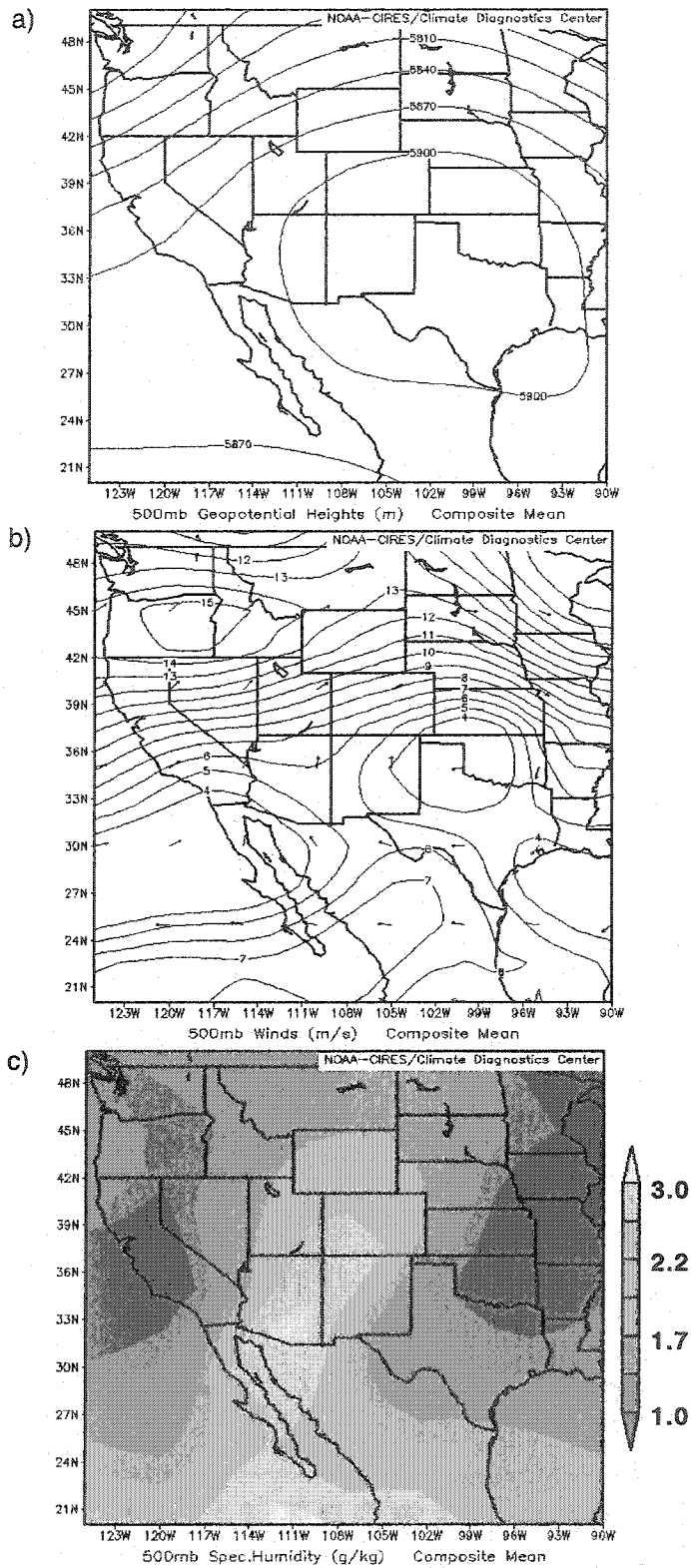
Figure 15b. Same as Fig. 11, only for the nondiurnal regime, where storm movement is northward (NDR-N).

a)
500mb Geopotential Heights (m)   Composite Mean

b)
500mb Winds (m/s)   Composite Mean

c)
500mb Spec.Humidity (g/kg)   Composite Mean
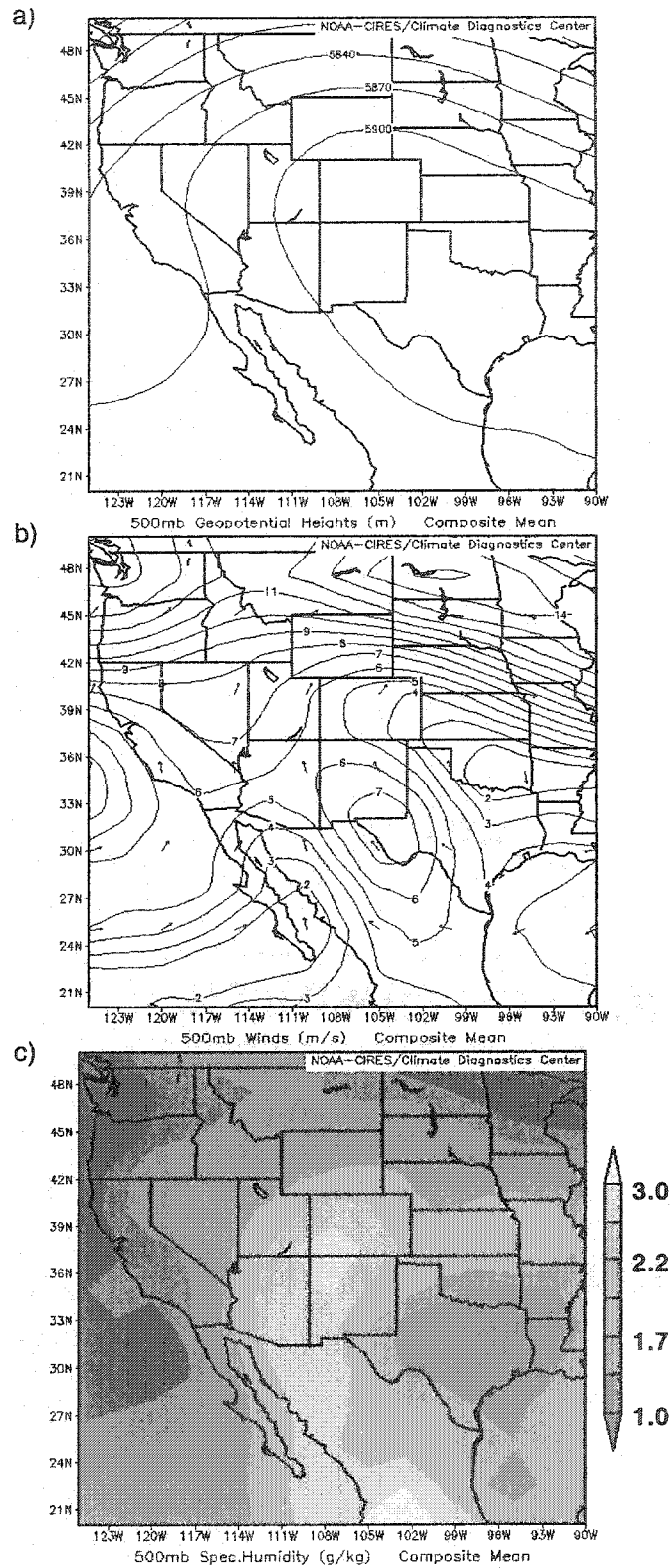
Figure 15c. Same as Fig. 11, only for the nondiurnal regime, where storm movement is westward (NDR-W).

55

During NDR days with eastward storm movement, a shortwave trough in the westerlies is located just west of Arizona and the subtropical high is centered over Oklahoma and Texas (Fig. 15a). This pattern is conducive to large-scale forcing ahead of the shortwave trough, which, in turn, may enhance instability and lift in a region where orographic and/or thermal forcing is prevalent and deep moisture is abundant. In addition, the southwesterly steering-level flow, and anticipated northeastward track of the shortwave trough, are likely responsible for the observed eastward storm movement.

On days where storms move northward, there is a broad high-amplitude ridge over the central plains and Rockies, separated from the North Pacific trough, by the monsoon boundary (Fig. 15b). Similar to EMR, CEMR, and CEMSR patterns, the meridional moist axis is located just east of this confluence zone, with drier air to its west (cf. Figs. 12 and 15b). This synoptic-scale pattern provides southerly flow over Arizona, which favors northward moving storms.

On days where storms move westward, the North Pacific trough and large-scale ridge are shifted eastward, relative to the north-moving storm composite (cf. Figs. 15b and 15c). In addition, the horizontal ridge axis is tilted toward the northwest, creating southeasterly flow favorable for westward storm movement. Interestingly, composite synoptic-scale patterns on northward- and westward-moving storm days are similar to CEMR and CEMSR composites, respectively (cf. Figs. 13 and 15b; cf. Figs. 13 and 14c). The most dramatic difference between these

nondiurnal regimes and CEMR and CEMSR is the westward shift and northward extension of the meridional moist axis. Given NDR's nondiurnal evolution of deep moist convection, another possible difference between NDR and CEMR or CEMSR is the contribution of nonorographic lifting mechanisms. Since storm development within NDR is fairly well organized, synoptic-scale forcing may play an important role. The shortwave trough in the westerlies, shown in the east-moving NDR composite (Fig. 15a), provides evidence of such synoptic-scale forcing. The role of synoptic-scale forcing in NDR is investigated below.

The importance of large-scale forcing during the nondiurnal regime is investigated by analyzing 12 and 00 UTC 500-mb maps of geopotential height and vorticity over the Southwest US during July and August 1997 and 1999. Large-scale forcing is considered relevant if storm development occurs within a region of differential vorticity advection within the 650–550-mb layer. Investigation of these conditions indicates that large-scale forcing for regimes occurs as follows: DR and EMR, absent (i.e., occurs 0% of the time), CEMR, 12.5% of the time, CEMSR, 70% of the time, and NDR, 88% of the time.

In summary, a study of 500-mb composites of geopotential height and specific humidity suggests that the occurrence of a given regime is connected to 1) the location of the North Pacific trough, monsoon boundary, and center of the subtropical high, 2) the location of the meridional moist axis, and 3) the presence or absence of vorticity maxima embedded in the flow. These findings emphasize

the importance of moisture and lift, or two of the three ingredients needed for deep moist convection over Arizona. The third ingredient, instability, is examined below using Phoenix soundings.

4.2 12 UTC Phoenix Soundings

Previous studies of thunderstorm development analyze Tucson soundings in hopes of improving forecasts of convective and nonconvective days in Phoenix (Wallace 1997; Wallace et al. 1999). They find that characteristics of 12 UTC Tucson soundings bear little relation to convective storm development in Phoenix (Wallace 1997; Wallace et al. 1999). The current study is the first to use Phoenix soundings to assess storm development. The 1997 dataset marks the first nearly complete record of sounding data recorded at Phoenix during the NAM, thanks to participants of SWAMP. Thereafter, the Salt River Project, a power company in Phoenix, began collecting sounding data at their facility. These data are now available operationally.

Morning sounding data (12 UTC) are used exclusively to study the pre-storm environment of various regimes. Soundings that are incomplete (e.g., missing wind profiles or deep layers of thermodynamic data), contaminated by precipitation, or lacking corresponding radar data are excluded, and the impact of outliers is diminished by applying a five-point filter to sounding data. Following this procedure, 89 soundings are available for analysis. The vertical structure of

Phoenix soundings associated with each regime's 500-mb composite map is investigated by constructing composite 12 UTC soundings. Each composite sounding is created by computing the average temperature, dewpoint, and wind vector, at each 25 mb level between 950 and 200 mb (e.g., 925, 900, 875 mb levels). In ideal circumstances, the distribution of temperature and dewpoint temperature at each examined level would be unimodal and leptokurtotic. However, in this study, the variance at most levels is too high to meet these criteria. Thus, these composite soundings do not represent the breadth of sounding characteristics associated with each regime. Regardless, characteristics of these composite soundings do exemplify general similarities and differences in stability, tropospheric moisture and wind among regimes.

4.2.1 Composite Soundings

One measure of instability is the magnitude of the low–mid-level lapse rate (e.g., 850–500 mb), where higher lapse rates indicate a more unstable atmosphere. A comparison of 850–500-mb lapse rates among the five regimes shows little variability, with values ranging from 7.1–7.5°C km^{-1}. Hence, differences in instability are not strongly tied to lapse rate. However, the potential release of this instability is tied, in part, to the amount of available tropospheric moisture. For example, given two soundings with the same lapse rate structure, the sounding with more moisture within low-levels (e.g., lowest 100 mb) will have higher values of convective available potential energy (CAPE) or buoyancy, once a parcel

reaches its level of free convection (LFC). Since the potential release of instability

is related to the amount of tropospheric moisture within low-levels, I examine dif-

ferences in mean layer CAPE (MLCAPE; calculated using lowest 100-mb layer)

among regimes. In addition, characteristics of tropospheric moisture and wind are

described and interpreted in light of the composite synoptic-scale flow discussed

in Section 4.1. Tropospheric moisture is measured by mean precipitable water

values (PWTR), defined as the total atmospheric water vapor contained in a verti-

cal column of unit cross-sectional area extending between any two specified lev-

els (here, surface and 400-mb). Low-level moisture is assessed qualitatively by

examining the difference in temperature and dewpoint temperature within the low-

est 100-mb layer.

During DR, the troposphere is particularly warm and dry (PWTR = 13

mm), relative to other regimes (cf. Figs. 16 and 17–18). The lack of moisture at

low-levels results in a relative absence of mean MLCAPE (5 J kg^{-1}). As indicated

by the 500-mb composite, this dry air is associated with westerly winds on the

northside of an anticyclonic circulation centered southward of Arizona (Fig. 11).

At Phoenix, tropospheric flow is represented by a wind profile that veers from

southwesterly to westerly with height (Fig. 16).

In EMR, the troposphere is more moist compared to DR, where PWTR val-

ues are 25 mm and 13 mm, respectively (cf. Figs. 16 and 17). The increase in

low-level tropospheric moisture, relative to DR, indicates an environment with

NOTE TO USERS

Page(s) not included in the original manuscript and are
unavailable from the author or university. The manuscript
was scanned as received.

61

This reproduction is the best copy available.

UMI®
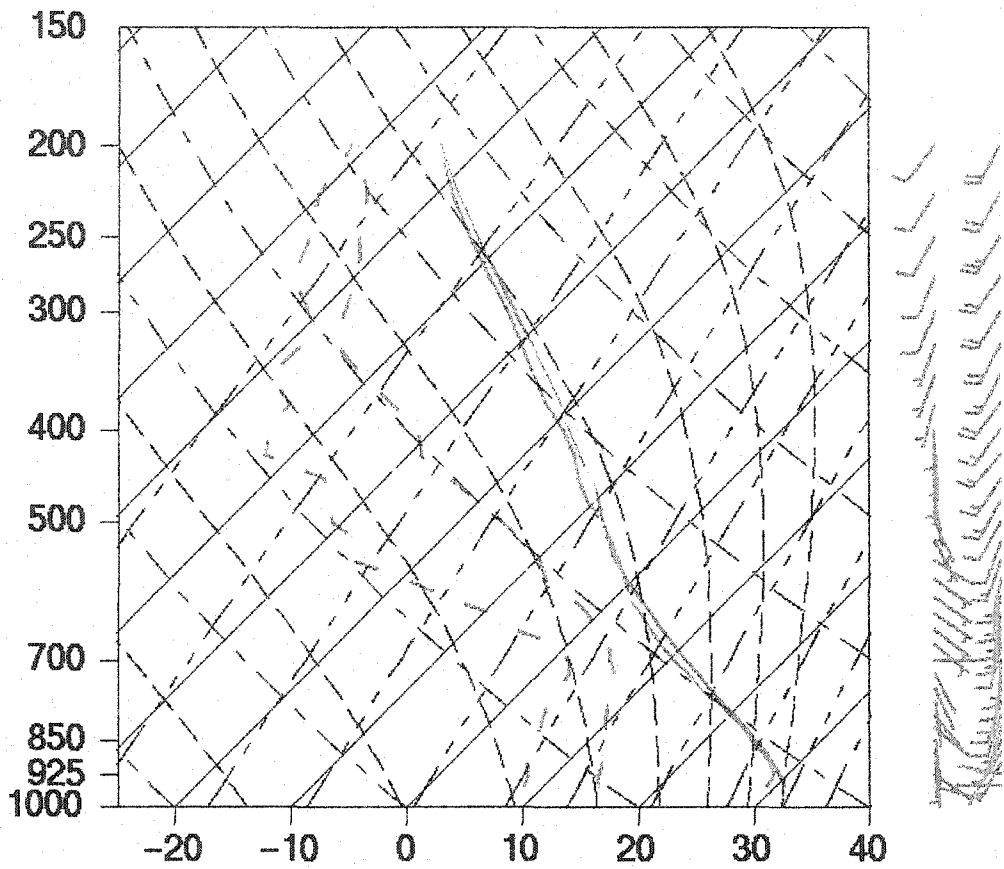
Figure 17. Composite 12 UTC sounding at Phoenix for eastern mountain regime (EMR : orange, N=10), central–eastern mountain regime (CEMR: yellow, N=31), and central–eastern and Sonoran regime (CEMSR: blue, N=17).

higher MLCAPE (5 J kg^{-1}vs. 94 J kg^{-1}, respectively) . At midlevels, increased

moisture corresponds with changes in the 500-mb flow, where the subtropical

high is shifted farther northward and eastward, compared to DR, resulting in a

resurgence of the meridional moist axis over western New Mexico (cf. Figs. 11

and 12). At Phoenix, the tropospheric flow is represented by a wind profile that is

nearly undirectional with height, with light south-southwesterly winds at low-levels,

and stronger south-southwesterly winds at mid–upper levels (Fig. 17).

During CEMR, tropospheric moisture is even higher than in EMR (30 mm

vs. 25 mm, respectively; Fig. 17), but is remarkably similar to CEMSR. Given the

similarity in CEMR's and CEMSR's thermodynamic characteristics, they are dis-

cussed together. The increase in low-level moisture found in CEMR and CEMSR,

relative to EMR, indicates an environment that contains higher values of mean

MLCAPE (484 J kg^{-1}during CEMR and 610 J kg^{-1} during CEMSR). Interestingly,

the 5 mm increase in mean precipitable water EMR to CEMR, is strikingly similar

to perturbations of precipitable water associated with the monsoon boundary (~6

mm; Adang and Gall 1998). Thus, the increase in moisture at midlevels reflects a

westward shift in the location of the monsoon boundary (cf. Figs. 12 and 13; cf.

Figs. 12 and 14).

Subtle differences in the orientation of the horizontal ridge axis between

CEMR and CEMSR result in different 850–500-mb wind profiles (Fig. 17). During

CEMR, the low–midlevel wind profile at Phoenix is characterized by light winds

that veer from easterly to westerly from the surface to 700 mb, and slightly stronger southerly winds within the 700–500-mb layer. In contrast, during CEMSR, the low–midlevel wind profile is characterized by light winds that back slightly from southeasterly to easterly from 925–500 mb (Fig. 17).

These results indicate that the 925–500 mb layer of easterlies found in the CEMSR sounding is more favorable for more organized storm development over elevated terrain and storm movement toward lower terrain than the southerlies associated with CEMR. Assuming that storm outflow evolves favorably for storm redevelopment (e.g., Weisman and Klemp 1986), interactions between outflows and the layer of easterlies within CEMSR's sounding may increase the lift available for new storm development. Smith and Gall (1989) also assert that midlevel easterlies (~700–400 mb) provide organized storm development over the Sonoran Desert, owing to ideal interactions (perpendicular) with the Southeast Highlands.

During NDR, composite sounding characteristics are found for each storm movement category: eastward-moving, northward-moving, and westward-moving (Fig. 18). Of the five regimes, NDR soundings contain the most tropospheric moisture, making them the most unstable set of soundings, given sufficient lift. The striking similarity in tropospheric moisture and lapse rate among the 3 NDR types gives credence to their common classification (Fig. 18). As expected, composite wind profiles show a strong relationship to storm movement, with south-

64

westerly tropospheric winds associated with eastward-moving storm days, southerly tropospheric winds associated with northward-moving storm days, and a layer of easterly to southeasterly winds (925–500 mb) associated with westward-moving storm days (Fig. 18). These results agree with the 500-mb composites discussed earlier (Fig. 15).

The 12 UTC composites discussed above give a physically-consistent picture of synoptic-scale conditions associated with each regime prior to its development. Although these results show that intraseasonal variability in storm development is related to the location of the North Pacific trough, subtropical high, and meridional moist axis, forecasters rely also on sounding variables (e.g., Moller 2001) to anticipate the weather. Thus, several sounding variables are investigated to determine their use in distinguishing among regimes.

4.2.2 Use of Sounding Variables: Box-and-Whisker Plots

Ninety-nine sounding variables are computed for each regime using National centers-Advanced Weather Interactive Processing System Skew-t Hodograph Analysis and Research Program (NSHARP) scripts provided by John Hart of the Storm Prediction Center. Like the composite soundings discussed previously, these variables are computed from 12 UTC soundings at Phoenix. Distinguishing characterstics of these soundings are investigated by examining box-and-whisker plots of each variable by regime type. Box-and-whisker plots show the distribution of data, for each regime, within 1.5 times the interquartile range,
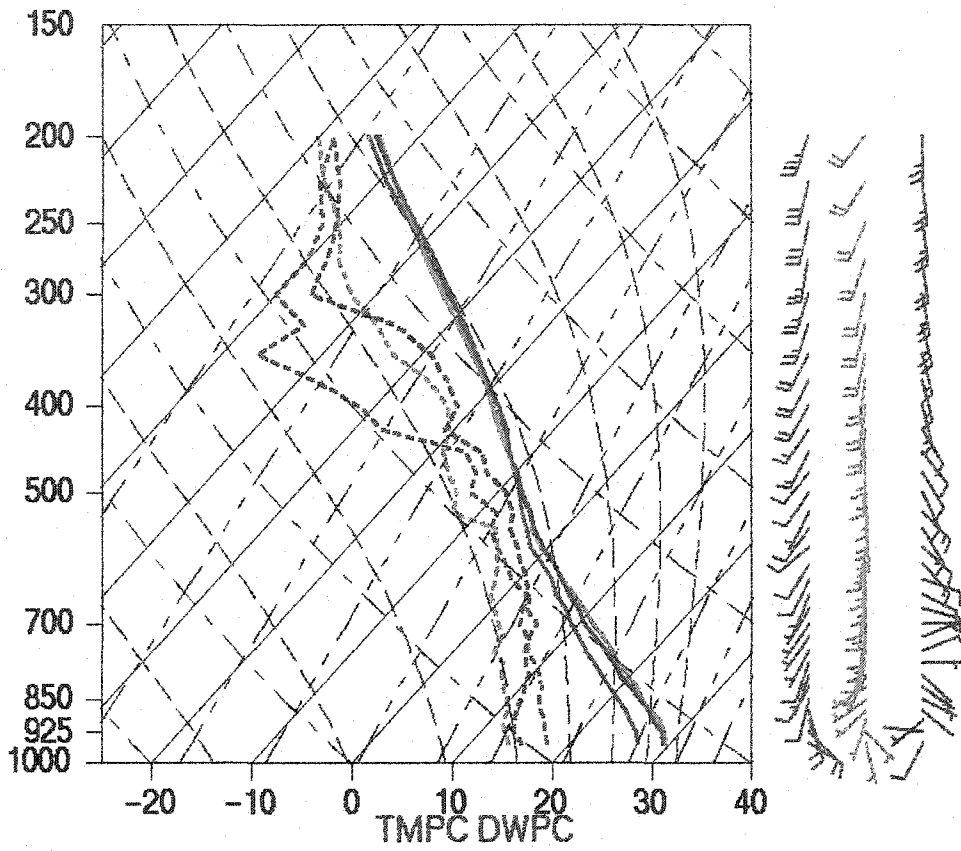
Figure 18. Composite 12 UTC soundings at Phoenix for nondiurnal regime (NDR), where storms may move eastward (red, N=7), northward (green, N=8), and westward (blue, N=4).

with values outside that range considered outliers. Highlights from this analysis are discussed below.

A subjective examination of 99 box-and-whisker plots of NSHARP variables reveals that the three most discriminating variables include precipitable water (surface–400 mb), surface–6- km shear, and density-weighted 700–400-mb mean wind. The importance of precipitable water as a discriminating variable is apparent from the drastically different distributions found between DR and EMR, and between DR and EMR and other regimes (Fig. 19). These substantial differences in precipitable water reflect the tendency for median precipitable water values to increase with increasing storm coverage (Fig. 19). However, as storm coverage increases, distributions of precipitable water also become less distinctive, making tropospheric moisture a relatively poor distriminating variable among CEMR, CEMSR, and NDR. As shown in Section 4.1, these differences in precipitable water are related to the location of the meridional moist axis during each regime.

The importance of surface–6-km shear as a discriminating variable is revealed by significantly different distributions between CEMSR and three other regimes: DR, EMR, and NDR (Fig. 20). Differences in shear between CEMSR and NDR reflect the tendency for median shear values to increase when synoptic-scale forcing is present (Fig. 20). In contrast, differences in shear between CEMSR and the two drier regimes (DR and EMR) reflect the tendency for median
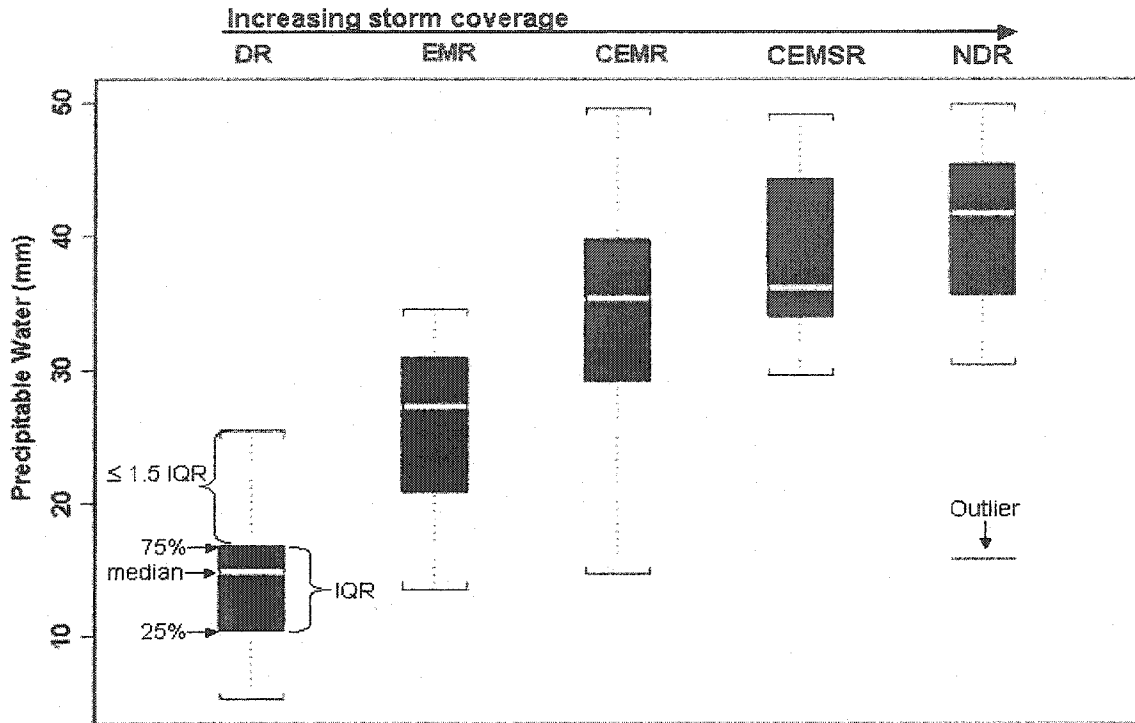
Figure 19. Box and whisker plot of precipitable water (surface–400 mb; mm), calculated from 12 UTC soundings at Phoenix. Filled boxes show the data distribution within the 25th and 75th percentiles, where the median is denoted by a thick white line. Outermost braces indicate values within 1.5 x interquartile range (IQR, defined as the difference between the 75th and 25th percentiles), whereas isolated horizontal lines indicate outliers.
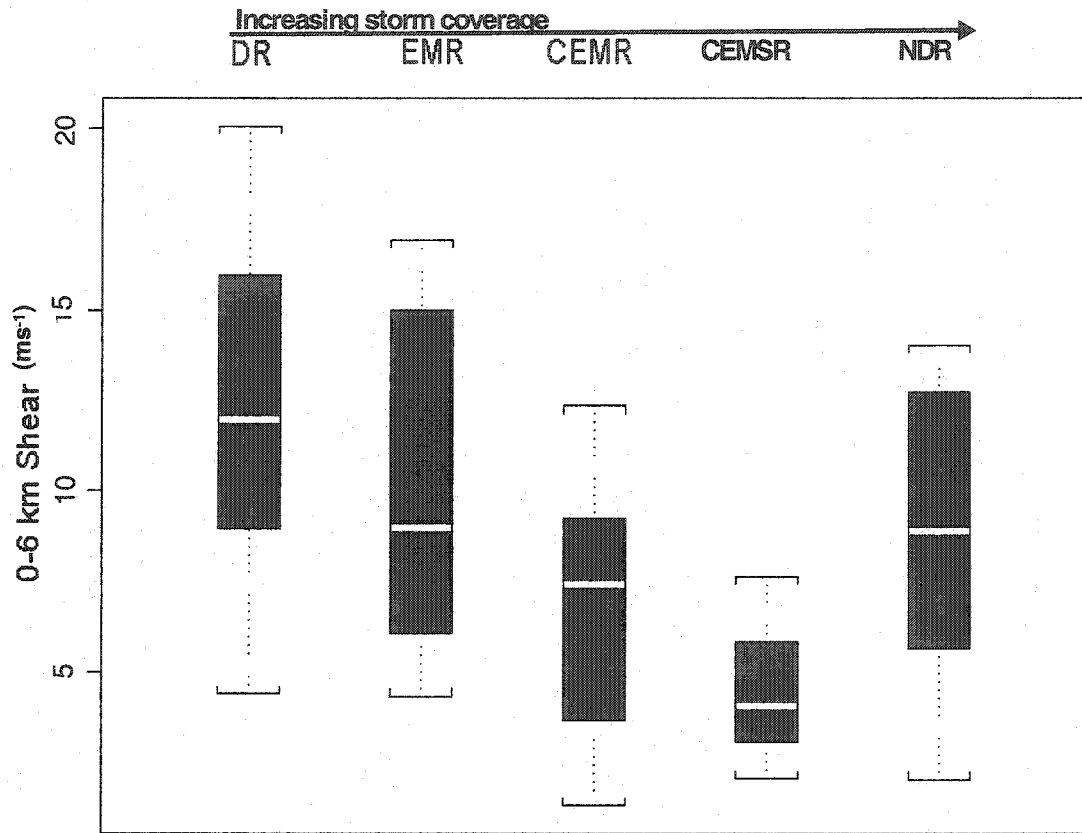
Figure 20. Same as in Fig. 19, only for surface–6-km shear.

shear values to decrease with increasing storm coverage (Fig. 20). Why might this relationship arise? One possible answer to this question is tied to the thermal forcing of deep moist convection. The low shear of 12 UTC Phoenix soundings reflect an wind profile where winds remain light with increasing height. Thus, assuming that such light winds occur over elevated terrain also, the lack strong wind allows thermally forced circulations to moisten the environment and lift parcels to their LFC, without much mixing near the surface (e.g., Banta 1990). Since these regions of enhanced moisture are surrounded by drier air, stronger storms (updrafts), and, in turn, stronger outflows may be produced, relative to an environment with strong wind at mountain-level and high shear at Phoenix (owing to increasing wind speed with height; e.g., Banta 1990). These outflows and may move toward lower terrain and cause more productive storm redevelopment over lower elevations, compared to storms that develop under higher shear conditions.

Density-weighted 700–400-mb mean wind direction distinguishes well between DR and the other regimes (Fig. 21). Indeed, wind direction above 220° (25th percentile of DR) is almost always associated with a lack of precipitation across the domain. Along these lines, there is a tendency for storm coverage to increase as the median wind becomes more easterly, excluding NDR (Fig. 21). These differences in flow are related to the orientation of the ridge axis and the location of the center of the anticyclone, relative to Arizona and the North Pacific trough (cf. Figs. 11–14). Interestingly, as storm coverage increases, so does the variability in wind direction (Fig. 21). The increased variability in wind direction
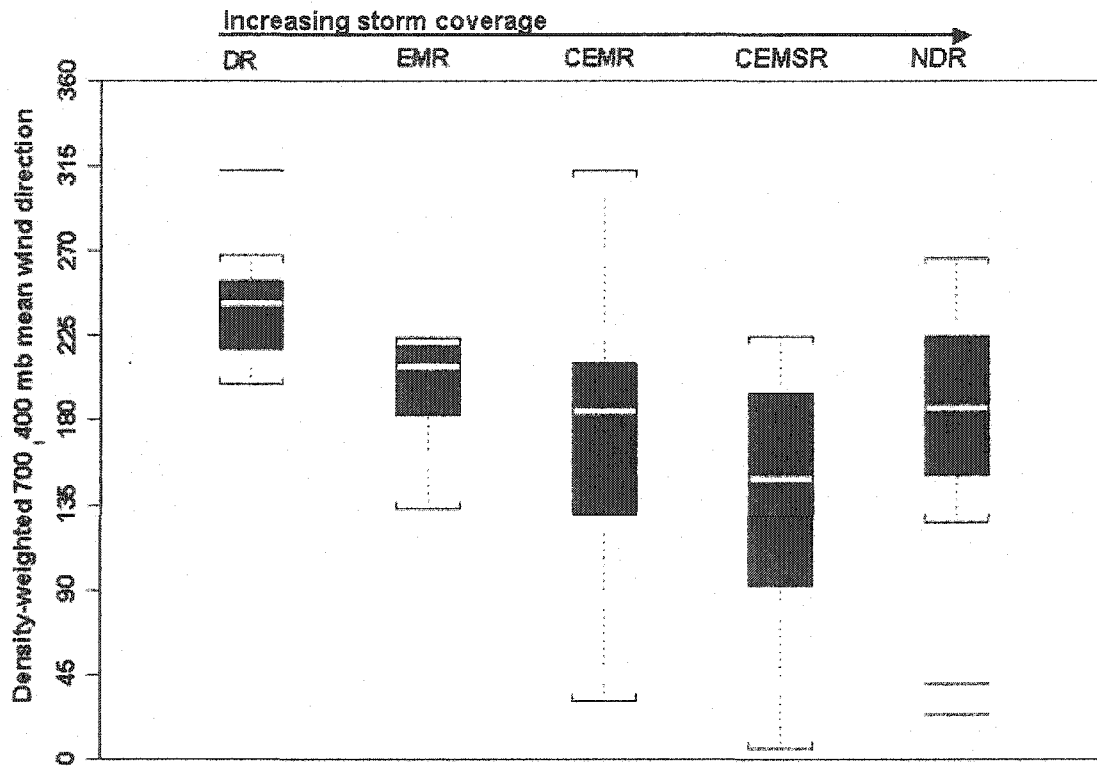
Figure 21. Same as in Fig. 19, only for density-weighted mean 700–400-mb wind direction (°).

during CEMR and CEMSR, compared to EMR and DR, likely represents higher variability in synoptic-scale pattern. Since the subtropical high determines mid–upper-level wind direction during CEMR and CEMSR (Figs. 13 and 14), this variability in wind direction likely represents the meandering nature of anticyclonic centers during the NAM.

Given the dissimilarity in precipitable water and/or 0–6 km shear distributions among various regimes, these variables may help forecasters anticipate which regime(s) is (are) most likely on a given day. Toward this end, the strength of such relationships is clarified further by applying discriminant analysis to these variables.

4.2.3 Discriminant Analysis

The goal of discriminant analysis is to classify a new event correctly based on its observed characteristics (Wilks 1995, 408). Herein, the discriminant analysis technique is described briefly, with the complete methodology demonstrated in Appendix B, based on Wilks (1995, 408–415). In this study, discrimination among events arises from a "training sample" that is used to build a linear relationship between two regimes (Wilks 1995, 409–415). This training sample consists of precipitable water and surface–6-km shear values from 12 UTC Phoenix soundings associated with each regime. These data are denoted by n_1 x K- and n_2 x K-dimensional vectors x_1 and x_2, respectively, where n_1 and n_2 denote the number

of soundings in each regime (89 in total), and $K=2$. These vectors are used to find

the discriminant vector, d_1, defined as "... a direction... in the K-dimensional

space of the data, such that the distance between the two mean vectors (mean

vectors are defined in Appendix B) is maximized when the data are projected onto

d_1" (Wilks 1995, 410). The discriminant vector is given by

$$d_1 = [S_{pooled}]^{-1}(\overline{x_1} - \overline{x_2}), \tag{5}$$

where

$$[S_{pooled}] = \frac{(n_1 - 1)[S_1] + (n_2 - 1)[S_2]}{(n_1 + n_2 - 2)} \tag{6}$$

is a pooled estimate of the dispersion of the data around their means, $[S_1]$ and

$[S_2]$ are sample covariance matrices computed from K-dimensional vectors

x_1 and x_2, and the overbar represents the mean. Once the discriminant vector is

obtained, the midpoint is calculated between the means of the two groups,

$$\overline{\delta}_1 = d_1^T \frac{\overline{x_1} + \overline{x_2}}{2} \tag{7}$$

where superscript T denotes the transpose of d_1. Since this midpoint lies on d_1,

a line emanating from this point and drawn perpendicular to this vector divides the

samples into two groups. If x_1 and x_2 lie on opposite sides of this line, they are

discriminated perfectly. In the future, d_1 and $\overline{\delta}_1$ may be used to classify a future

observation, y, as belonging to either group one or group two, following the rule

base given in Wilks (1995, 410):

$$\text{Assign } \mathbf{y} \text{ to group one if } d_1^T \bar{\mathbf{y}} - \bar{\delta}_1 \geq 0$$

or

$$\text{Assign } \mathbf{y} \text{ to group two if } d_1^T \bar{\mathbf{y}} - \bar{\delta}_1 \leq 0.$$

Thus, good discrimination affords a forecast tool which can help forecast-

ers distinguish anticipated outcomes. Also, assuming the two most distinguishing

variables are used, the "goodness" of the discrimination is a measure of forecast

difficulty. A 2x2 contingency table is used to quantify the accuracy and skill of

these simple forecast models (Table 2). Within the contingency table, a is a "hit",

b is a "false alarm", c is a "miss", and d is a "correct null" (Table 2). For each pair

of regimes, two forecast situations may be investigated (e.g., DR vs. EMR and

EMR vs. DR), resulting in two sets of scores. This complexity is avoided by com-

puting scores independent of the forecast situation only, including the hit rate,

$$H = \frac{a+d}{n}, \text{ miss rate, } M = \frac{b+c}{n}, \text{ and Heidke skill score,}$$

$$HSS = \frac{2(ad - bc)}{(a+c)(c+d) + (a+b)(b+d)}, \text{ where } n \text{ is the total number of fore-}$$

casts or observations (Wilks 1995, 238–244). The hit rate and miss rate are given

as percentages to reveal the probability of a correct or incorrect forecast. The

HSS measures the skill of the model relative to a random forecast, such that a

value of 0 indicates no skill compared to a random forecast, and a value of 1 indi-

74

cates the best skill compared to a random forecast. With these measures in mind, results of the discriminant analysis are discussed next.

Table 2: Example of a 2x2 contingency table, where *a* is a hit, *b* is a false alarm, *c* is a miss, and *d* is a correct null.

	Regime Observed	Regime Not Observed
Regime Forecast	*a*	*b*
Regime not Forecast	*c*	*d*

,

The ability of precipitable water to distinguish between various regimes is demonstrated best by a discriminant analysis of DR vs. wet (EMR+CEMR+CEMSR+NDR) regimes (Fig. 22). Within these groups, the assumption that variance is the same is violated, but not at a degree that depricates results significantly. Thus, discriminant analysis shows that precipitable water distinguishes DR from wet regimes quite well—only 3 of the wet regimes are classified incorrectly as dry days (Fig. 22). Accordingly, this simple forecast model has a hit rate, miss rate, and Heidke skill score (HSS) of 93%, 7%, and 0.87, respectively. However, as storm coverage increases (e.g., CEMR, CEMSR, NDR), the 0–6 km shear discriminates regime type better than precipitable water, resulting in a dividing line that is more horizontally oriented (Fig. 23). This shift in discrimination from precipitable water to 0–6 km shear, as storm coverage increases, corresponds well with box-and-whisker plots presented in Section 4.2.2. The 0–6 km shear distinguishes best between CEMSR and NDR (Fig. 23), producing a hit rate, miss rate, and HSS of 69%, 31%, and 0.39, respectively.

The lower value of NDR vs. CEMSR accuracy scores compared to dry vs. wet regimes, represents the greater difficulty in forecasting regime type during wetter periods of the NAM.

A more complete forecast model is constructed by combining the results of each discriminant analysis. Toward this end, the dividing lines resulting from discriminant analyses between: the DR and wet regimes, EMR and CEMR, CEMR and CEMSR, CEMSR and NDR, and CEMR vs. NDR, are drawn within the 2-D space (Fig. 24). Then, color-coded arrows are drawn to define regions within the 2-D space defining each regime (Fig. 24). The ensueing forecast model shows that precipitable water discriminates well between the break regimes (DR and EMR) and burst regimes (CEMR, CEMSR, and NDR; Fig. 24). On the other hand, the surface–6-km shear discriminates best between CEMR and NDR, and CEMSR and NDR (Fig. 23). Both precipitable water and surface–6-km shear help discriminate between CEMR and CEMSR (Fig. 24). Thus, discrimination among regimes generally declines with increasing storm coverage. This decline in discrimination affects overall forecast accuracy, such that regimes are identified correctly 55% of the time. This 55% forecast accuracy is a promising result, because the discriminant analysis model outperforms forecasts based on persistence or a simple one in five guess.

Since the forecast model contains a hierarchy of forecast accuracies, this statistic conceals the higher forecast accuracy attainable from some forecast situ-
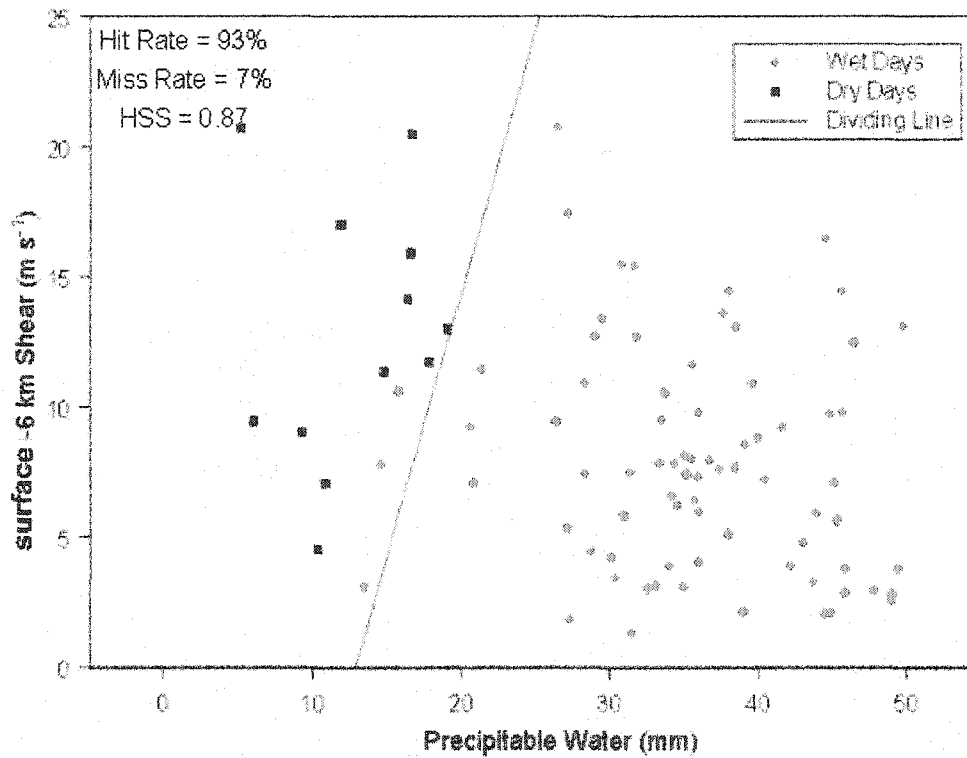
Figure 22. Discriminant analysis surface–6-km shear and precipitable water for dry and wet days during 1997 and 1999 NAMs. Wet days include the EMR, CEMR, and NDR regimes. Squares indicate dry days, whereas circles indicate wet days. The dividing line shows the separation of groups from the discriminant analysis.

77
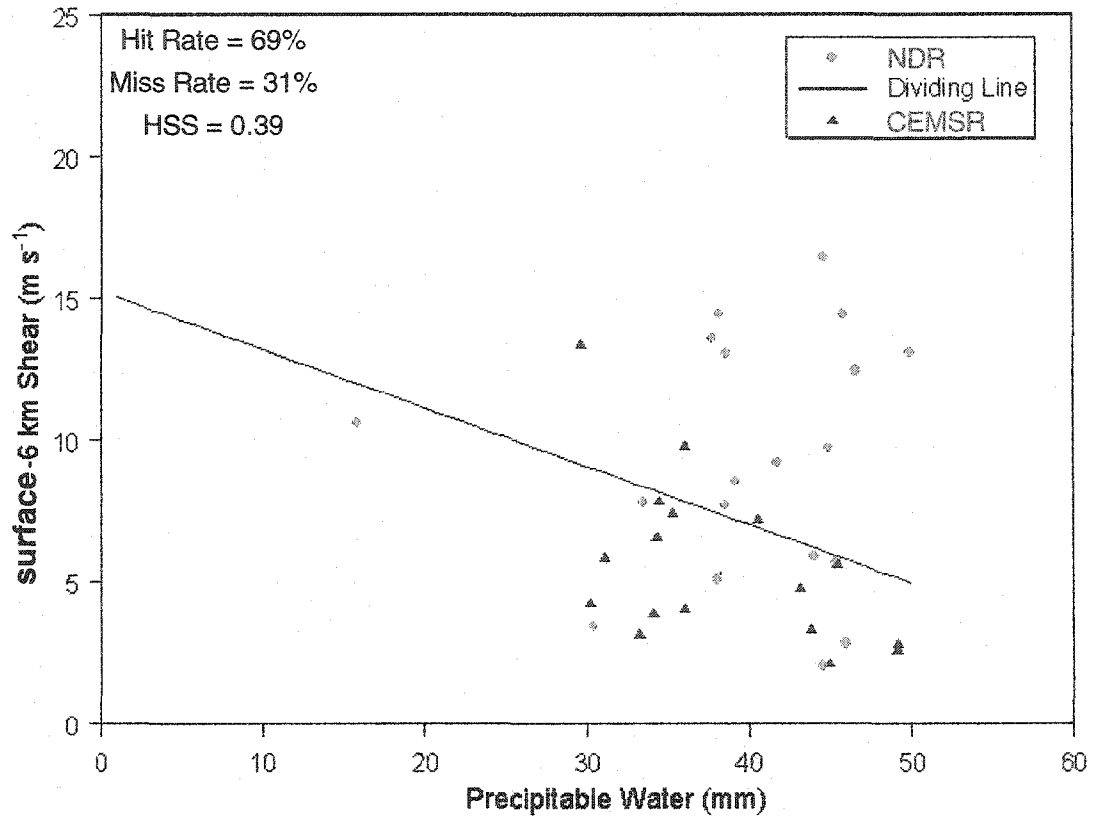
Figure. 23. Discriminant analysis of surface–6-km shear and precipitable water for CEMSR (triangles) and NDR (circles) during 1997 and 1999 NAMs. The dividing line shows the separation of groups from the discriminant analysis.
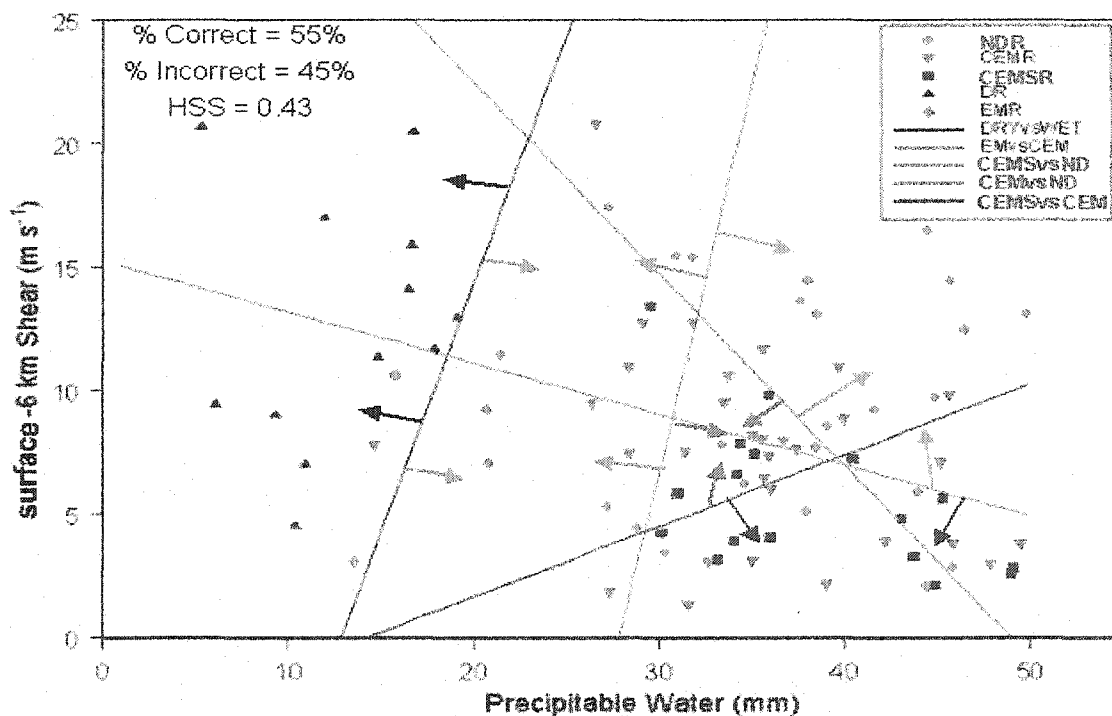
Figure 24. Combined discriminant analyses of surface–6-km shear and precipitable water. Colored lines represent the dividing line between regimes, where discriminant analyses include: black: DR vs. all other regimes, orange: EMR vs. CEMSR+CEMSR+NDR, green: CEMSR vs. NDR, blue: CEMR vs. NDR, and pink: CEMR and CEMSR. Each regime is denoted by a symbol, where DR is a black triangle, EMR is an orange diamond, CEMR is a blue "delta", CEMSR is a pink square, and NDR is a light green circle. Colored arrows indicate region where each regime is classified by this analysis.

ations. However, the model illustrates well the relative difficulty of various forecast situations, where discerning: 1) DR or EMR is an easy forecast, 2) NDR vs. CEMR or CEMSR is a more difficult forecast, and 3) CEMR vs. CEMSR is the most difficult forecast (Fig. 24). The relative lack of discrimination between CEMR and CEMSR highlights the difficulty forecasters face as they decide whether storm development will remain over elevated terrain or move into the Sonoran Desert during the evening.

In summary, intraseasonal variability during the 1997 and 1999 NAM seasons is described by five regimes. The occurrence of these regimes is related to the location and evolution of the North Pacific trough, subtropical high, and meridional moist axis, which, in turn, determine the magnitude of precipitable water and surface–6-km shear at Phoenix. Although these results provide forecasters with tools to help forecast each regime, this basic forecast model may be improved by investigating how storm development, synoptic-scale flow, and Phoenix soundings evolve on a daily basis. The next section addresses these topics by examining the persistence of regimes and situations that produce significant changes in regime type.

NOTE TO USERS

Page(s) not included in the original manuscript and are
unavailable from the author or university. The manuscript
was scanned as received.

81 & 82

This reproduction is the best copy available.

UMI®

Chapter 5. Evolution of Regimes

Differences in the diurnal evolution of the five regimes (Chapter 3) and related analyses of 12 UTC synoptic-scale patterns and sounding characteristics (Chapter 4) illustrate spatial aspects of intraseasonal variability in the NAM over Arizona. Chapter 5 investigates temporal aspects of intraseasonal variability by examining the daily evolution of regimes and precipitable water. The strong relation between precipitable water and regime type make this variable an ideal choice for this investigation.

5.1 Time series of regimes

Intraseasonal variability is characterized by periods of relatively large and small areal storm coverage, similar to bursts and breaks (Fig. 25). During bursts, three regimes occur, including CEMR, CEMSR, and NDR (upward-pointing lines in Fig. 25). In contrast, only two regimes occur during breaks, including EMR and DR (downward-pointing lines in Fig. 25). A comparison of regime evolution during bursts and breaks reveals more intraseasonal variability during wet periods than dry periods (Fig. 25). Although this result may be biased by the small number of dry periods in 1997 and 1999, some regimes are clearly more persistent than others.

Differences between the evolution of regimes in 1997 and 1999 suggest something about interseasonal variability, of which a complete analysis is beyond

the scope of this thesis. Therefore, such differences are described briefly. For example, the onset of the NAM begins almost two weeks later in 1997 than 1999 (cf. Figs. 25a, b). Following the onset of the NAM, breaks interupt bursts more frequently in July 1997 than July 1999, but less frequently in August 1997 than August 1999 (cf. Figs. 25a, b). In addition, during August 1999, breaks are drier and longer-lived compared to 1997 (cf. Figs. 25a, b). These contrasts in the evolution of bursts and breaks exemplify aspects of interseasonal variability between NAM seasons.

Intraseasonal variability is investigated by examining the persistence or predictability of regime evolution during the NAM. The persistence of regimes is determined by calculating relative frequencies of regime occurrence one day prior to, and one day following, each regime. This investigation reveals that DR is the most persistent, recurring 82% of the time during July and August 1997 and 1999 (cf. Figs. 25a and 25b). Since half of DR days occur prior to monsoon onset (Fig. 25), the persistence of this regime is calculated also before and after monsoon onset. Before monsoon onset, DR persists 83% of the time (5 of 6 events), whereas after monsoon onset, DR persists 66% of the time (4 of 6 events). Thus, even after monsoon onset, DR remains the most persistent regime. Transitions toward DR result in either persistent or dramatically reduced storm coverage, whereas transitions from DR result in either persistent or dramatically increased storm coverage (Fig. 26). Given the extreme persistence of DR, such dramatic changes in storm coverage have the potential to startle forecasters and populace.

84
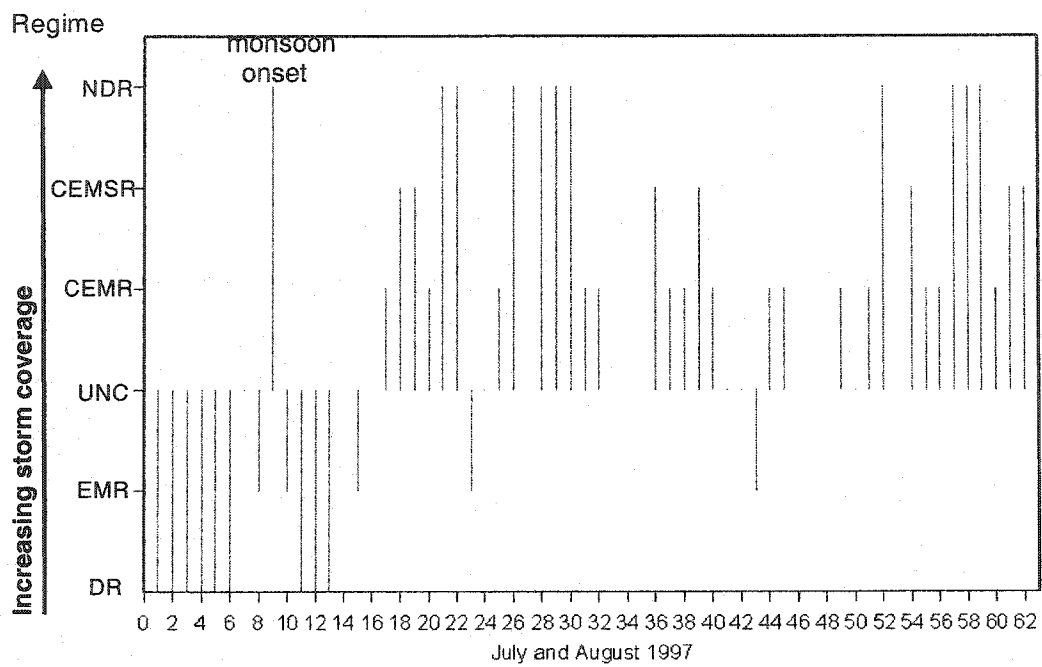
Figure 25a. Time series of regimes during July and August 1997, where DR is the dry regime, EMR is the eastern mountain regime, UNC is unclassified (denoted by a dot), CEMR is the central-eastern mountain regime, CEMSR is the central-eastern mountain and Sonoran regime, and NDR is the nondiunral regime. Missing dates are blank.
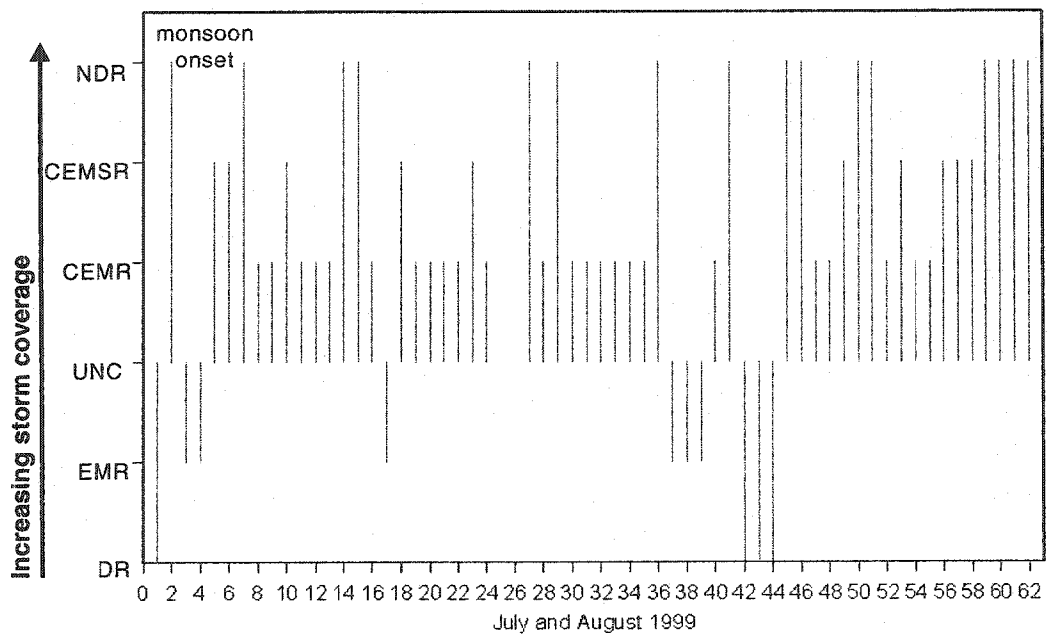
Figure 25b. Same as in Fig. 25a, only for July and August 1999.
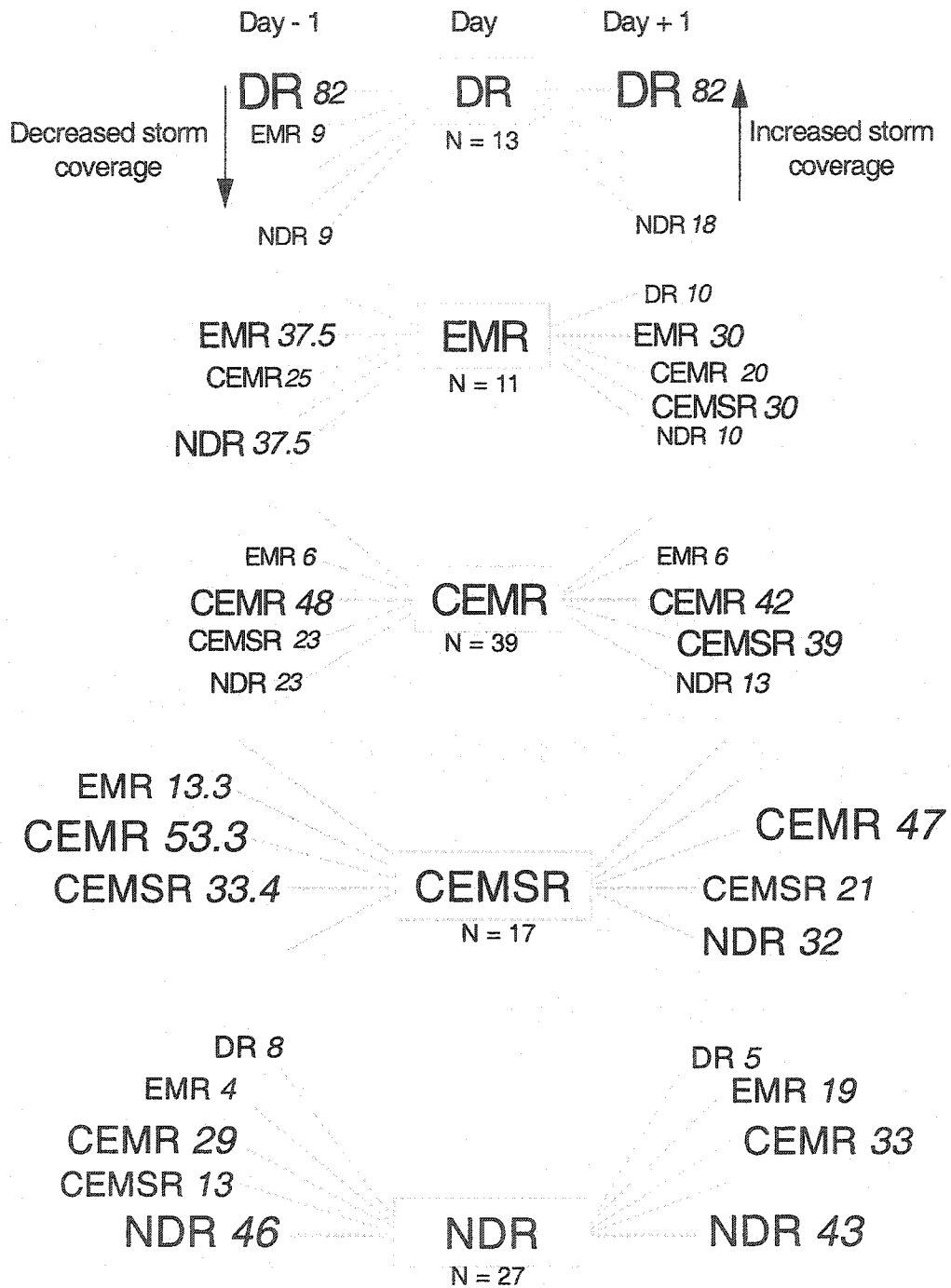
Figure 26. The relative frequency of regimes preceding and following DR, EMR, CEMR, CEMSR, and NDR.

Thus, an improved understanding of atmospheric processes leading to such abrupt transitions in weather is pursued further in section 5.2.

Transitions toward EMR produce either persistent or reduced storm coverage (Fig. 26). Based on results from Chapter 3, this reduction in storm coverage is likely tied to an eastward shift in the North Pacific trough, subtropical high, and-meridional moist axis (e.g., cf. Figs. 15 and 12). On the other hand, transitions from EMR produce either persistent or increased storm coverage (Fig. 26), and are likely tied to a westward shift in the same features (e.g., cf. Figs. 12 and 14).

Similar to EMR, transitions to CEMR usually result in mostly persistent or reduced storm coverage, and shifts from CEMR result in mostly persistent or increased storm coverage (Fig. 26). The higher persistence of CEMR, compared to EMR, indicates the more transient nature of EMR and its associated synoptic-scale environment. Since CEMR occurs most often, the synoptic-scale pattern favored during the NAM is probably similar to that shown in Fig. 13, where the North Pacific trough is located off-shore, the meridional moist axis is centered over the Arizona–New Mexico border, and the flow is modulated by the location of the subtropical high. Deviations from this pattern result in subtle environmental differences (cf. Figs. 13 and 14), which sometimes favor CEMSR rather than CEMR (Fig. 26). This similarity in synoptic-scale environment, combined with the nearly equal chance of CEMR and CEMSR following CEMR, make discerning the potential for either regime challenging.

Transitions toward CEMSR produce either persistent or increased storm coverage, whereas transitions from CEMSR produce either reduced or increased storm coverage (Fig. 26). Given the similarity in moisture and instability found prior to CEMSR and CEMR (Chapter 4), it follows that the nonpersistence of CEMSR is likely due to the lack of persistent lifting mechanisms over lower elevations. Nonetheless, since CEMR follows CEMSR about half of the time, forecast statistics may be improved by predicting CEMR, rather than CEMSR or NDR, when shortwave troughs (Chapter 4) are absent from the 500-mb flow.

Similar to CEMSR, shifts toward NDR result in either persistent or increased storm coverage (Fig. 26). Unlike CEMSR, shifts from NDR result in either very persistent or significantly reduced storm coverage (note the absence of CEMSR in Fig. 26). The persistent nature of NDR likely reflects the time scale of synoptic-scale forcing often present during this regime (Chapter 4). On the other hand, the next-day occurrence of CEMR, EMR, or DR probably reflects an eastward shift in the location of the subtropical high and meridional moist axis (e.g., cf. Figs. 15a and 12), following the passage of a shortwave trough in the westerlies.

Although this investigation of intraseasonal variability shows that day-to-day transitions in regime can often result in little or no change in storm coverage, occasionally changes in regime produce significant changes in storm coverage.

The relatively rare occurrence of significant changes in storm coverage make an awareness and understanding of synoptic-scale processes responsible for such changes important to forecasters. Since Chapter 4 shows that precipitable water discriminates between regimes having vastly different storm development patterns, significant changes in regime are likely tied to changes in precipitable water. This association is examined further below, followed by an investigation of synoptic-scale processes responsible for these abrupt changes in environment.

5.2 Relation between changes in regime and precipitable water

The relationship between changes in regime and precipitable water is investigated by comparing daily changes in regime to 24-h differences in precipitable water (surface–400 mb). These differences are computed using consecutive 12 UTC soundings at Phoenix during the 1999 NAM season. This analysis focuses on the 1999 NAM owing to the relatively large number of consecutive days missing radar data, and hence regime types, in 1997. Significant changes in precipitable water are defined as those differences either higher than the 80th percentile (6.1 mm) or lower than the 20th percentile (-5.3 mm; Fig. 27). Based on these criteria, 11 days are characterized by a significant increase in precipitable water, whereas 10 days are characterized by a significant decrease in precipitable water (Fig. 27). But, how often do these significant changes in tropospheric moisture relate to changes in regime (i.e., storm coverage)?
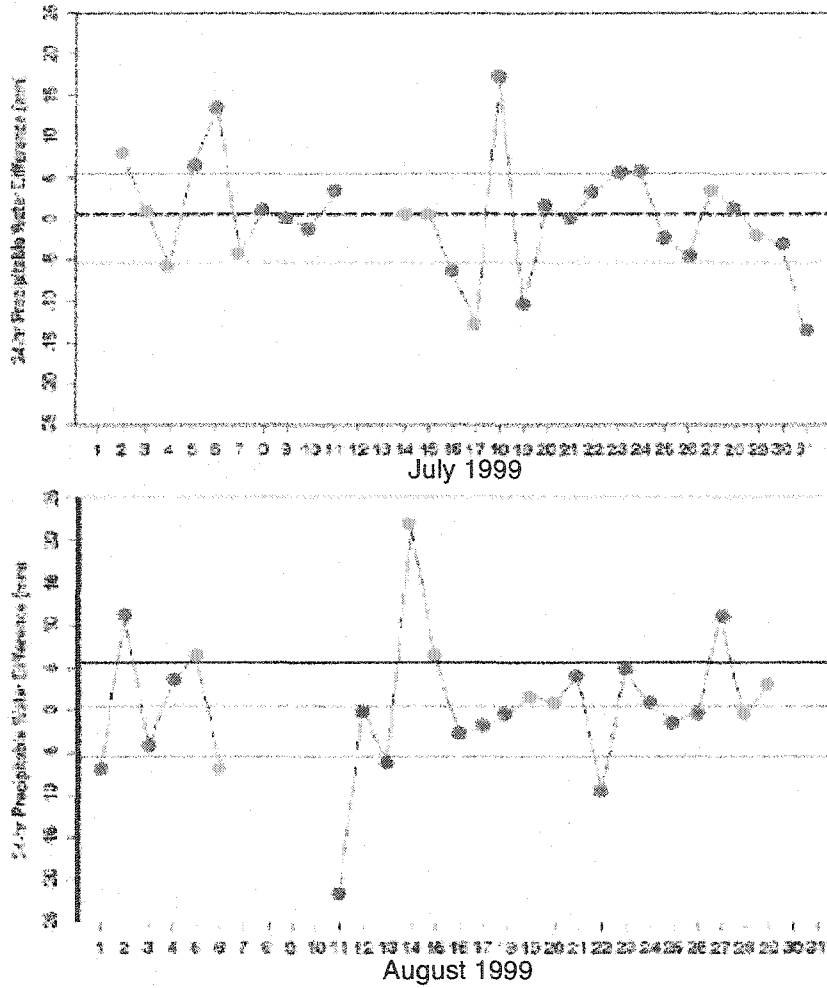
Figure 27. Time series of precipitable water (mm) and regimes during July and August 1999, where brown denotes the dry regime (DR), orange denotes the eastern mountain regime (EMR), pink denotes the central–eastern mountain regime, blue denotes the central-eastern mountain and Sonoran regime (CEMSR), and green denotes the nondiurnal regime (NDR).

A comparison of changes in precipitable water and regime (Fig. 27) reveals that the eleven substantial increases in precipitable water are associated with either regimes having larger areal storm coverage (6 events or 54%) or no change in regime (5 events or 46%). Further analysis of these time series shows that 4 of 5 regimes (80%) that *persist* following *increases* in tropospheric moisture occur during bursts. Since most of these persistent events produce precipitation in the Sonoran Desert, observed increases in precipitable water likely result from this rainfall. Thus, significant increases in moisture preceded by dry condition across the Sonoran Desert indicate a strong potential for increased storm coverage. On the other hand, the ten substantial decreases in precipitable water (Fig. 27) are associated with smaller areal storm coverage (50%), no change in regime (40%), or larger areal storm coverage (10%; Fig. 27). Further analysis shows that 3 of 4 regimes (75%) that *persist* following *decreases* in tropospheric moisture occur during breaks. This result reflects the persistent nature of DR.

Therefore, changes in precipitable water of greatest interest to forecasters are those which produce an environment hostile to the sustenance of the previous day's regime. To help forecasters recognize these situations better, the next sub-section investigates synoptic-scale processes contributing to such significant changes in environment.

5.3 Diagnosis of changes in precipitable water

92

The role of synoptic-scale processes in significant changes in precipitable water (upper and lower 20th percentile) is investigated using two complementary analyses. First, a simplified moisture time tendency is computed using 6-h Rapid Update Cycle-2 (RUC-2; Benjamin et al. 1998) analyses of geopotential height and mixing ratio. Second, 6-h RUC-2 analyses are analyzed to find changes in synoptic-scale pattern related to significant increases and decreases in tropospheric moisture. Prior to computation of the moisture budget, 12 UTC Phoenix soundings and 6-h RUC analyses are used to find the level and 12-h period of maximum moistening or drying, respectively. At the middle of each 12-h period, terms in the mixing ratio tendency equation are calculated within a 100-mb layer, centered at the level of maximum change in mixing ratio, and then multiplied by $\partial t = 12$ h to explicitly show the advective processes responsible for local changes in moisture:

$$\delta q = \left(-\vec{V}_h \cdot \nabla q - \omega \frac{\partial q}{\partial p} \right) \delta t, \tag{8}$$

where q is mixing ratio, $\vec{V}_h$ represents the horizontal wind, ω is vertical motion in pressure coordinates, and p is pressure. This moisture tendency equation cannot address source and sink terms (Evaporation-Precipitation), turbulent mixing, or effects of parameterized convection. Thus, local changes in mixing ratio in this study result from the horizontal and vertical advection of moisture only.

93

To compare computed values of local mixing ratio tendency to actual changes, I compute the 12-h difference: $\delta q = q_{12} - q_o$. Similar values are not expected because computations of quasihorizontal and vertical advection assume that quasihorizontal and vertical advection persist over 12 h, when, in reality, they may occur over a shorter period.

Computations from (8) reveal that changes in moisture arise mostly from the horizontal advection of air from different source regions rather than from the vertical movement of moisture within the column (not shown). An exception is 17–18 July 1999, where local increases in moisture are enhanced by lift from a shortwave trough. Complementary analyses of synoptic-scale evolution show that, in general, increases in precipitable water of 6.1 mm or higher arises from the westward- (50%) or northward- (50%) development of the subtropical high, whereas decreases in precipitable water of -5.3 or more arises from the passage of a shortwave trough (90%) or evolving anticyclonic flow (10%). The magnitude of these changes in moisture (5–6 mm) correspond well with perturbations in precipitable water associated with the monsoon boundary (~ 6 mm; Adang and Gall).

Three representative cases are used to illustrate the importance of horizontal and verticial advection during periods of tropospheric drying and moistening for the synoptic-scale evolutions most prevalent during the NAM: 1) westward development of the subtropical high, 2) northward development of the subtropical high, and 3) passage of a shortwave trough in the westerlies.

5.3.1 Westward development of the subtropical high

During 4–5 July 1999, significant 24-h moistening in the 12 UTC sounding at Phoenix and a shift in midlevel winds from westerly to easterly (Fig. 28) accompany a transition in regime from EMR to CEMSR (Fig. 25a). Although mixing ratio increases throughout most of the column, the maximum increase in moisture occurs near 500 mb (Fig. 28). This increase in midlevel moisture is illustrated by water vapor imagery (Fig. 28) taken by the 6.7μ m channel of the Geostationary Operational Environmental Satellite-10 (*GOES-10*).

Maximum change in 500-mb mixing ratio occurs between 00 UTC and 12 UTC 5 July 1999. At 00 UTC 5 July 1999, Fig. 29a shows a light westerly wind over north-central Arizona, which increases in intensity northward owing to a relatively strong pressure gradient over the western United States. Light easterlies compose the flow south of central Arizona (Fig. 29a), with the subtropical anticyclone centered east of Texas (not shown). High mixing ratio values are located east of Arizona, with highest values over western New Mexico (Fig. 29a).During the next 12-h, high mixing ratio values are advected westward by easterly flow that evolves owing to the development of anticyclonic flow over the Four Corners (Figs. 29b,c).
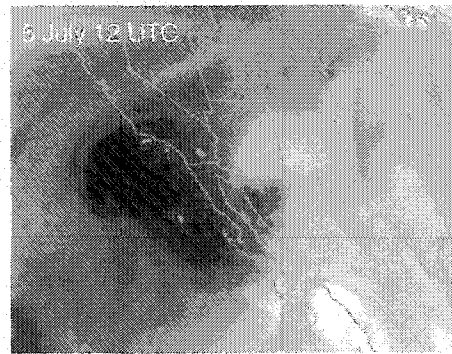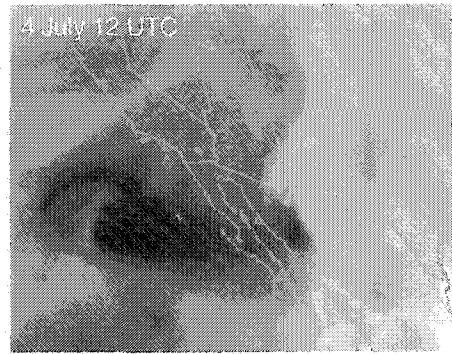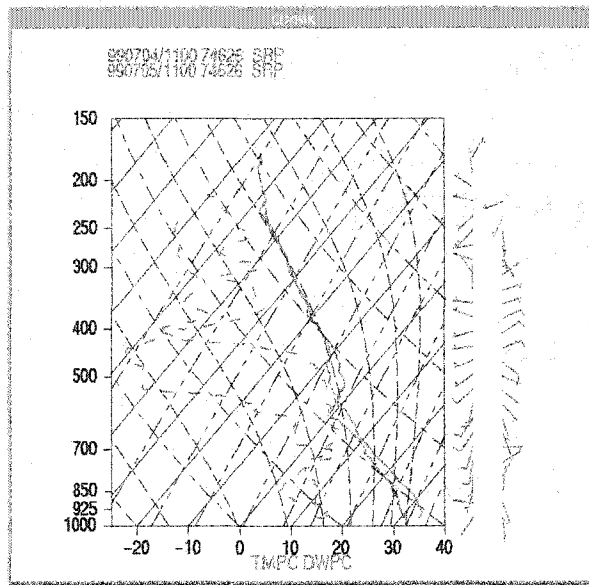
Figure 28. 12 UTC Phoenix soundings and GOES-10 water vapor imagery on 4 and 5 July 1999.
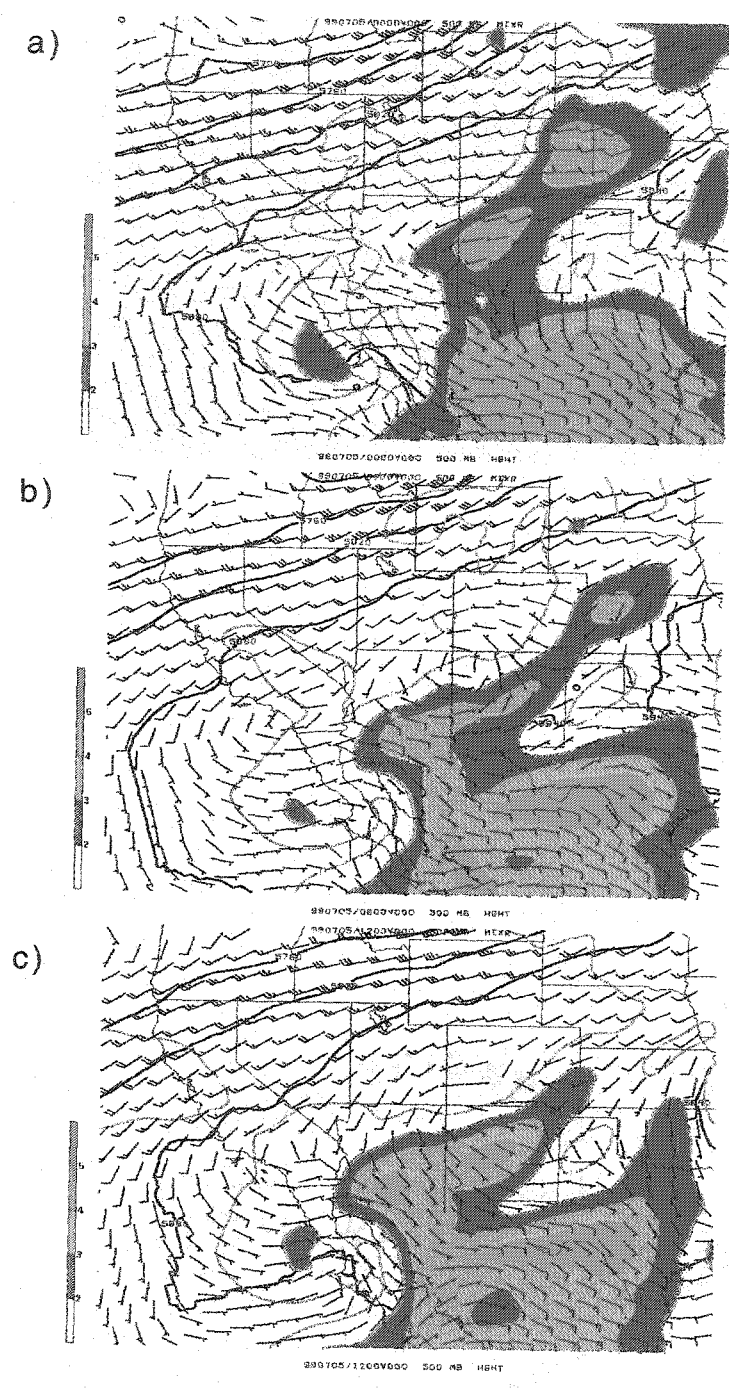
Figure 29. Map of 500-mb goepotential height (m), wind barbs (m s^{-1}), and mixing ratio (g kg^{-1}) for a) 00 UTC 5 July 1999, b) 06 UTC 5 July 1999, and c) 12 UTC 5 July 1999.
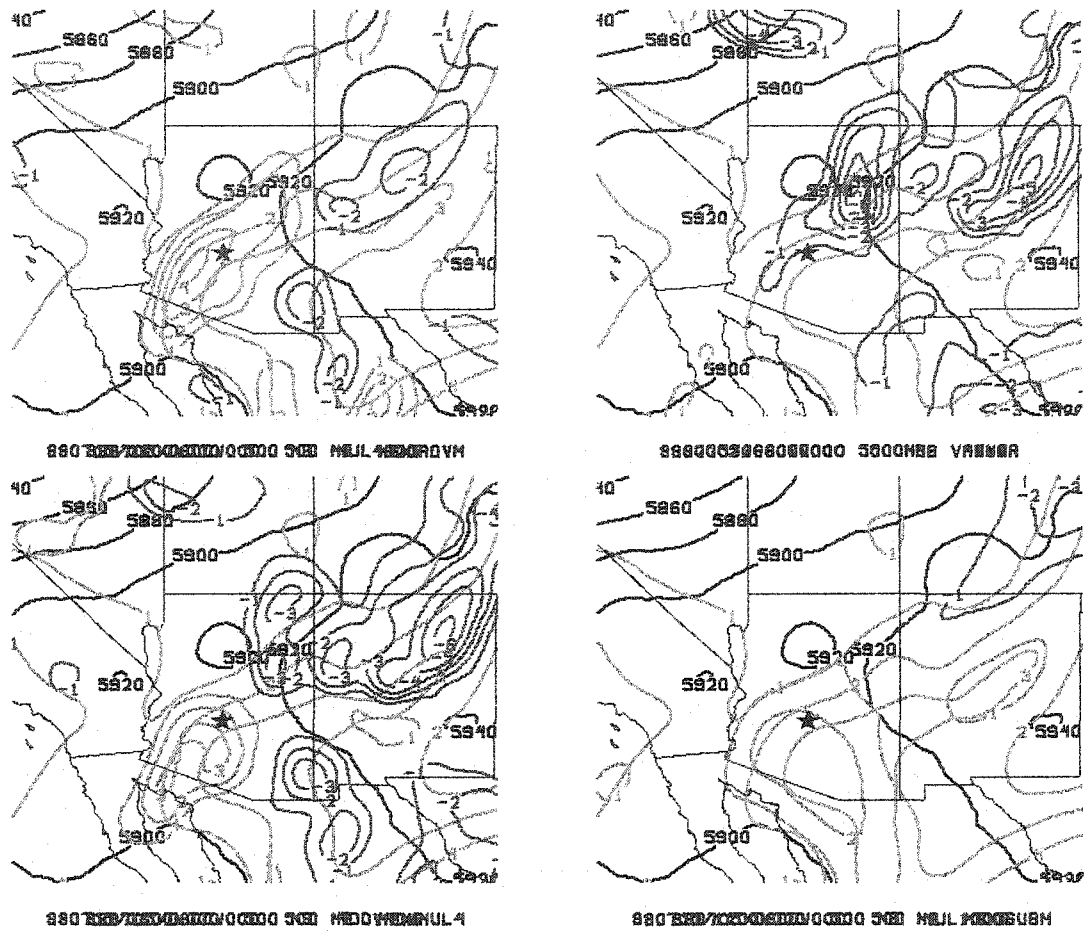
Figure 30. Terms comprising the mixing ratio tendency equation for the period spanning from 00–12 UTC 5 July 1999 at 500 mb, including a) quasihorizontal moisture advection, b) vertical moisture advection, c) calculated local mixing ratio tendency, and d) observed local mixing ratio tendency, all expressed in $(g\ kg^{-1})\ 12\ h^{-1}$. Green lines indicate 500-mb mixing ratio values at 6-h into the 12-h tendency calculation, blue lines indicate positive tendencies, and red lines indicate negative tendencies.

The relative importance of horizontal and vertical advection at 500 mb is demonstrated by examining terms comprising (8). In Fig. 30a, quasihorizontal advection of moisture between 00 and 12 UTC 5 July 1999 increases mixing ratio values by 1–4 g kg^{-1} within a northeasterly oriented swath extending from the northern Gulf of California to northeastern Arizona. During the same period, sub-sidence causes the vertical advection of moisture term to decrease mixing ratio values by 1–5 g kg^{-1} over northeastern Arizona (Fig. 30b). Together, these terms result in net moistening (up to 3 g kg^{-1}) over southwestern Arizona, and net drying (up to 3 g kg^{-1}) over northeastern Arizona (Fig. 30c). In Fig. 30d, local changes in mixing ratio show a pattern quite different from Fig. 30c, where mixing ratio values increase across the entire domain, rather than over over southwestern Arizona only. Since local changes in mixing ratio (Fig. 30d) correspond well with the quasihorizontal moisture advection term (Fig. 30a), the vertical advection term (Fig. 30b) is clearly to high. Thus, in this case, the RUC-2 model is apparently overestimating vertical motion values. Nonetheless, at Phoenix the similarity in the spatial pattern of local changes in mixing ratio and horizontal advection of mix-ing ratio (cf. Figs. 30a and 30d) demonstrates the importance of quasihorizontal advection to significant increases in moisture on 4–5 July 1999.

5.3.2 Northward development of the subtropical high

During 13–14 August 1999, significant 24-h moistening in the 12 UTC sounding at Phoenix and a northward developing subtropical high (Figs. 31 and

32) accompany a transition in regime from DR to NDR (Fig. 25b). Although mix-
ing ratio increases throughout most of the column, the maximum increase in mois-
ture occurs near 600 mb (Fig. 31). This increase in midlevel moisture is illustrated
by *GOES-10* water vapor imagery (Fig. 31) .

The maximum change in 600-mb mixing ratio occurs between 18 UTC 13
August and 06 UTC 14 July 1999. Although a light southwesterly wind occurs
over central Arizona, light southerlies occur south of central Arizona in response
to the subtropical anticyclone centered over the southern Arizona–New Mexico
border (Fig. 32a). High mixing ratio values are located south of Arizona, with
highest values over west-central Mexico and the Gulf of California (Fig. 32a).
During the next 12 h, high mixing ratios are advected northward by southerly flow
in response to the northward development the subtropical high (Figs. 32b,c).

The relative importance of horizontal and vertical advection is demon-
strated by examining terms comprising (8). In Fig. 33a, quasihorizontal advection
of moisture between 18 UTC 13 August and 06 UTC 14 August 1999 increases
mixing ratio values by 1–6 g kg^{-1} over southwestern Arizona and northwestern
Mexico. During the same period, upward vertical motion causes the verticalad-
vection of moisture term to increase mixing ratio values another 1–10 g kg^{-1} from
central to eastern Arizona (Fig. 33b). Together, these terms result in net moisten-
ing (up to 10 g kg^{-1}) over southwestern and eastern Arizona (Fig. 33c). In Fig.
33c, a net moistening of approximately 2.5 g kg^{-1} at Phoenix results fromboth
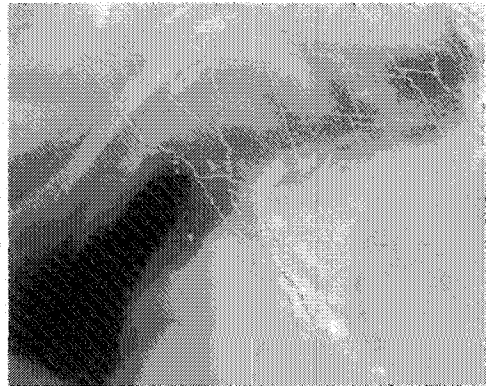
Figure 31. 12 UTC Phoenix soundings and GOES-10 water vapor imagery on 13 and 14 August 1999.
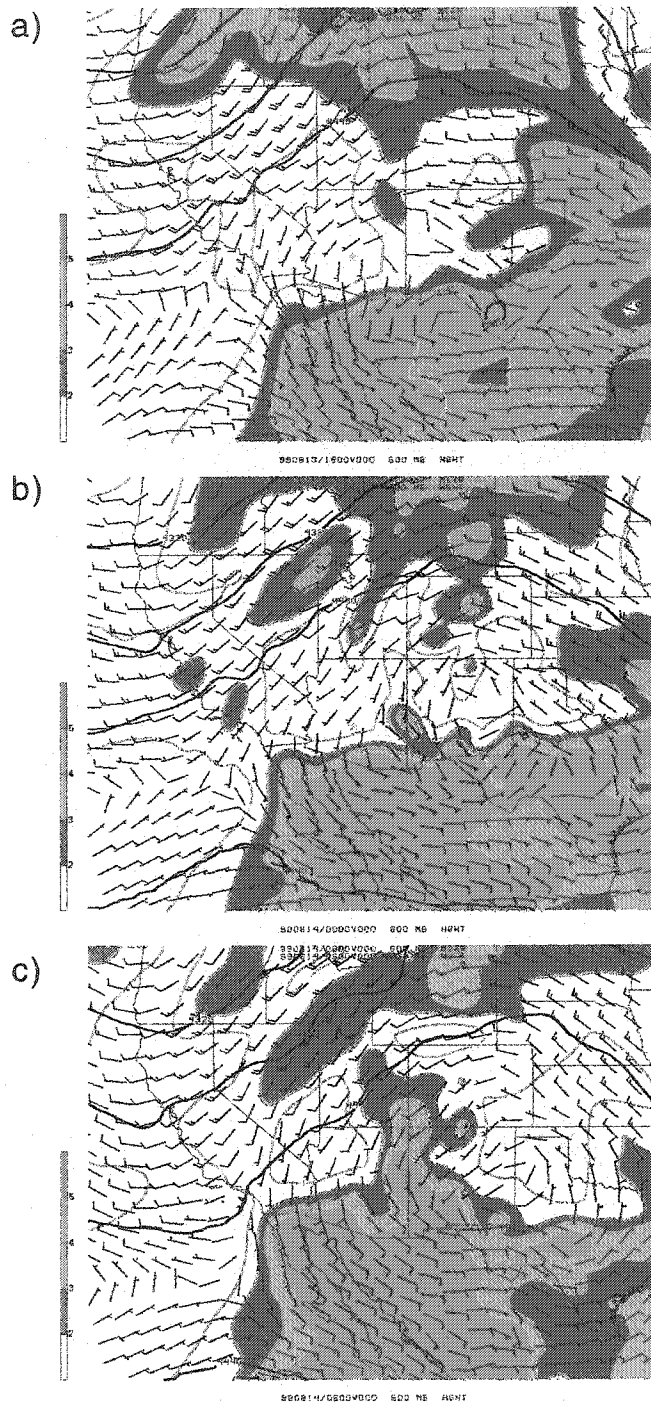
Figure 32. Same as in Fig. 29, only for a) 18 UTC 13 August 1999, b) 00 UTC 14 August 1999, and c) 06 UTC 14 August 1999.
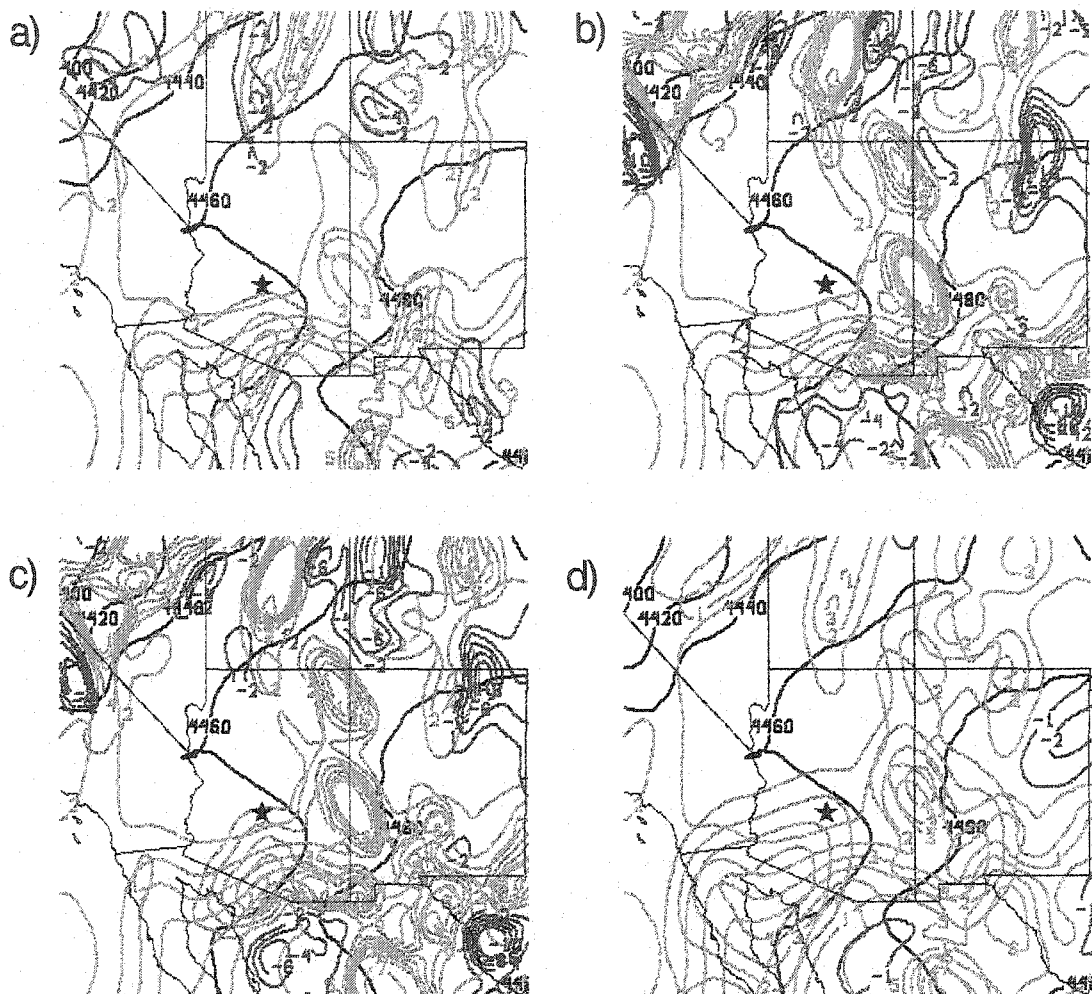
Figure 33. Same as Fig. 30, but for the period spanning from 18 UTC 13 August through 06 UTC 14 August 1999 at 600 mb, including a) quasihorizontal moisture advection, b) vertical moisture advection, c) calculated local mixing ratio tendency, and d) observed local mixing ratio tendency, expressed in (g kg^{-1}) 12 h^{-1}.

horizontal (1.5 g kg^{-1}) and vertical (1.0 g kg^{-1}) advection of moisture. Local changes in mixing ratio (Fig. 3ed) show a spatial pattern of mixing ratio tendencies similar to Fig. 33c, although values are lower, especially over parts of eastern Arizona and northwest Mexico.

5.3.3 Passage of shortwave trough in the westerlies

During 16–17 July 1999, significant 24-h drying in the 12 UTC sounding at Phoenix and a consistent westerly tropospheric wind (Fig. 34) accompany a transition in regime from NDR to DR (Figs. 25a,b). Although mixing ratio decreases throughout most of the column, the maximum decrease in moisture occurs near 500 mb (Fig. 34). Since the decrease in moisture occurs at 500 mb and below, this change in midlevel moisture is not apparent from *GOES -10* water vapor imagery (Fig. 34).

The maximum change in 500-mb mixing ratio occurs between 12 UTC 16 July and 00 UTC 17 July 1999. At 12 UTC 16 July, a shortwave trough in the westerlies is approaching Arizona (Fig. 35a). A mixing ratio gradient lies over Arizona, with the highest mixing ratio values located east of Arizona (Fig. 35a). During the next 12 h, high mixing ratios are advected eastward by westerly flow as the shortwave trough in the westerlies moves over Arizona (Figs. 35b, c).

The relative importance of horizontal and vertical advection is demonstrated by examining terms comprising (8). In Fig. 36a, quasihorizontal advection

104

of moisture between 12 UTC 16 August and 00 UTC 17 July 1999 decreases mixing ratio values by 1–4 g kg^{-1} over central Arizona, and 1–8 g kg^{-1} over north-central Arizona. During the same period, ascent ahead of the shortwave trough in the westerlies causes upward transport of moisture of 1–3 g kg^{-1} over central and east-central Arizona (Fig. 36b). However, subsiding air to the south acts to decrease moisture by similar amounts (Fig. 36b). Thus, together these terms result in net drying (up to 9 g kg^{-1}) over most of Arizona, including Phoenix (Fig. 36c).

Local changes in mixing ratio (Fig. 36d) show a pattern similar to Fig. 36c, although mixing ratio tendencies are lower over much of the domain. An exception is within the vicinity of Phoenix, where local changes in mixing ratio (Fig. 36d) are actually higher than the net change (Fig. 36c). In this region, the net change in mixing ratio (Fig. 36c) likely underestimates the actual local change in mixing ratio (Fig. 36d) because vertical advection is probably occurring over a period shorter than the 12-h used in this computation. Nonetheless, the similarity in the pattern of mixing ratio tendencies (cf. Figs. 36c and 36d) demonstrates the greater importance of quasihorizontal advection, compared to vertical advection, to the significant decreases in moisture on 16–17 July 1999.

In summary, about 50% of significant changes in precipitable water (upper and lower 20th percentile) are associated with abrupt changes in regime that result in either increased or decreased storm coverage. Results show that such
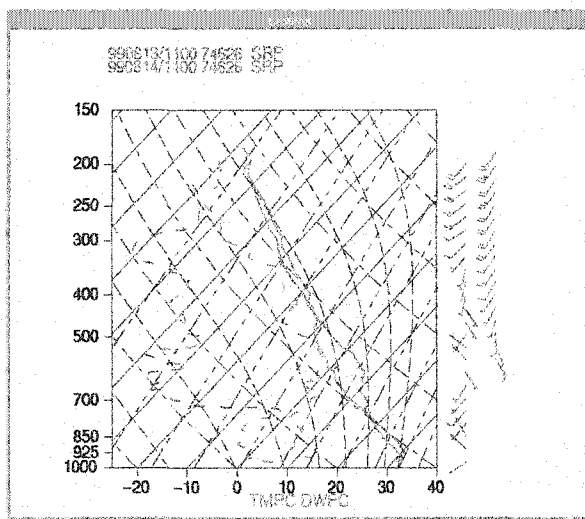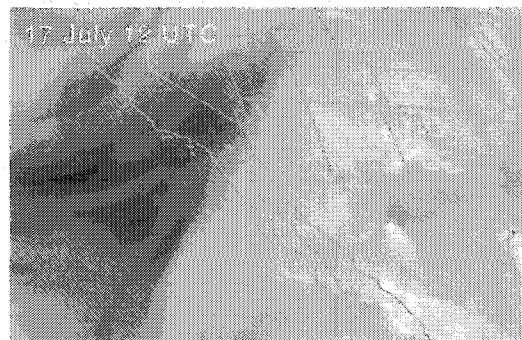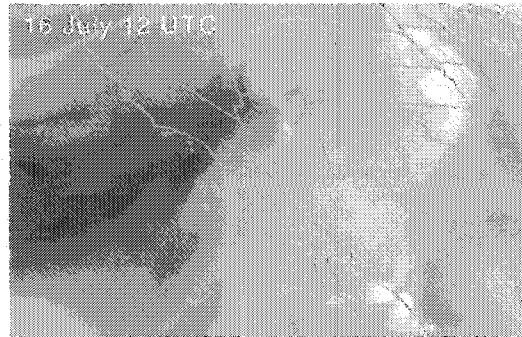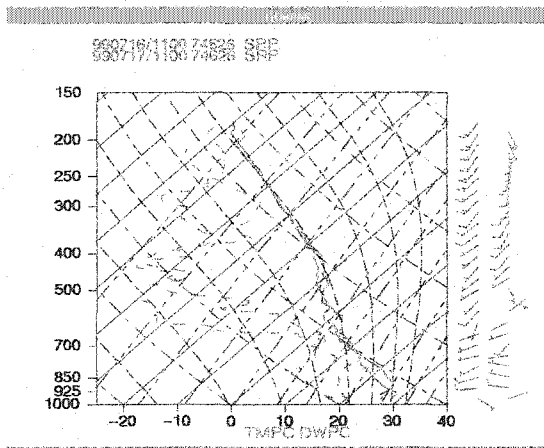
Figure 34. 12 UTC Phoenix soundings and GOES-10 water vapor imagery on 16 and 17 August 1999.
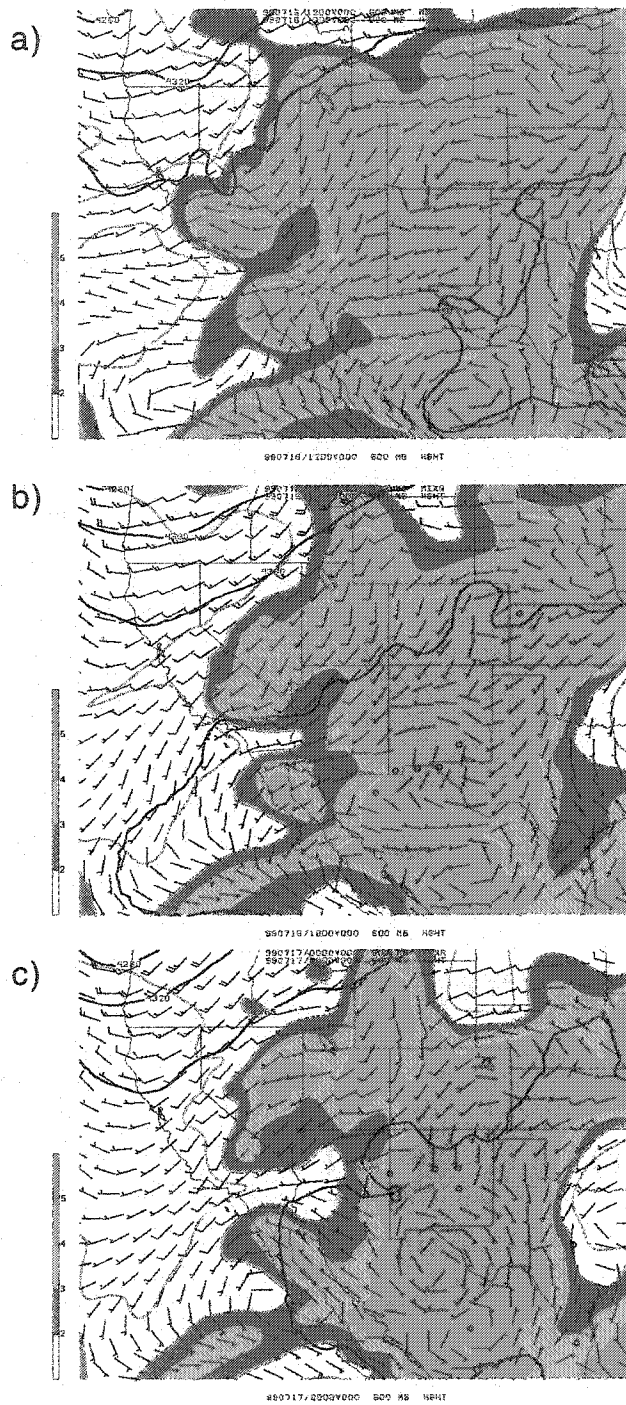
Figure 35. Same as in Fig. 29, only for a) 12 UTC 16 July 1999, b) 18 UTC 16 July 1999, and c) 00 UTC 17 July 1999.
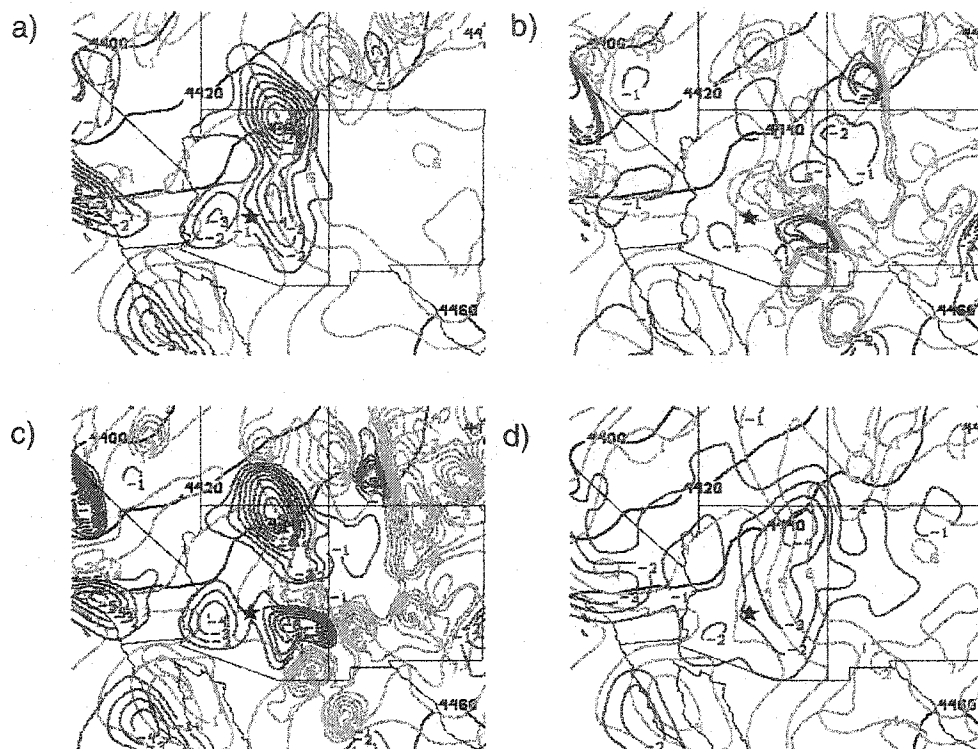
Figure 36. Same as Fig. 30, but for the period spanning from 12 UTC 16 July through 00 UTC 17 July 1999 at 600 mb, including a) quasihorizontal moisture advection, b) vertical moisture advection, c) calculated local mixing ratio tendency, and d) observed local mixing ratio tendency, expressed in (g kg^{-1}) 12 h^{-1}.

increases in moisture are caused primarily by quasihorizontal advection, which is associated with the shift in the location of the monsoon boundary. When large-scale lift is present over Arizona, increases in moisture are enhanced by vertical advection of moisture. On the other hand, decreases in moisture are associated with the passage of shortwave troughs in the westerlies. Therefore, the regional distribution of moisture between 700–400 mb depends heavily on the evolution of the large-scale flow.

Thus far, this discussion focuses on processes responsible for changes in moisture at 700 mb and higher, and neglects those below this level. The review of previous literature in Chapter 2 indicates that low-level moisture in Arizona originates from the Gulf of California, owing to the diurnal LLJ and occasional surges. Adams and Comrie (1997) point out that, although several papers imply a relationship between surges from the Gulf of California and changes in storm coverage over Arizona, such a connection remains unexplored at seasonal or longer time scales in the published literature. Since the current study seeks to improve understanding of intraseasonal variability, the relation of surges to significant changes in low-level moisture at Phoenix and storm coverage is investigated for the 1997 and 1999 NAMs.

5.4 Relation between surges and intraseasonal variability

The relation of surges to intraseasonal changes in moisture is addressed by examining the temporal relationship between the onset of surges at Yuma, Ari-

zona, and significant increases in low-level moisture at Phoenix. Following the criteria of Fuller and Stensrud (2000), surges from the Gulf of California are identified using time series of dewpoint temperature, wind direction, and wind speed from the surface station at Yuma, Arizona. Yuma is chosen because it is best available site for observing surges, located about 100 km north of the Gulf of California (Fuller and Stensrud 2000). The onset of a surge at Yuma is defined by an abrupt increase in dewpoint temperature to 60°F (15.6°C) or higher, and at least one observation of southerly near-surface winds and wind speed exceeding 4 m s^{-1} (Fuller and Stensrud 2000). The dewpoint temperature threshold is set at 60°F to represent the air temperature over the Gulf of California during the NAM (Stensrud et al. 1995). After the onset of a surge, the daily maximum dewpoint temperature must exceed this threshold during several consecutive days (Fuller and Stensrud 2000). The application of these criteria reveals that 18 surges occur in this study: ten in 1997 and eight in 1999.

A surge is considered a contributing factor to increases in low-level moisture at Phoenix if, within 24-h of surge onset, the observed 850–700-mb mixing ratio in the 12 UTC Phoenix sounding increases and wind direction over the Sonoran Desert is southerly to southwesterly within this same layer. Wind direction within the 850–700-mb layer above the Sonoran Desert is determined by combining 12 UTC Phoenix sounding data and 00 and 12 UTC National Center for Environmental Prediction (NCEP) upper-air charts. Both data sets are available for 14 of the 18 surges (Table 3).

The application of the above criteria reveals that 50% of surges contribute toward increases in low-level moisture at Phoenix (Table 3). This result complements Stensrud et al.'s (1997) numerical modeling study of surges, where strong gulf surges, or those that affect Arizona, tend to occur a few days following the passage of a midlatitude trough over the western United States. Based on results from section 5.3 and 5.4, the applicability of Stensrud et. al.'s (1997) finding likely depends on how the subtropical high evolves after a trough moves over Arizona: either creating a shift from westerly to 1) southwesterly or southerly flow, which is favorable to surges, or 2) southeasterly to easterly flow, which is unfavorable to surges. Given this result, a question of interest is whether increases in areal storm coverage are favored by surges that are more closely related to increases in low-level moisture at Phoenix.

A surge is considered a contributing factor to changes in regime if, within 48-h of surge onset, regime type transitions to a pattern with more areal storm coverage (e.g., DR to NDR; EMR to CEMSR). The application of these criteria reveal that 8 of the 14 surges (57%) at Yuma are associated with increases in areal storm coverage over the domain (Table 3). Of these eight surges, only two are not related to increases in low-level moisture at Phoenix. This finding implies that surges unaccompanied by increases in low-level moisture at Phoenix (5 of 7 or ~71%) result only occasionally in increased storm coverage over the domain. Therefore, when a forecaster observes a surge at Yuma, consideration

Table 3: Relation of surges to same or next day precipitable water (PWTR) at Phoenix and storm coverage within domain, where an 'X' indicates a positive association.

Surge Date / Time	Associated with significant change in PWTR at Phoenix	Associated with significant change in storm coverage
4 July 1997 / 2 UTC	X	
11 July 1997 / 10 UTC		
21 July 1997 / 00 UTC	X	X
27 July 1997 / 12 UTC	X	X
12 August 1997 / 12 UTC	X	X
26 August 1997 / 21 UTC		
6 July 1999 / 9 UTC		
17 July 1999 / 00 UTC		X
22 July 1999 / 4 UTC	X	X
27 July 1999 / 22 UTC		X
2 August 1999 / 20 UTC		
5 August 1999 / 4 UTC	X	X
14 August 1999 / 6 UTC	X	X
19 August 1999 / 9 UTC		

of the background low-level flow is strongly recommended to help assess the potential influence of the surge on storm development in Arizona.

In summary, time series of regimes and precipitable water values at Phoenix illustrate some temporal aspects of intraseasonal variability in the NAM over Arizona. For one, intraseasonal variability of precipitation during the 1997 and 1999 NAMs is characterized by fairly persistent regimes and occasional sharp changes in regime type, and, therefore, storm coverage. These sharp changes in storm coverage are associated with significant changes in precipitable water in 12 UTC soundings at Phoenix. In turn, associated changes in mixing ratio are tied to the evolution of the North Pacific trough, subtropical high, and surges from the Gulf of California.

The above results, combined with those in Chapters 3 and 4, present the opportunity to produce a summary (Chapter 6) that highlights conclusions concerning the intraseasonal variability in radar reflectivity patterns and the environment during the 1997 and 1999 NAM. Chapter 6 discusses also forecast implications arising from these results.

Chapter 6. Summary and Forecast Implications

Intraseasonal variability during the 1997 and 1999 NAMs consists primarily of five radar reflectivity regimes: DR, EMR, CEMR, CEMSR, and NDR, listed in the order of increasing areal storm coverage across the domain. Owing to the strong diurnal heating cycle, terrain forcing and high boundary layer lapse rates provide ample lift and instability for deep moist convection over Arizona's mountains almost daily. Therefore, the spatial distribution of tropospheric moisture controls the areal extent of storm development over elevated terrain. Indeed, 12 UTC composite 500-mb maps and Phoenix soundings of DR, EMR, and CEMR reveal three different synoptic-scale situations:

1. During DR, the subtropical high's horizontal ridge axis and the meridional moist axis are located south of Arizona, resulting in westerly wind and dry tropospheric conditions.

2. During EMR, the center of the subtropical high is located far eastward of Arizona and the North Pacific trough is located westward of Arizona, resulting in confluent flow and a moisture gradient over Arizona. In this case, the meridional moist axis is centered over western New Mexico.

3. During CEMR, EMR's synoptic-scale pattern is shifted westward, resulting in more moist conditions over most of Arizona.

These differences in flow occur through most of the troposphere, producing distinct differences in tropospheric moisture, and making precipitable water an excellent variable for discriminating among DR, EMR, and CEMR.

Although tropospheric moisture also controls storm development over lower elevations (e.g., CEMSR and NDR), high values of tropospheric moisture associated with such regimes help discriminate CEMSR and NDR from DR and EMR only. The lack of discrimination among CEMR, CEMSR, and NDR by precipitable water reflects the similarity in the location of the meridional moist axis, and hence the composite synoptic-scale flow. Regardless of these similarities, NDR is distinguished from CEMR and CEMSR by relatively high surface–6-km shear, owing to shortwave troughs embedded in westerly, southerly, or easterly flow. An acute awareness of mobile shortwave troughs in the flow is particularly important for predicting NDR because these systems sometimes contribute to heavy rainfall and flash flooding (e.g., 14 July 1999, *Storm Data 1999*).

In summary, the discriminant analysis of 12-UTC precipitable water and surface–6-km shear at Phoenix indicates that this model of intraseasonal variability performs best (e.g., has highest Heidke Skill Score) when a forecaster is considering the potential for DR, EMR, or a wet regime (CEMR, CEMSR, or NDR) within the next 24-h. Even though the discriminant analysis becomes less skillful when considering the potential for one or more of the wet regimes (e.g., especially CEMR vs. CEMSR), as a whole, the combined discriminant analysis (Fig. 23) has more skill than a random forecast (HSS=0.43), and is more accurate than persistence or a one in five guess. Thus, this model is a promising model for 12-h forecasts of areas where precipitation is most likely.

115

Another aspect of intraseasonal variability is the daily persistence of regimes. DR is the most persistent regime, followed by CEMR, NDR, EMR, and CEMSR. The extreme persistence of DR (82% before and after), combined with its distinctive environmental characteristics, makes DR the easiest regime to forecast—especially prior to monsoon onset. In contrast, even though CEMR is one of the more persistent (48% before and 42% after) regimes, it is quite difficult to forecast. This forecast difficulty arises from the approximately equal chance of CEMR being followed by either itself or CEMSR, and, the similarity in these regimes' environmental conditions. Although CEMSR is less persistent (33.4% before and 21% after) than CEMR, the relatively high next-day occurrence (47%) of CEMR provides an additional piece of climatological information which may improve a forecaster's confidence while discerning the potential for these regimes within the next 12-h.

Occasionally, sharp changes in storm coverage precede or follow a given regime. Such sharp changes are most likely prior to or following EMR or NDR. Since such sharp changes in regime type are closely tied to significant changes in precipitable water at Phoenix, tracking the temporal and spatial evolution of tropospheric moisture is important. At mid–upper-levels significant local changes in moisture arise mostly from quasi-horizontal advection, in response to changes in the synoptic-scale flow. In most cases, moistening corresponds with the westward or northward expansion of the subtropical high, whereas drying corresponds

with the passage of a shortwave trough. Occasionally, mid–upper-level moisten-

ing is enhanced by the vertical advection of moisture ahead of shortwave troughs.

At low-levels in Phoenix, significant changes in moisture at 12 UTC are

associated with three situations: precipitation in the vicinity of Phoenix the previ-

ous night (30%), surges from the Gulf of California (35%), and moisture advection

east or southeast of Phoenix (35%). Interestingly, surges appear more important

to the return of low-level moisture at Phoenix in 1997 than 1999, where 44% and

27%, respectively, of significant increases in precipitable water are associated

with surges. Since 2.5 times as much precipitation fell at Phoenix during 1999

NAM than 1997 NAM (3.88" vs. 1.56", 1.79" is 30-y average), more active mon-

soons may depend less strongly on surges for low-level moisture. Nonetheless,

since gulf surges can contribute strongly to the return of low-level moisture at

Phoenix, when a forecaster observes a surge at Yuma, consideration of the speed

and direction of the low–midlevel background flow is recommended to help

assess its potential influence on changes in moisture and storm coverage (i.e.,

northward progress of the surge).

When the current study began (1999), operational models were unable to

forecast precipitation patterns similar to those observed (Dunn and Horel 1994a).

Although Stensrud et al. (1995) had shown success in simulating prominent mean

features of the NAM with the nonoperational PSU/NCAR mesoscale model, MM5

(Grell et al. 1994), special observations from SWAMP were required to attain

these results. Thus, accurate regional forecasts of storm development depended

heavily on nonoperational datasets. Even if models performed relatively well in

this region, operational datasets are essential to the forecast process. For one,

they provide the ground truth necessary for real-time verification of model perfor-

mance. In addition, these datasets allow forecasters to monitor hazardous

weather and the diurnal evolution of the environment. Under these circum-

stances, it was important to investigate and establish a physically consistent way

to handle forecasts of storm coverage using operational datasets.

A primary concern of this study was to help forecaster discern better those

days where storms move off the mountains and into Phoenix-Mesa from those

where storms develop over the mountains only (CEMSR vs. CEMR). Since the

resulting discriminant analysis model (Fig. 23) has forecast skill over a random

forecast, this model is a step forward in providing forecasters with a tool to help

discern between these regimes, using the 12 UTC Phoenix sounding. From a

nowcast perspective, the more distinct band of higher late afternoon relative fre-

quencies of reflectivity over the Mogollon Rim during CEMSR, compared to

CEMR, suggests that contiguous storm development over these mountains is a

promising indicator of CEMSR. Nonetheless, an unanswered question concerns

the mechanisms responsible for the difference in storm evolution between these

regimes. The similarity in their measurable 12 UTC environmental characteristics

suggest that the development of CEMSR vs. CEMR may be tied to the diurnal

evolution of synoptic-scale flow, terrain-driven circulations, and/or internal storm

dynamics. Detailed study of these mechanisms by idealized mesoscale model simulations or higher-resolution datasets may, in turn, provide even better scientif-ically-based tools for discerning these regimes.

Appendix A: Adaptive Barnes Interpolation

This research implements an adaptive Barnes interpolation scheme (Askelson 2000; Trapp and Doswell 2000; Zhang 2000) that filters radial radar reflectivity data in radial, azimuthal and vertical directions. Accordingly, the raw reflectivity factor, f, is interpolated from polar coordinates, $f_i(r, \theta, \phi)$, to Cartesian coordinates, $f_g(x, y, z)$ (e.g., Trapp and Doswell):

$$f_g(x, y, z) = \frac{\sum\limits_{i}^{N} w_i f_i(r, \theta, \phi)}{\sum\limits_{i=1}^{N} w_i}, \tag{A1}$$

where the weighting factor w_i is defined as:

$$w_i = \exp\left[-\frac{(r_g - r_i)^2}{\kappa_r} - \frac{(\theta_g - \theta_i)^2}{\kappa_\theta} - \frac{(\phi_g - \phi_i)^2}{\kappa_\phi} \right],$$

where r, θ, ϕ represent polar coordinates of distance, azimuth, and elevation, x, y, z represent Cartesian coordinates of horizontal distance and height, the subscript i represents a bin of raw reflectivity data in polar coordinates, the subscript g represents the grid point at which the analysis is produced, N is the number of radar bins influencing the interpolated grid value, and $\kappa = \kappa(r, \theta, \phi)$ are dimensional filtering parameters. These filtering parameters are defined as (e.g., Trapp and Doswell 2000):

$$\kappa_r = \kappa * L_r^2 \quad , \tag{A2}$$

$$\kappa_\theta(r) \ = \ \kappa * L_\theta^2(r) \text{, and} \tag{A3}$$

$$\kappa_\phi(r) \ = \ \kappa * L_\phi^2(r) \text{,} \tag{A4}$$

where $\kappa *$ denotes the non dimensional filtering parameter,

$\kappa * = -\log(0.65)\pi^{-2} \ = \ 0.0189$, chosen to retain the highest possible resolution

of the raw data within the analysis (Zhang, personal communication), and

L_r, $L_\theta(r)$, and $L_\phi(r)$ denote radial (2 km), azimuthal (2°), and elevation (°, var-

ies with height and volume coverage pattern (VCP)) length scales, respectively

(personal communication, Zhang). Range-dependent filtering results because

azimuthal- and elevation-length scales increase with increasing range (Fig. A1).

As shown below, application of these adaptive length scales results in azimuthal

and vertical response functions whose magnitude diminishes with increasing

range.

The three-dimensional response function determines how much a given wave-

length, $\lambda(r, \theta, \phi)$, is filtered within a given volume, at a given range. This

response function is given by (e.g., Trapp and Doswell 2000):

$$D(\lambda^*) \ = \ e^{-\kappa^*\left(\frac{\pi}{\lambda^*}\right)} \text{,} \tag{A5}$$

where λ^* is a non dimensional wavelength in each direction:

$$\lambda_r^* = \frac{\lambda_r}{L_r}\,, \qquad\qquad\qquad\qquad \text{(A6)}$$

$$\lambda_\theta^* = \frac{\lambda_\theta(r)}{L_\theta(r)}\,, \qquad\qquad\qquad\qquad \text{(A7)}$$

and

$$\lambda_\phi^* = \frac{\lambda_\phi(r)}{L_\phi(r)}\,. \qquad\qquad\qquad\qquad \text{(A8)}$$

In A6–A8, $\lambda(r, \theta, \phi)$ is a fixed length scale in each dimension.

To illustrate the impact of $D(\lambda^*)$ in each dimension, I examine the response function for five different wavelengths, including 2 km, 4 km, 6 km, 8 km, and 10 km, at six ranges (50–300-km range, in 50 km increments) from a WSR-88D running in VCP 11 (14 elevation slices from 0.5° to 19.5°). In the radial direction (Fig. A2), the response function is constant with increasing range, resolving wavelengths associated with thunderstorms and larger-scale phenomena best. For the azimuthal direction (Fig. A3), the response function diminishes most sharply with increasing range at 2-km wavelengths, with a value near zero beyond 250 km in range. In contrast, the response function diminishes least at 10-km wavelengths, with values ranging from 0.99 to 0.8 between 1 km and 300 km, respectively (Fig. A3). Thus, as range increases, each wavelength is filtered more strongly (Fig. A3).

In the vertical direction, response functions are computed at 0.5°, 7.5°, 12°, and 16.7° elevation angles to show the filtering of various wavelengths (2-km, 4-km, 6-km, 8-km, and 10-km) within VCP 11, with respect to range (Fig. A4). Indeed, comparison of Figs. A4a–A4d shows that the response function (filtering) decreases (increases) with increasing range from the radar, at all elevations and wavelengths. At all wavelengths, the response function at the 0.5° (16.7°) elevation drops off the least (most) with increasing range from the radar. This exercise shows that wavelengths associated with thunderstorms and larger-scale phenomena are resolved best near the radar, as a function of range, in all three dimensions.
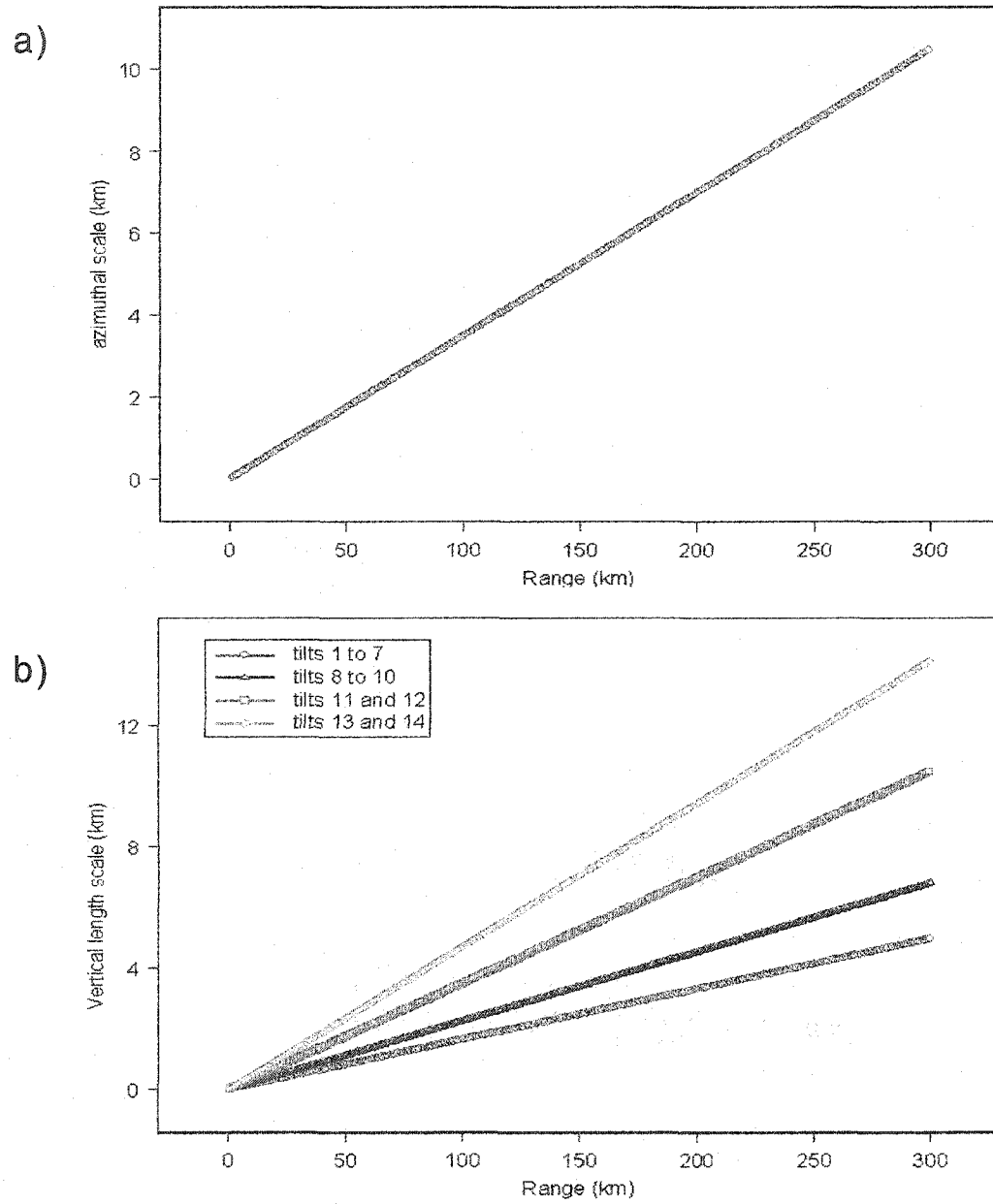
Figure A1. a) Azimuthal length scale, $L_\theta(r)$, and b) vertical length scale, $L_\phi(r)$, for volume coverage pattern 11, out to 300 km range.
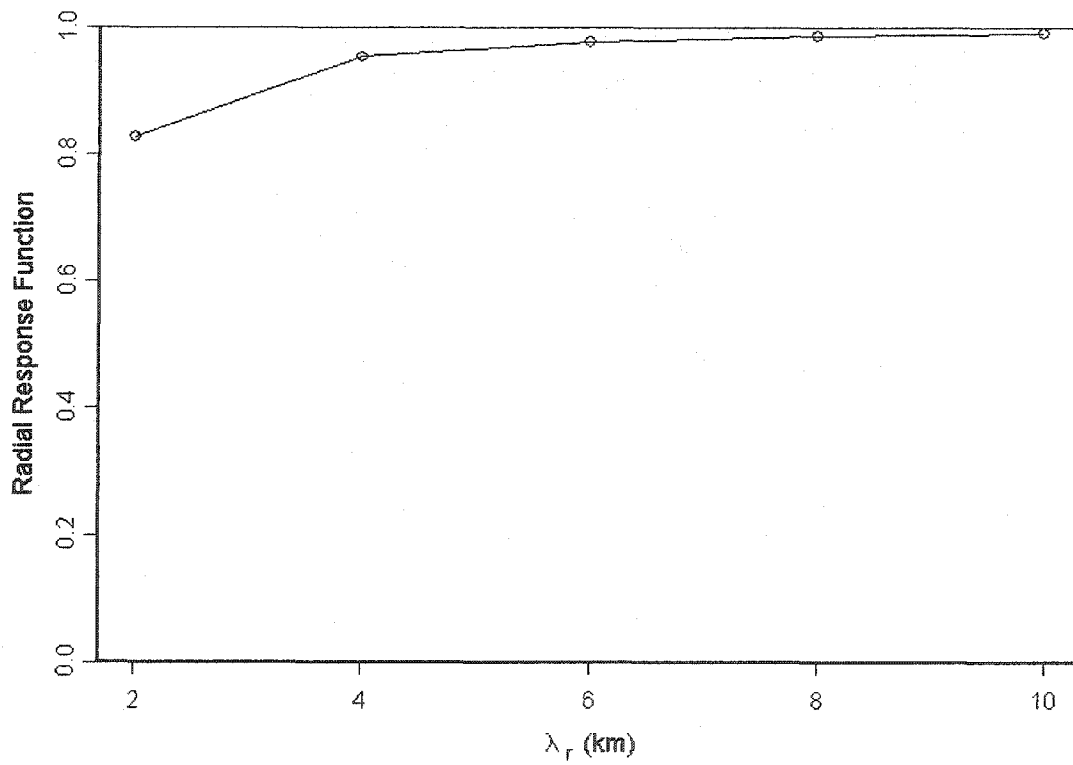
Figure A2. Radial response function with respect to radial wavelength.

Figure A3. Response function, $D(\lambda_\theta^*)$, where λ_θ^*, the azimuthal nondimensional wave-length, is computed at the following fixed ranges: 1 km (blue), 50 km (maroon), 100 km (green), 150 km (orange), 200 km (light blue), 250 km (brown), and 300 km (red) from the radar, for five dimensional wavelengths ($\lambda = \dfrac{2\pi}{k}$, upper x-axis) and wavenumbers (lower x-axis).

126

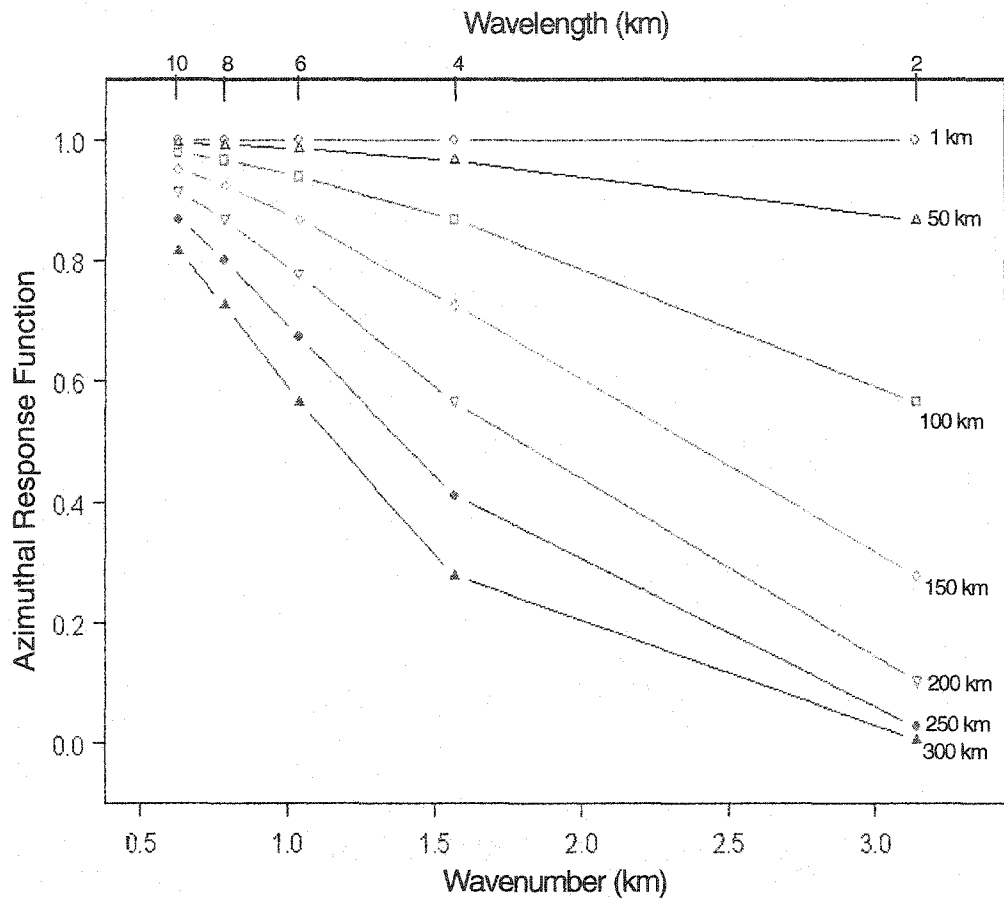Figure A4. Response function, $D(\lambda_\phi^*)$, where λ_ϕ^*, the elevational non dimensional wavelenth, is computed at fixed four elevation angles (0.5°, 7.5°, 12°, and 16.7°) at a range of a) 50 km, b) 100 km, c) 200 km, and d) 300 km from the radar, for five dimensional wavelengths ($\lambda = \dfrac{2\pi}{k}$, upper x-axis), and wavenumbers (lower x-axis).
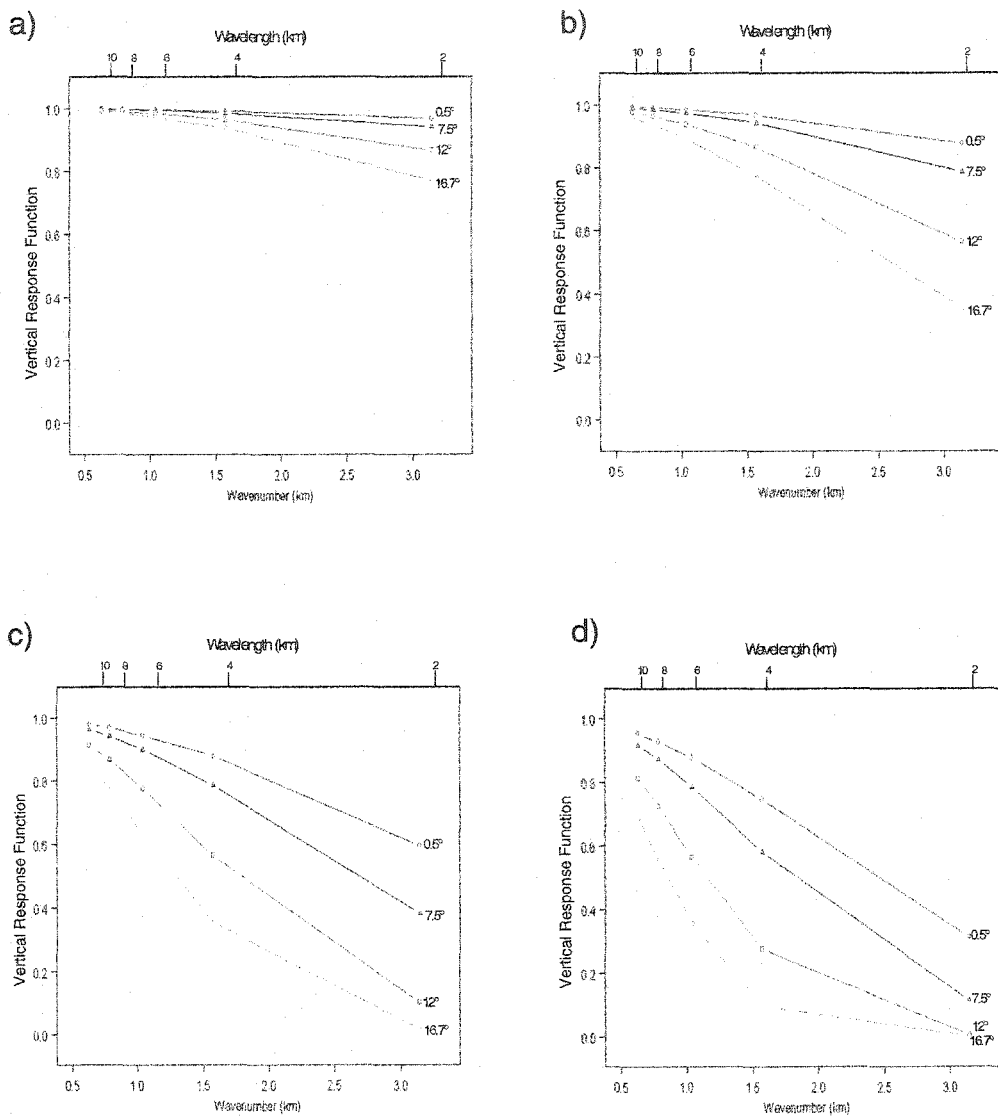
Appendix B: Linear Discriminant Analysis

The goal of discriminant analysis is to classify a new event correctly based on its observed characteristics (Wilks 1995, 408). Following Wilks (1995, 409–415), discrimination among events arises from a "training sample" that is used to build a linear relationship between two groups. These groups are denoted by two data matrices, $[X_1]$, dimensioned (n_1 x K), and $[X_2]$, dimensioned (n_2 x K), where n_1 is the number of observations in group one, n_2 is the number of observations in group two, and K is the vector dimension (in this study, $K = 2$).

First, find K-dimensional mean vectors:

$$\bar{x}_g = \frac{1}{n_g}[X_g]^T 1 = \begin{pmatrix} \dfrac{1}{n_g} \displaystyle\sum_{i=1}^{n_g} x_{i,1} \\ \dfrac{1}{n_g} \displaystyle\sum_{i=1}^{n_g} x_{i,2} \end{pmatrix}, g = 1, 2, \tag{B1}$$

where 1 is a (n x 1) vector containing only 1's. See Fig. B1 for an example of mean vectors from this study. Second, find a direction, d_1, in the K-dimensional space of the data such that the distance between $\bar{x}_1$ and $\bar{x}_2$ is maximized when the data are projected onto d_1. The discriminant vector d_1 is given by:

$$d_1 = [S_{pooled}]^{-1}(\bar{x}_1 - \bar{x}_2), \tag{B2}$$

128

where,

$$[S_{pooled}] = \frac{(n_1 - 1)[S_1] + (n_2 - 1)[S_2]}{(n_1 + n_2 - 2)} \tag{B3}$$

is a pooled estimate of the dispersion of the data around their means, and $[S_1]$ and $[S_2]$

are sample covariance matrices:

$$[S_g] = \frac{1}{n_g - 1}[X'_g]^T[X'_g] \quad , \tag{B4}$$

and

$$[X'] = [X_g] - \frac{1}{n_g}[1][X_g] . \tag{B5}$$

According to Wilks (1995, 409), the computation of d_1 assumes that "the population

underlying each of the groups has the same covariance matrix." See Fig. B2 for an example of d_1

projected onto two sample groups.

Third, find Fisher's linear discriminant function, $\bar{\delta}_1 = d_1^T \frac{\overline{x}_1 + \overline{x}_2}{2}$, which is

the midpoint between the means of x_1 and x_2. In turn, this value, $\bar{\delta}_1$, "defines the dividing line

between values of the discriminant function $d_1^T y$ for a future observation y that would result in its

being assigned to either group one or group two" (an example is shown in Fig. B3).
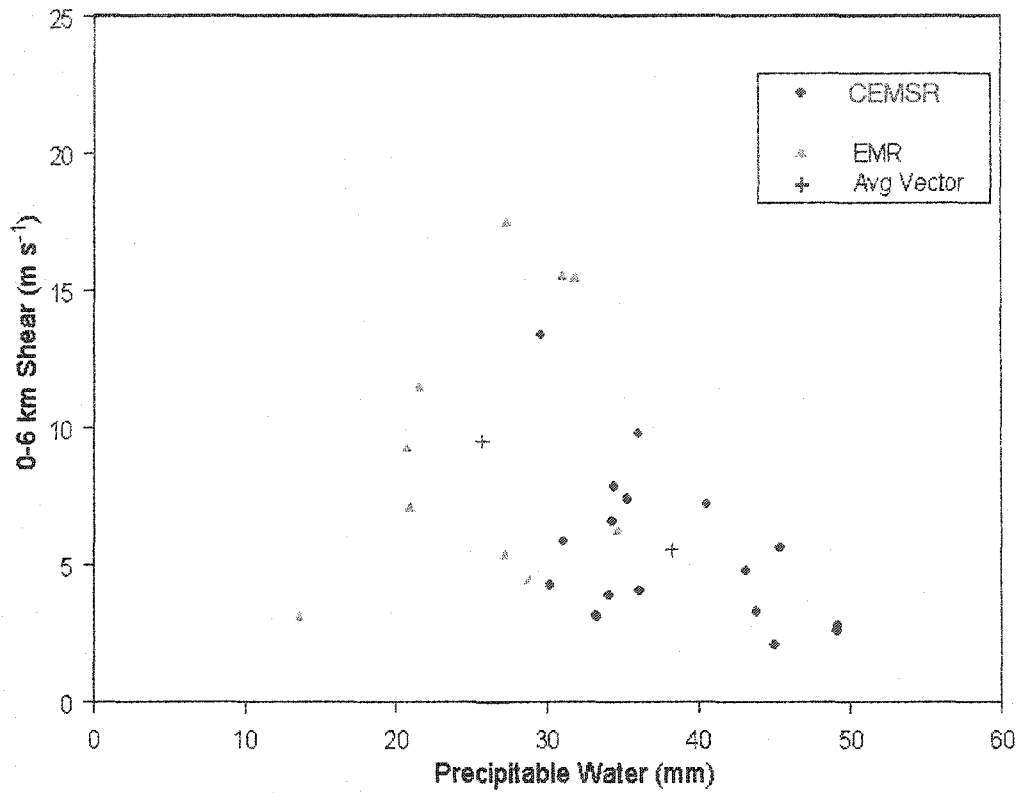
Figure B1. An example of training samples, $[X_1]$ and $[X_2]$, or characterstics of the eastern mountain regime (EMR; triangles) and central–eastern mountain and Sonoran regime (CEMSR; circles). The average vectors, $\bar{x}_1$ and $\bar{x}_2$ for each sample are given by the cross-hairs.

Figure B2. Same as Fig. B1, only showing the discriminant vector d_1.

Figure B3. Same as Fig. B2, only showing Fisher's linear discriminant function, δ_1, or the dividing line between the two groups, EMR and CEMSR..

References

Adams, D. K., and A. C. Comrie, 1997: The North American monsoon. *Bull. Amer. Meteor. Soc.*, **10**, 2197–2213.

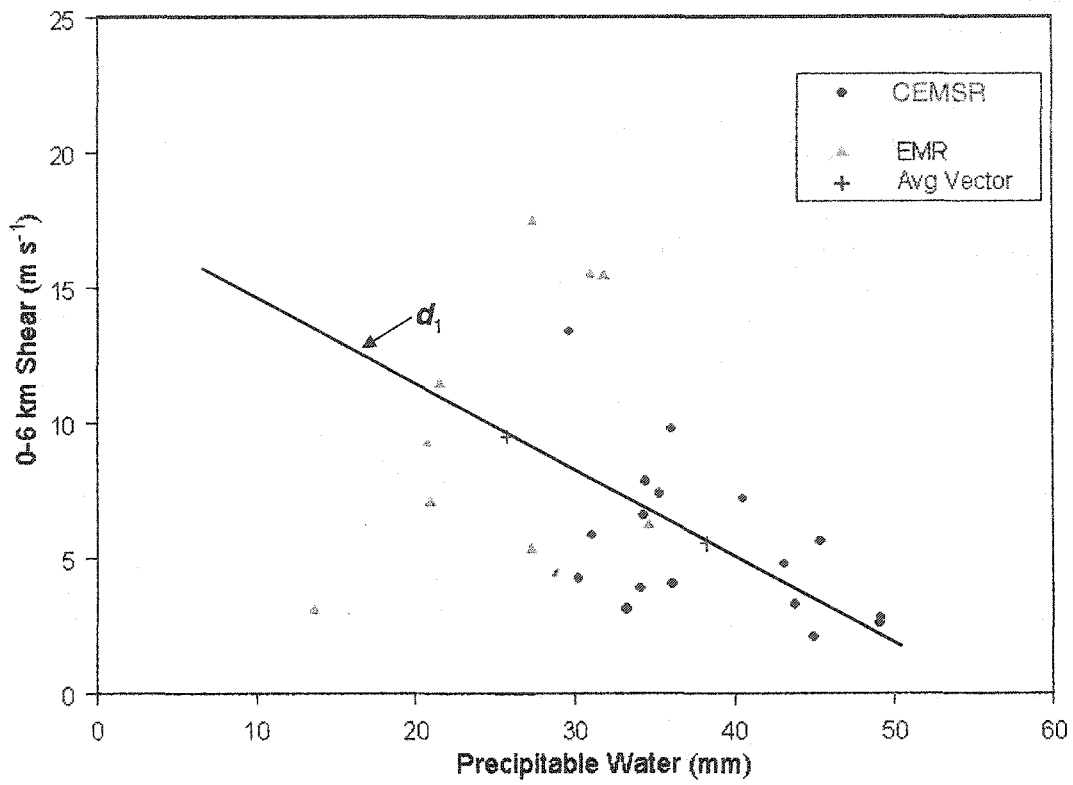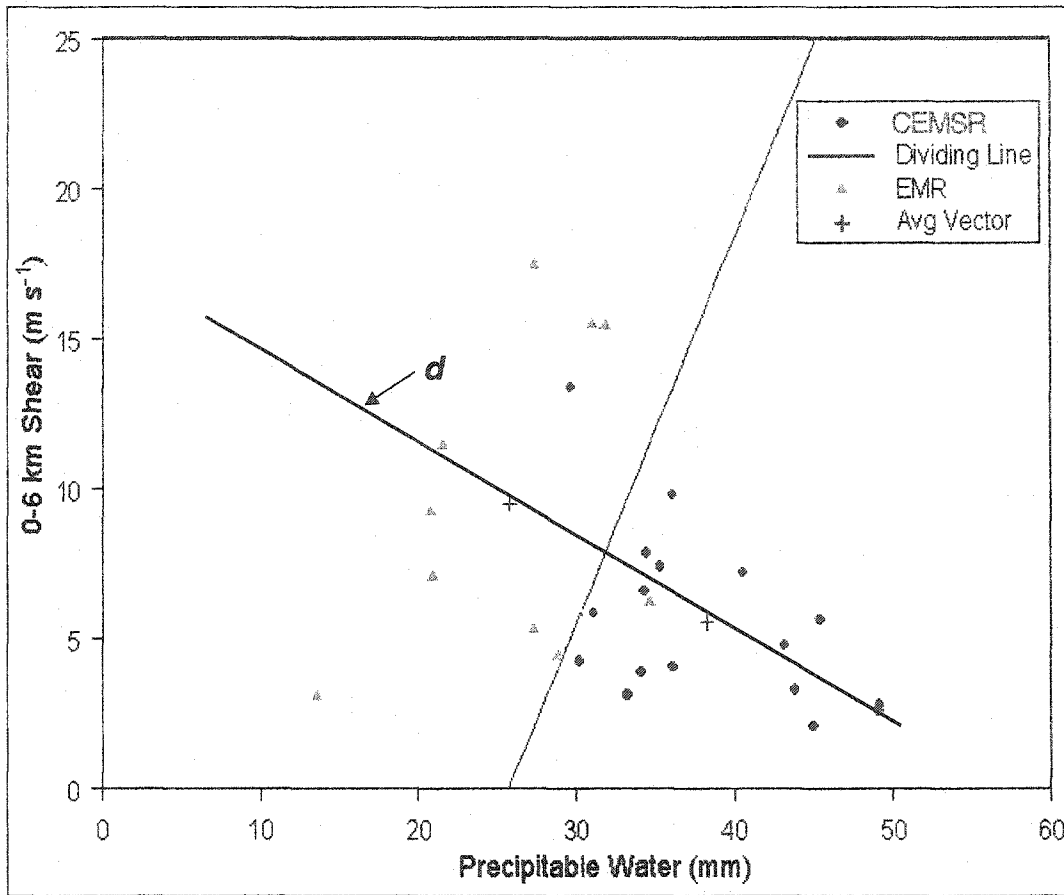Adang, Thomas C., Gall, Robert L. 1989: Structure and Dynamics of the Arizona Monsoon Boundary. *Mon. Wea. Rev.*, **7**, 1423–1438.

Anderson, B. T., J. O. Roads, and S-C. Chen, 2000: Large-scale forcing of summertime monsoon surges over the Gulf of California and the southwestern United States. *J. Geophys. Res.*, **105**, 24455–24467.

Askelson, M. A., J-P. Aubagnac, and J. M. Straka, 2000: An adaptation of the Barnes filter applied to the objective analysis of radar data. *Mon. Wea. Rev.*, **128**, 3050–3082.

Balling, R. C., and S. A. Brazel, 1987: Diurnal variations in Arizona monsoon precipitation frequencies. *Mon. Wea. Rev.*, **115**, 342–346.

Bagdan-Dangon, A., C. E. Dorman, M. A. Merrifield, and C. D. Winant, 1991: The lower atmosphere over the Gulf of California. *J. Geophys. Res.*, **96**, 877–896.

Banta, R. M., 1990: The role of mountain flows in making clouds. *Atmospheric processes over complex terrain*, W. Blumen, Ed., Amer. Meteor. Soc., 229–282.

Barnes, S. L., 1964: A technique for maximizing details in numerical weather map analysis. *J. Appl. Meteor.*, 3, 396–409.

Beals, E. A., 1922: The semipermanent Arizona low. *Mon. Wea. Rev.*, **50**, 341–347.

Benjamin, S.G., J.M. Brown, K.J. Brundage, B.E. Schwartz, T.G. Smirnova, and T.L. Smith, 1998: The operational RUC-2. Preprints, *16th Conference on Weather Analysis and Forecasting*, AMS, Phoenix, 249-252.

Blake, D., 1923: Sonora storms. *Mon. Wea. Rev.*, **51**, 585–588.

Brenner, I. S., 1974: A surge of maritime tropical air—Gulf of California to the southwestern United States. *Mon. Wea. Rev.*, **102**, 375–389.

Bright, David R., Mullen, Steven L. 2002: Short-range ensemble forecasts of precipitation during the southwest monsoon. *Wea. Forecasting*, **17**, 1080–1100.

------, ------, 2002: The sensitivity of the numerical simulation of the southwest monsoon boundary layer to the choice of PBL turbulence parameterization in MM5. *Wea. Forecasting*, **17**, 99–114.

Brooks, H. B., 1946: A summary of some radar thunderstorm observations. *Bull. Amer. Meteor. Soc.*, **27**, 557–563.

Bryson, R. A., and W. P. Lowry, 1955: Synoptic climatology of the Arizona summer precipitation singularity. *Bull. Amer. Meteor. Soc.*, **36**, 329–339.

Campbell, A., 1906: Sonora storms and Sonora clouds of California. *Mon. Wea. Rev.*, **34**, 464–465.

Carleton, A. M., 1986: Synoptic-dynamic character of 'bursts' and 'breaks' in the south-west U.S. summer precipitation singularity. *J. Climate*, **6**, 605–623.

Crook, N. Andrew. 1996: Sensitivity of Moist Convection Forced by Boundary Layer Processes to Low-Level Thermodynamic Fields. *Mon. Wea. Rev.*, **124**, 1767–1785.

Douglas, M. W., R. A. Maddox, and K. Howard, 1993: The Mexican monsoon. *J. Climate*, **6**, 1665–1677.

------,1995: The summertime low-level jet over the Gulf of California. *Mon. Wea. Rev.*, **123**, 2334–2347.

------, and S. Li, 1996: Diurnal variation of the lower-tropospheric flow over the Arizona low desert from SWAMP-1993 observations. *Mon. Wea. Rev.*, **6**, 1211–1224.

------, and J. C. Leal, 2003: Summertime surges over the Gulf of California: Aspects of their climatology, mean structure, and evolution from radiosonde, NCEP reanalysis, and rainfall data. *Wea. Forecasting*, **18**, 55–74.

Dunn, L. B., and J. D. Horel, 1994a: Prediction of central Arizona convection. Part I: Evaluation of the NGM and Eta model precipitation forecasts. *Wea. Forecasting*, **9**, 495–507.

Fuller, R. D., and D. J. Stensrud, 2000: The relationship between tropical easterly waves and surges over the Gulf of California during the North American monsoon. *Mon. Wea. Rev.*, **128**, 2983–2989.

Fulton, R. A., J. P. Breidenbach, D-J Seo, D. A. Miller, and T. O'Bannon, 1998: The WSR-88D rainfall algorithm. *Wea. Forecasting*, **13**, 377–295.

Fujita, T., K. S. Styber, R. A. Brown, 1962: On the mesometeorological field studies near Flagstaff, Arizona. *J. Appl. Meteor.*, **1**, 26–42.

Gourley, J.J., J. Zhang, R.A. Maddox, C.M. Calvert, K.W. Howard, 2001: A real-time precipitation monitoring algorithm - Quantitative Precipitation Estimation and Segregation Using Multiple Sensors (QPESUMS). Preprints, *Symp. on Precipitation Extremes: Prediction, Impacts, and Responses,* Albuquerque, Amer. Meteor. Soc., 57–60.

Grell, G. A., J. Dudhia, and D. R. Stauffer, 1994: A description of the fifth-generation Penn State/NCAR Mesoscale Model (MM5). NCAR Tech. Note NCAR/ TN-398+STR, 121 pp.

Hales, J. E., 1972a: Surges of maritime tropical air northward over the Gulf of California. *Mon. Wea. Rev.*, **100**, 298–306.

-----, 1972b: A study of radar echo distribution in Arizona during July and August. NOAA Tech. Memo. NWS WR-77, 1–21.

-----, 1974: Southwestern United States summer monsoon source—Gulf of Mexico or Pacific Ocean? *J. Appl. Meteor.*, **13**, 331–342.

-----, 1975: A severe southwest desert thunderstorm: 19 August 1973. *Mon. Wea. Rev.*, **103**, 344–351.

-----, 1977: On the relationship of convective cooling to nocturnal thunderstorms at Phoenix. *Mon. Wea. Rev.*, **105**, 1609–1613.

Higgins, R. W., Y. Yao, and X. L. Wang, 1997: Influence of the North American monsoon system on the U.S. summer precipitation regime. *J. Climate*, **10**, 2600–2622.

Houghton, J. G., 1979: A model for orographic precipitation in the north-central Great Basin. *Mon. Wea. Rev.*, **107**, 1462–1475.

Johns, Robert H., Doswell, Charles A. 1992: Severe Local Storms Forecasting. *Wea. Forecasting*, **7**, 588–612.

Jurwitz, L. R., 1953: Arizona's two-season rainfall pattern. *Weatherwise*, **6**, 96–99.

Kalnay, E., M. Kanamitsu, R. Kistler, W. Collins, D. Deaven, L. Gandin, M. Iredell, S. Saha, G. White, J. Woollen, Y. Zhu, A. Leetmaa, and B. Reynolds, 1996: The NCEP/NCAR reanalysis 40-year project. *Bull. Amer. Meteor. Soc.*, **77**, 437-472.

King, T. S., and R. C. Balling, 1994: Diurnal variations in Arizona monsoon lightning data. *Mon. Wea. Rev.*, **122**, 1659–1664.

MacKeen, P. L., and J. Zhang, 2000: Convective climatology for central Arizona during the 1999 monsoon. Postprints, *Southwest Weather Symposium*, Tucson, AZ, 64–67.

Magana, V. O., and P. J., Webster, 1998: CLIVAR monsoon conference: Monsoons. Preprints, *CLIVAR Conference*, Paris, France, December 1–3, 34 pp.

Moller, A., 2001: Severe Local Storms Forecasting. *Severe Convective Storms*, C. A. Doswell, Ed., Amer. Meteor. Soc., 433–480.

Mullen, S. L., J. T., Schmitz, and R. O. Renno, 1998: Intraseasonal variability of the summer monsoon over southeast Arizona. *Mon. Wea. Rev.*, **126**, 3016–3035.

NCDC, 1999: *Storm Data*. Vol. 41, No. 7.

Rasmussen, E. M., 1967: Atmospheric water vapor transport and the water balance of North America: Part I. Characteristics of the water vapor flux field. *Mon. Wea. Rev.*, **95**, 403–426.

Reed, T. R., 1933: The North American high level anticyclone. *Mon. Wea. Rev.*, **61**, 321-325.

-----, 1939: Thermal aspects of the high-level anticyclone. *Mon. Wea. Rev.*, **67**, 210–204.

Rowson, D. R., and S. J. Colucci, 1992: Synoptic climatology of the thermal low-pressure systems over south-western North America. *Int. J. Climatol.*, **12**, 529–545.

Schmidli, R. J., 1986: Climate of Phoenix, Arizona. NOAA Tech. Memo. NWS WR-177, 101–114.

Schmitz, J. T., and S. L. Mullen, 1996: Water vapor transport associated with the summertime North American monsoon as depicted by ECMWF analyses. *J. Climate*, **9**, 1621–1634.

Schaaf, C. B., J. Wurman, and R. M. Banta, 1988: Thunderstorm-producing terrain features. *Bull. Amer. Meteor. Soc.*, **69**, 272–277.

Shapiro, M.A.. 1981: Frontogenesis and Geostrophically Forced Secondary Circulations in the Vicinity of Jet Stream-Frontal Zone Systems. *J. Atmos. Sci.*, **38**, 954–973.

Sellers, W. D., and R. H. Hill, 1974: *Arizona Climate 1931–1972*. The University of Arizona Press, 616 pp.

Stensrud, D. J., 1993: Elevated residual layers and their influence on surface boundary-layer evolution. *J. Atmos. Sci.*, **50**, 2284–2293.

-----, R. L. Gall, S. L. Mullen, and K. W. Howard, 1995: Model climatology of the Mexican monsoon. *J. Climate*, **8**, 1775–1794.

-----, R. L. Gall, and M. K. Nordquist, 1997: Surges over the Gulf of California during the Mexican monsoon. *Mon. Wea. Rev.*, **125**, 417–437.

Smith, W. P., and R. L. Gall, 1989: Tropical squall lines of the Arizona monsoon. *Mon. Wea. Rev.*, **117**, 1553–1569.

Tang, M. and E. R. Reiter, 1984: Plateau monsoons of the Northern Hemisphere: A comparison between North America and Tibet. *Mon. Wea. Rev.*, **112**, 617–637.

Trapp, J. R. and C. E. Doswell, 2000: Radar data objective analysis. *J. Atmos. Oceanic Technol.*, **17**, 105–120.

Wallace, C. E., 1997: Convective storm environments in central Arizona during the summer monsoon. M.S. Thesis, School of Meteorology, University of Oklahoma, Norman, OK, 117 pp.

-----, R. A. Maddox, and K. W. Howard, 1999: Summertime convective storm environments in central Arizona: Local observations. *Wea. Forecasting*, **14**, 994–1006.

Watson, A. I., R. L. Holle, and R. E. Lopez, 1994a: Cloud-to-ground lightning and upper-air patterns during bursts and breaks in the southwest monsoon. *Mon. Wea. Rev.*, **122**, 1726–1739.

-----, R. E. Lopez, R. L. Holle, 1994b: Diurnal cloud-to-ground lightning patterns in Arizona during the southwest monsoon. *Mon. Wea. Rev.*, **122**, 1716–1725.

Weisman, M. L., and J. B. Klemp, 1986: Characteristics of isolated convective storms. *Mesoscale Meteorology and Forecasting*, P. S. Ray, Ed., Amer. Meteor. Soc., 331–358.

Wilks, D. S., 1995: *Statistical Methods in the Atmospheric Sciences.* Academic Press, Inc., San Diego, CA, 464 pp.

Zhang, J., 2000: Three-dimensional mosaic displays of data from multiple WSR-88D radars. Postprints, *Southwest Weather Symposium*, Tucson, AZ, 69–73.